

Seismic Applications of Interactive Computational Methods

By

Min Li

The Department of Geosciences
University of Sydney

A thesis submitted to The University of Sydney
for the degree of Master of Science
in Geophysics

July, 2000

ABSTRACT

Effective interactive computing methods are needed in a number of specific areas of geophysical interpretation, even though the basic algorithms have been established. One approach to raise the quality of interpretation is to promote better interaction between human and the computer. The thesis is concerned with improving this dialog in three areas: automatic event picking, data visualization and sparse data imaging.

Fully automatic seismic event picking methods work well in relatively good conditions. They collapse when the signal-to-noise ratio is low and the structure of the subsurface is complex. The interactive seismic event picking system described here blends the interpreter's guidance and judgment into the computer program, as it can bring the user into the loop to make subjective decisions when the picking problem is complicated. Several interactive approaches for 2-D event picking and 3-D horizon tracking have been developed. Envelope (or amplitude) threshold detection for first break picking is based on the assumption that the power of the signal is larger than that of the noise. Correlation and instantaneous phase pickers are designed for and better suited to picking other arrivals. The former is based on the cross-correlation function, and a model trace (or model traces) selected by the interpreter is needed. The instantaneous phase picker is designed to track spatial variations in the instantaneous phase of the analytic form of the arrival. The picking options implemented into the software package *SeisWin* were tested on real data drawn from many sources, such as full waveform sonic borehole logs, seismic reflection surveys and borehole radar profiles, as well as seven of the most recent 3-D seismic surveys conducted over Australian coal mines. The results show that the interactive picking system in *SeisWin* is efficient and tolerant. The 3-D horizon tracking method developed especially attracts industrial users.

The visualization of data is also a part of the study, as picking accuracy, and indeed the whole of seismic interpretation depends largely on the quality of the final display. The display is often the only window through which an interpreter can see the earth's substructures. Display is a non-linear operation. Adjustments made to meet display deficiencies such as automatic gain control (AGC) have an important and yet ill-

documented effect on the performance of pattern recognition operators, both human and computational. AGC is usually implemented in one dimension. Some of the tools in wide spread use for two dimensional image processing which are of great value in the local gain control of conventional seismic sections such as edge detectors, histogram equalisers, high-pass filters, shaded relief are discussed. Examples are presented to show the relative effectiveness of various display options.

Conventional migration requires dense arrays with uniform coverage and uniform illumination of targets. There are, however, many instances in which these ideals can not be approached. Event migration and common tangent plane stacking procedures were developed especially for sparse data sets as a part of the research effort underlying this thesis. Picked-event migration migrates the line between any two points on different traces on the time section to the base map. The interplay between the space and time domain gives the interpreter an immediate view of mapping. Tangent plane migration maps the reflector by accumulating the energy from any two possible reflecting points along the common tangent lines on the space plane. These methods have been applied to both seismic and borehole-radar data and satisfactory results have been achieved.

ACKNOWLEDGMENTS

I would like to thank my supervisor Prof. Iain Mason for his advice and guidance to my study. I also wish to thank him for spending his valuable time to read, correct and comment on my thesis.

I wish to thank Dr Peter Hatherly for showing me his early work on the first break detection, and for his advice on the problem solutions.

This study was supported by the ARCO British Geophysical Imaging Research Laboratory, Australian Research Council (ARC) and the Center of Mining Technology and Equipment (CMTE). I also would like to thank BHP Coal (Appin Colliery), Callide Coal Mines and Burton Coal Mine for allowing me to use their data.

I wish to thank my parents. They always encouraged me to pursue my career. I also thank my children, Jieyun and Edward, for being such good kids, so that I could concentrate on my study. My last thanks go to my husband, Binzhong Zhou, for his constant support and help, as well as clear guidance and objective criticism through my study, which has helped me reach the final line.

DECLARATION

I certify that this thesis does not incorporate without acknowledgement any material previously submitted for a degree or diploma in any university; and that to the best of my knowledge and belief it does not contain any material previously published or written by another person except where due reference is made in the text.

Min Li

TABLE OF CONTENTS

ABSTRACT	I
ACKNOWLEDGMENTS.....	III
DECLARATION	IV
TABLE OF CONTENTS	V
LIST OF FIGURES.....	VII
LIST OF TABLES.....	XIII
CHAPTER 1 INTRODUCTION.....	1
1.1 INTRODUCTION.....	1
1.2 SEISMIC DATA PROCESSING AND INTERPRETATION	1
1.3 OBJECTIVES AND THE LAYOUT OF THE THESIS.....	2
CHAPTER 2 2-D EVENT RECOGNITION & INTERACTIVE CORRECTION.....	4
2.1 INTRODUCTION.....	4
2.1.1 <i>Background</i>	4
2.1.2 <i>Signal Detection in Radar</i>	5
2.1.3 <i>Review of Earlier Works</i>	7
2.2 CONCEPTS OF SEISMIC EVENT PICKING.....	9
2.2.1 <i>Seismic Events</i>	9
2.2.2 <i>Picking Positions</i>	10
2.2.3 <i>Picking Logic -- Hand Picking</i>	13
2.3 AUTOMATIC FIRST BREAK DETECTION WITH INTERACTION	14
2.3.1 <i>Methods of First Break Picking</i>	15
2.3.2 <i>Interactive Picking Methods</i>	18
2.3.3 <i>Other Measurement Positions of the First Arrival</i>	23
2.3.4 <i>Discussion</i>	24
2.4 INTERACTIVE SEISMIC EVENT TRACKING.....	25
2.4.1 <i>The correlation method</i>	25
2.4.2 <i>The Instantaneous Phase Picker</i>	27
2.5 CONCLUSIONS	32
CHAPTER 3 3-D HORIZON TRACKING	34
3.1 INTRODUCTION.....	34
3.2 HORIZON TRACKING IN A 3-D DATA VOLUME	34
3.2.1 <i>3-D Horizon Model Construction and Auto-picking</i>	35
3.2.2 <i>3-D Horizon Tracking</i>	36
3.2.3 <i>First 3-D seismic survey in Appin area 4</i>	39
3.2.4 <i>Second 3-D seismic survey in Appin area 4</i>	41
3.2.5 <i>3-D seismic survey in Newlands</i>	44
3.2.6 <i>3-D seismic survey in Burton</i>	46
3.3 CONCLUSIONS	48
CHAPTER 4 SEISMIC DISPLAY AND INTERPRETATION.....	49
4.1 INTRODUCTION.....	49
4.2 BASICS OF SEISMIC DISPLAY	50
4.2.1 <i>Seismic Display</i>	50
4.2.2 <i>Instantaneous Seismic Attribute Display</i>	52
4.2.3 <i>Zoom Function in Seismic Display</i>	52
4.2.4 <i>Automatic Gain Control</i>	54

4.2.5 <i>Clipping & Comanding</i>	56
4.3 IMAGE ENHANCEMENT AND SEISMIC DISPLAY.....	57
4.3.1 <i>Using Filters</i>	57
4.3.2 <i>Edge Detection</i>	60
4.3.3 <i>Histogram Processing</i>	62
4.3.4 <i>Local Enhancement</i>	66
4.3.5 <i>Gray Scale and Color Display</i>	67
4.3.6 <i>Shaded Relief</i>	69
4.4 DISCUSSIONS AND CONCLUSIONS.....	72
CHAPTER 5 NON-UNIFORM SPARSE DATA AND IMAGING.....	74
5.1 INTRODUCTION.....	74
5.2 BASIC PATTERN OF REFLECTIONS.....	75
5.2.1 <i>Reflection Models</i>	75
5.2.2 <i>Diffraction Model</i>	77
5.2.3 <i>Hyperbolic Move-out</i>	78
5.3 TWO-DIMENSIONAL SEISMIC IMAGING.....	80
5.3.1 <i>Conventional Pre-Stack Migration</i>	81
5.3.2 <i>Diffraction Summation</i>	82
5.3.3 <i>Interactive migration on a personal computer</i>	85
5.4 IMAGING WITH SPARSE DATA.....	88
5.4.1 <i>Event Migration</i>	88
5.4.2 <i>Common tangent line stacking</i>	93
5.5 DISCUSSIONS AND CONCLUSIONS.....	98
CHAPTER 6 DISCUSSION AND CONCLUSION.....	100
BIBLIOGRAPHY.....	102

LIST OF FIGURES

Figure 2.1 A diagram of the first arrival and later arrival measure points. The solid curve is a trace while the dashed-curve is the corresponding envelope.	10
Figure 2.2 Hand picking result shown in two different resolutions. (a) The visual picked maximum position. (b) The enlarged (zoomed) section of (a).	12
Figure 2.3 Illustration of 3-point parabolic fitting for locating the true local peak. The three adjacent points used for curve fitting are marked in dots. The peak location on sample and the true peak location computed by the curve fitting interpolation are indicated by the left and right vertical lines, respectively.	12
Figure 2.4 A diagram of picking zero-crossing points. (a) If a signal has zero mean value, its zero-crossing points are easily detected; (b) seismic signals do not have zero mean, zero-crossing points need to be detected carefully.	13
Figure 2.5 A signal displayed in three different magnifications. Top picture is in normal display scale, the middle one has 20 times more magnifications than the normal display scale while the bottom one has 50 times magnifications than the top one. The apparent first break position (arrow position) in the normal scale display is obviously not accurate.	14
Figure 2.6 The diagram of calculating the ratio function. The energy ratio at point k is obtained from short-term-average W_2 to long-term-average W_1	16
Figure 2.7 The two-sided ratio function. (a) A synthetic signal followed by ratio functions corresponding to different window length ratios (i.e., " $w_2/w_1=30/50$ " means that the short-term window length is 30 samples and the long-term window length is 50 samples). The column (b) shows a real signal, which was extracted from a fault proximity survey in the North Sea. Crosses mark the possible threshold. The vertical line indicates the estimated first break position. Column (c) shows a real signal extracted from the data collected in the Appin area by BHP Coal. Because of the low SNR, the threshold detection is at a big risk of "false alarms".	17
Figure 2.8 The picked result (the white curve) by using the two-sided ratio function detection. Data courtesy of BHP Coal (Appin Colliery).	17
Figure 2.9 The picking procedure. The user picks the "Guide curve" before which no relevant energy could have arrived. After applying the envelope detector, the first pass picks are shown in (b). The model trace, shown in (a) with a vertical black line on the first break, is served as a reference for adjusting the first break picks on neighboring traces. The observer is free to pick as many model traces as the data quality might require, or as few as time constraints will allow. The final picks after the phase adjustment are shown in (c).	20
Figure 2.10 The first break picking result is shown on this common shot gather. The envelope threshold detection method was used. Sample pick traces and the model trace are shown below. The white lines mark the positions of the sample traces. The vertical line on these sample traces mark the final picking positions. The white dot on the section indicates the model trace position selected during picking. The data comes from BHP Tower Colliery.	21
Figure 2.11 The first break picking result (the black curve) is shown on the full waveform sonic log section. Sample pick traces and the model trace are shown	

below. The envelope threshold detection method was used. The white lines mark the positions of the sample traces. The vertical line on these sample traces mark the final picking positions. The white dot on the section indicates the model trace position selected during picking. Data courtesy of Callide coal mine.	22
Figure 2.12 The upper diagram illustrates the idea of user guidance using the data in Figure 2.8, while the lower diagram shows the re-picked result.	23
Figure 2.13 A diagram of the local maximum (/minimum). The search length determines the range the computer looks for the maximum value. Numbers 1-5 mark the peak and trough positions for two search lengths.	24
Figure 2.14 The picking procedure based on correlation.	26
Figure 2.15 S-wave arrival picking within the user-defined correlation range marked by black zigzag lines. The white spot indicates the position where the model arrival was taken. The picked S-wave is shown by the white curve. The model trace and three example traces are shown below the section. Data courtesy of BHP Appin Colliery.	27
Figure 2.16 The comparison between the image display and the instantaneous phase display. The arrows in (a) and (b) show three events in two different displays. (c) Portion of section (a) displayed in wiggles. (d) Portion of section (b) displayed in wiggles. The horizontal lines across the wiggle displays are used to mark the trough of each event in the real signals in (c) and the corresponding positions in the phase display (d).	29
Figure 2.17 The picking procedure based on the discontinuity of the instantaneous phase.	30
Figure 2.18 The result by using the instantaneous phase picker is shown in the image display and the instantaneous phase display.	30
Figure 2.19 The first arrival of the full waveform sonic log segment was picked (the dark gray curve) by the instantaneous picker. Data courtesy of Callide coal mine.	31
Figure 2.20 The interactive correction process. The black arrow on the image of (a) indicates a mispick occurred in the picking process. This mispicking position can be easily located as shown by (b) which indicates that the picked position had one cycle shift to the right. After moving the pick position manually one cycle to the left (c), the mispick is corrected (d).	32
Figure 3.1 A sketch of common bin gathers in 3-D surveys.	35
Figure 3.2 An illustration of a subsurface cut by in-lines and cross-lines. The in-lines and cross-lines construct a grid on the surface which covers the whole survey area.	36
Figure 3.3 The coarse grid forms a control grid used for automatic horizon tracking.	38
Figure 3.4 The automatically picked Bulli coal seam surface for the first 3D seismic survey at Appin Area 4 is displayed as a two-way reflection time contour.	40
Figure 3.5 Examples of picked results (in red) on four inline sections for the first 3D seismic survey at Appin Colliery Area 4. The red label at each top left-hand corner of the image represents the corresponding inline number.	40
Figure 3.6 The contour map of reflection times for the Bulli Seam for the second 3D seismic survey at Appin Colliery, generated by the correlation method.	42
Figure 3.7 Examples of picked results shown on inline sections for the second 3D seismic survey at Appin Colliery. The label at each top left-hand corner of the	

image represents the corresponding inline number. The mispicks are marked by black rectangular areas.	42
Figure 3.8 The contour map of reflection times for the Bulli Seam for the second 3D seismic survey at Appin Colliery. The reflection times were obtained from the instantaneous phase method.	43
Figure 3.9 The picked result from the instantaneous phase method on some sections. The red label at each top left-hand corner of the image represents the corresponding inline number.	43
Figure 3.10 Since the instantaneous phase is independent of the amplitude strength, a horizon that appears with good signal-to-noise ratio looks clear and easy to follow, while the reflection strength on the same event is different from trace to trace. White rectangles are used to show the areas where most variation occurred between picking methods. The instantaneous phase picker will have less mis-picks due to its increased S/N ratio. Black arrows mark the same event on the two display styles. .	44
Figure 3.11 3D picking result for the Newlands 3D seismic survey. The two-way reflection time contours (left) of the Upper Newlands coal seam and the shaded relief presentation (right) of the reflections with the light source at 50 degrees east of south and 45 degrees above the horizon.	45
Figure 3.12 Sample sections show the picks (in red) by the instantaneous phase method for the Newlands 3D seismic survey. The label at each top left-hand corner of the image represents the corresponding inline number.	46
Figure 3.13 The two-way reflection time contours (left) of the Burton coal seam from a portion of 3D seismic survey at Burton Coal Mine.	47
Figure 3.14 Four examples of picked sections (in red) from the 3D seismic survey at Burton Coal Mine.	47
Figure 4.1 A few common used seismic display methods. (a) The image display; (b) The wiggle display; (c) The variable area display; (d) The superposition of the variable area and the wiggle trace.	50
Figure 4.2 Three instantaneous attribute displays. Data courtesy of Burton Coal mine. (a) Real seismic section; (b) Instantaneous phase display of (a); (c) Instantaneous amplitude display of (a).	52
Figure 4.3 Zooming on a single seismogram.	53
Figure 4.4 The zoom or re-scale is an important tool in seismic interpretation. By using different vertical and horizontal scale, some important feature may be revealed. (a) A vertical section from the Bulli seam; (b) The vertically enlarged version of the original image reveals a possible fault; (c) The horizontally enlarged version may conceal the possible fault.	53
Figure 4.5 The gain function is calculated for each time gate.	55
Figure 4.6 The results of automatic gain control. T (=20 ms) is the dominant period.	55
Figure 4.7 The signal shape after applying AGC. The window length is denoted by "wlen". T is the dominant period.	56
Figure 4.8 Value clipping. Dynamic range can be decreased by clipping some percentile of elements (shaded area) from two ends of the sorted array.	57
Figure 4.9 Different Clipping factors applied to an image.	57
Figure 4.10 Median filters with different shapes.	58

Figure 4.11 (a) The first breaks picked (the red curve) by amplitude threshold detection; (b) The first breaks are picked again after applying the median filter to the raw data.	59
Figure 4.12 (a) Original image from part of full waveform sonic collected from Callide coal mine; (b) The result of high pass-filtering using M3 (displayed in the negative form of the actual image).....	59
Figure 4.13 Using sharpening filter M1 to highlight details.	60
Figure 4.14 Edge detection. This portion of image is an inline section (#41) of the 3D data from BHP Appin Colliery. (a) The original image with 3% clipping; (b) The result yielded by the Sobel edge detection – vertical operator with high boost filtering. The white arrows mark possible geological discontinuities which can not be seen in the original image.	61
Figure 4.15(a) The original image; (b) After applying a Laplacian operator on (a); (c) after applying a Sobel operator on (a).	61
Figure 4.16 Clipping guided by the histogram. (a) The original image and its histogram (right side of (a)); (b) The clipped image guided by the original histogram and the new histogram.....	63
Figure 4.17 A gray-level transformation function. The horizontal axis presents the gray levels of the source image, the vertical axis presents the gray levels of the destination image. The transformation procedure can be considered as a mapping procedure as the arrows indicate.	64
Figure 4.18 Histogram equalization processing. (a) The corresponding improvement to the original image which was shown in Figure 4.16(a). (b) The histogram corresponding to (a).....	65
Figure 4.19 Histogram specification method. The transformation function for each image is placed right beneath it. (a) The transformation is a linear function and the original image is unchanged; (b), (c) The new images produced by the transformation function. The pictures were produced by using CoreIDRAW7.....	66
Figure 4.20 The local enhancement operation has made the original image more informative. Two different mask sizes are used for illustration. The histogram of each image was placed right underneath its image.....	67
Figure 4.21 (a) is an original image. (b), (c) and (d) are the original image displayed with different entries of gray scale. The image contrast can be improve by choosing appropriate palette entry.	68
Figure 4.22 Tricolor and grayscale displays.....	68
Figure 4.23 Colormap display.	69
Figure 4.24 Shaded relief display. (a) The original image; (b) The light was from the north and the height of light was 45 degrees from the horizon; (c) The light was from the east and the height of the light was 45 degrees from the horizon; (d) The light was from the exact top of the image.	70
Figure 4.25 Shaded relief display of the Upper Newlands seam. (a) The light source is at 320 degrees from the east and 30 degrees from the horizon; (b) The light source is at 55 degrees from the east and 60 degrees from the horizon; (c) The light source is at 60 degrees from the west, 40 degrees from the horizon. Images are presented using Surfer. The black arrow in (a) indicates a trend extended toward top-right corner, while (c) reveals that this trend is also connected with another trend marked	

by the black arrow. The trend indicated by the black arrow in (b) can not be seen on the other two images.....	71
Figure 5.1 Diagram illustrating the reflection raypath and its traveltime curve for a horizontal reflector– a hyperbola of time-distance relationship.....	75
Figure 5.2 A traveltime curve for a dipping reflector– an asymmetric hyperbola.....	77
Figure 5.3 Diagram illustrating diffraction raypaths and corresponding traveltime curves.....	78
Figure 5.4 Illustration of pre-stack migration for sub-surface reconstruction.....	81
Figure 5.5 Illustration of the computation procedure of diffraction summation.....	83
Figure 5.6 (a) The synthetic diffraction hyperbola for a borehole radar survey. (b) The migrated sections shows two mirror images.....	84
Figure 5.7 The migration results of a synthetic hyperbola with different migration apertures. Large apertures compact the diffraction image.....	84
Figure 5.8 Velocity governs the shape of diffraction hyperbolae.....	85
Figure 5.9 The relationship of migration & velocity. The dot indicates the expected point.....	85
Figure 5.10 A borehole radar survey in South Africa was simulated by reflection modeling. (a)The time section of the profile line shown on the base map; (b) The migrated section; (c), (d) Reflection simulation (green lines) and corresponding reflectors drawn by the computer simultaneously on both maps.....	86
Figure 5.11 A migrated reflector (marked by the magenta dots on (b)) is tangent to the diffraction curves (the red curves on (a))......	87
Figure 5.12 The hyperbolic diffraction patterns (red curves) on (b) match those scattering locations (yellow dots) on migrated image (c)......	88
Figure 5.13 Diffraction summation for dense sampled data (on the top row); (b) Diffraction summation for a very sparse data set (on the bottom row).....	89
Figure 5.14 Event migration seeks common tangents of two elliptical reflectors. There are three possible relationships of the two ellipses as shown here. This can give upto 4 possible solutions/tangent lines.....	89
Figure 5.15 The geometrical relationship between CMP and the true reflection point for a dipping reflector.....	90
Figure 5.16 (a) Radar data mapping of events A, B & C with event migration; (b) Mapped events on the basemap with their mirror images; (c) Mirror images in (b) eliminated according to prior geological knowledge. The background image in (b) & (c) is the Kirchhoff migration result of (a)......	93
Figure 5.17 Each pair of circles has at least two common tangent lines. After all possible combination of two circles common tangent lines are mapped, the hypothetical reflector should accommodate the most repeated common tangent lines from mapping.....	94
Figure 5.18 Inverse mapping. (a) A synthetic two trace data set and its base map. The green line indicates the reflection plane and two red dots show the receiver positions; (b) Diffraction summation results in two semicircles on the base map. (c) Common tangent line stacking provides the correct reflector image.....	95
Figure 5.19 Inverse mapping. (a) A base map model shows 7 receivers (marked by red dots) and two reflection planes (green lines) corresponding to the synthetic sparse data in (b); (c) Diffraction summation migrates the data into circles; (d) The result	

from common tangent line stacking; (e) The image from (d) with different gray levels.....	96
Figure 5.20 Forward mapping procedure. For any given reflector, we can trace the corresponding travel time to the time section. The average energy of the product of travel time t_1 and t_2 is assigned to line p_1p_2 on the migrated section. An accumulation of energy should reveal the real reflector in theory.	97
Figure 5.21 Forward mapping. The green line indicates the reflection plane and the two red dots show the receiver positions.....	97
Figure 5.22 Forward mapping. (a) A base map model shows 7 receivers (marked by red dots) two reflection planes (green lines) corresponding to the synthetic sparse data in (b); (c) Diffraction summation migrates the data into circles; (d) The result from common tangent line stacking; (e) The image from (d) with different gray levels..	98
Figure 5.23 The event migration algorithm developed in this chapter is not applicable to the general case where the major axes of any two ellipses are not necessarily in a line. (b) The event migration can be approximated by converting the non-zero offset data into zero offset.	99

LIST OF TABLES

Table 4-1 Instantaneous attributes	52
--	----

CHAPTER 1 INTRODUCTION

1.1 INTRODUCTION

The mining industry is currently facing a crisis of confidence in establishing geological conditions ahead of mining. Significant investments are on hold until geological certainty can be established. Seismic reflection surveying is one method of securing geological information (Zhou and Hatherly, 1999). However, interpretation of the geophysical results requires software tools tailored specifically towards the mining industry. A PC Windows based computer program *SeisWin*¹ was originally designed in Oxford. The purpose was to reduce mine development risk by allowing the validity of geologists' forecasts to be tested by the geologists and geophysicists against the concrete evidence offered by running radar and/or seismic profiles down boreholes. It was expanded into a powerful general-purpose geophysical imaging and analysis software package. *SeisWin* has found widespread interest from many companies and researchers, and been continuously developed to provide better tools for geological interpretations and visualization for mine sites. This thesis developed alongside and as a part of the development of the current version of *SeisWin*².

1.2 SEISMIC DATA PROCESSING AND INTERPRETATION

Seismic exploration can be divided into three main stages: data acquisition, processing and interpretation (Yilmaz, 1987). This study is concerned with the last two stages. Geophysicists interpret seismic or ground radar arrival patterns (events) in order to map underground geological structures and stratigraphic features. Timing the arrivals of those seismic waves (seismic events) is very important. Travel-time tomography, static correction computation, reflection radar and seismology benefit from the accurate picking of event times. Two basic picking methods are widely used: manual picking and automatic computer picking. The former can be more reliable if the display is flexible

¹ The software package inherited from researches of over 25 years by researchers within Professor Iain Mason's group.

² A 2000 ACARP project.

and the interpreter is competent, but the procedure can not cope with the increasingly large data volumes that are routinely acquired nowadays. Fully automatic methods, however, are easily misled by attenuation, sensor coupling variations, random scattering in the overburden and the competition of multiple arrivals for a given time slot. The task of designing a robust "hands-off" picking system for 3-D data is difficult.

One of the important steps in geophysical prospecting is to identify/verify and map geological features or patterns underground. A uniformly dense coverage in data acquisition is ideal for interpretation, but it is not always achieved. Non-uniform and very sparse arrays may be the only available layouts, especially in mining and environmental geophysics. There are various ways to map geophysical data into meaningful images, but most are suitable for spatially well-sampled data arrays. The challenge in mining geophysics is often to map effectively with non-uniform shooting geometries and irregular, sparsely sampled gathers of traces

1.3 OBJECTIVES AND THE LAYOUT OF THE THESIS

There are three main parts to this thesis: automatic seismic event picking in both 2D and 3D, seismic image display and sparse data mapping. Aside from the introduction chapter, the thesis is laid out as follows:

Seismic event detection is an old problem, but it needs to be reworked as computers improve. In chapter 2, the theory of radar signal detection and previous work on the automatic event picking of seismic events are reviewed. A new semi-automatic event recognition system is introduced. This system can be driven as close to the ideal of "hands-off" automatic picking if the interpretation is warranted by data quality. The interactive method developed as a part of this study and encoded in *SeisWin* is tested on a number of field time sections.

Chapter 3 deals with the extension of the two-dimensional event recognition system to three-dimensions, in order to track horizons interactively through 3D data sets. The 3D

picking method, developed for *SeisWin*, has been used to trace horizons through seven 3D seismic surveys conducted in Australian coal fields over the past two years.

Various seismic display methods are set out in chapter 4, where we comment on and demonstrate some of the potential applications of image enhancement techniques to interpretation operations.

Chapter 5 is a contribution to a particular form of migration, in which non-uniform illumination of the target field is a problem. I show that the normal "exploding point target" approach to the design of migration operators falls over if the imaging array is sparse and the target is not a point. Two effective methods designed for imaging with sparse data are described.

Conclusions and discussions are made in the final Chapter.

CHAPTER 2 2-D EVENT RECOGNITION & INTERACTIVE CORRECTION

2.1 INTRODUCTION

2.1.1 Background

One of the primary tasks in exploration seismology is to interpret seismic arrival patterns propagated from the source to receiver through the earth, to map subsurface geological structure and stratigraphic features. The recorded seismic waves consist of a series of seismic events. The seismic event may be a reflection, refraction, surface wave, random signal etc, which carries information about the earth's subsurface. Timing the arrivals of those seismic waves (seismic events) is usually the first step in reducing field data in order to relate seismic observations to geologically plausible structural models. However, seismic event detection is a difficult process, as the arrival pattern can be complicated even with a simple earth model due to a combination of factors, such as the variety of seismic wave types, the nature of subsurface structures, the signal capturing ability of recording instruments and noise interference. Correct recognition of seismic events and precise measurement of their arrival times are an essential step in both earthquake seismology and seismic exploration studies.

Seismic tomography plays an important role in seismic data interpretation. Travel-time tomography breaks into two classes: active and passive. In passive tomography such as in macro earthquake location and micro-seismic detection in mines, we have to measure the time of the initiation of the seismic wavefield so that we can determine where the source of seismic energy occurred and when it starts. We can also recover a three-dimensional model by measuring the travel-time residuals for body waves or modified dispersion characteristics for surface waves. In active tomography, because the source excitation time is known, the times of first arrivals can be measured with high accuracy. More attention may be paid to measuring later arrivals in order to resolve the complex structure of the subsurface. Travel-time tomography is improved by precise measurement of arrival times.

Static errors arise in active seismology if the shot and record is not well synchronized. They also appear if the sensors are poorly coupled to the continuum by, for example, patch of low velocity, as if they are deployed in hilly country. Static correction computation is used to correct reflection times that are affected by irregularities of the near-surface. The procedure requires reliable picking times of the direct and the refracted first arrivals.

Event picking is important in reflection radar and seismology, especially when structures in subsurface are non-uniformly illuminated. Faint reflections that look insignificant may carry important geological information about subsurface structures. When conventional migration is performed on such data, the information may be submerged beneath strong arrivals. To increase the energy contribution for faint reflections, faint events can be picked and converted to a spike-a-gram that can be substituted for this recorded time section in order to image the source of faint events.

2.1.2 Signal Detection in Radar

A radar radiates an electromagnetic pulse, detects the echo returned from reflecting objects and displays the result usually on a plan position indicator. The desired signal in the echo is corrupted with unwanted noise, which may be cluttering noise, system noise (such as thermal noise and noise-generating process) and other interference (i.e., jamming). The echo then is passed to a detector where a decision is made as to whether or not a particular type of signal is present in the total measured voltage in an interval of time. Many detection theories and sophisticated techniques have been developed in radar observation. The problem of the detection of a signal in noise falls under the category of the testing of hypotheses (Robinson, 1967), because a radar signal is the random fluctuation in the additive noise that corrupts the received signal. The two statements of hypothesis testing commonly used in statistical signal detection are: H_0 means that only the noise is present; H_1 means that the signal exists (as well as the noise). Because the noise is unpredictable, the decision remains uncertain. However, a statistical description of the noise can be considered as a stochastic process³. For such a designated decision

³ also called random process. A stochastic process is a function of time, defined on some observation interval and used to describe the time evolution of a statistical phenomenon according to probabilistic laws. The statistical nature of the phenomenon means that it is impossible to define exactly the way the function evolves with time before hand (Haykin, 1991).

(as threshold detections), the signal is detected when the signal amplitude $r > r_0$. The probability of the error Q_0 is given by

$$Q_0 = \int_{r_0}^{\infty} P(r | H_0) dr, \quad (2.1)$$

where $P(r|H_0)$ is the probability density of r given that H_0 is true. Q_0 is also known as "false alarm". In contrast to Q_0 , the probability density of r given that H_1 is true Q_m (i.e., noise is accepted as signal) is defined as

$$Q_m = \int_{-\infty}^{r_0} P(r | H_1) dr. \quad (2.2)$$

Therefore, the probability of a correct decision is:

$$Q_d = 1 - Q_m. \quad (2.3)$$

Ideally, a desired r_0 should set the false alarm Q_m to zero and the right decision Q_d to 1. However, it is practically impossible to do because of unpredictable noise. The right detection level depends on decision criteria. Setting r_0 low lifts the certainty of signal detection and the probability of false alarm. Setting r_0 high drops the false alarm rate, but also drops the probability of detection. The Neyman-Pearson and the Bayes criterion are two well-known criteria used for setting the threshold of the signal for signal detection (details can be found in Helstrom, 1960). The choice of which decision criterion to use depends on available priori information, such as the statistical properties of the noise and signal. Various decision criteria enable us to solve the detection problem at hand with maximum efficiency. Optimum detectors can be designed using the general framework of statistical decision theory.

A matched filter is designed for signal detection according to the criterion of maximum signal-to-noise output at a given instant. The matched filter is matched in the sense that its impulse response is the time reverse of a known signal. When the output of a signal from such a filter is compared with a fixed statistical level r_0 , and if $r > r_0$, the signal is declared as present.

In geophysics a matched filter is optimized for signal detection. If a known signal is white Gaussian noise, it is not optimized for tracking the times of signal arrivals (For tracking, noise permitting, one uses an inverse filter as a noise adaptive Wiener filter).

2.1.3 Review of Earlier Works

Various approaches have been developed for automatic seismic event tracking. Many of them are based on the fact that there should be clear gradient changes when signals arrive. Paulson and Merdler (1968) used a number of grading criteria based on the mean amplitude across a segment to detect desired signal arrivals. Hatherly (1982) combined a method based on abrupt deviations of a signal and the linear least square prediction technique to detect the time of first arrival. Gelchinsky and Shtivelman (1983), and Ervin et al. (1983) used correlation properties of a signal to estimate first arrival times. McEvelly and Majer (1982), Baer and Kradolfer (1987), Gu, Zhou and Zhang (1992), and Earle and Shearer (1994) used the ratio of long-term energy to short-term energy to declare the first arrival. This is a popular method especially in microseismic and teleseismic studies. All of above methods are good, but they are not necessarily optimal and they all break down under some circumstances.

Coherence measure is another design philosophy behind some forms of automatic picking. Paraldi and Clement (1972) used the cross-correlation method to pick the seismic events. Yung and Ikelle (1997) proposed a seismic time picking method based on the third-order bispectrum estimation rather than the conventional cross-correlation. The cross-bispectrum is defined as $B_{x,y,z}(\omega_1, \omega_2) = E[Y(\omega_1)Z(\omega_2)\bar{X}(\omega_1, \omega_2)]$ where $E[.]$ is the expectation operator and \bar{X} is the complex conjugate of X . One major advantage of using higher order spectra in signal processing is that for Gaussian processes only polyspectra for order greater than two are identically zero (Nikias, Mysore and Raghuvver, 1987). For the fact that most seismic source wavelets are non-Gaussian and noises are considered Gaussian, then Gaussian noise does not distort the correlation peaks in the third-order domain. Under some circumstances the method combining with implicit spectral prewhitening produces high correlation peaks that track the first arrival time.

By using statistic theory, Cochran (1973) proposed a method based on sign-bit semblance (hypothesis testing). Hansen, Roy-Chowdhury and Phinney (1988) developed a sign filter for seismic event detection also based on hypothesis testing. The sign filter is applied along various slowness-intercept lines on the stacked section, then the value of each windowed segment is calculated under hypothesis H_0 . Finally, a reflector is expected to appear on the stacked section as a burst of energy coherence that is sustained over a number of traces.

Pattern recognition methods used in image processing offer other opportunities. Neural networks were used in automatic picking of the first arrival by Murat and Rudman (1992), Kusuma and Fish (1993) and McCormack, Zaucha and Dushek (1993). A neural network, ideally, can learn from different given examples (models) by training gradually to create the correct and general solution for a particular class of problems. There are numerous neural network architectures. Each has its own learning capabilities and designs for different pattern recognition problems. The fundamental idea is to take several segments of traces containing arrivals. The neural network iteratively adjusts a set of internal weights of a recursion formula (a cost function) until the arrivals are successfully predicted. The final step is to save the weights and pick the remaining traces.

String matching is another approach that has been used to extract seismic events (Bois, 1980; Liu and Fu, 1982; Wu and Nyland, 1987; Le and Nyland, 1990). The basic idea behind string matching is to choose pattern primitives, or simple sub-patterns such as a certain peak location, the peak width and height of a segment of a signal. Those pattern primitives must agree on heuristic rules (a cost function) for similarity. The cost function is not unique. The determination of the weights of the function is based on a prior knowledge and the judgement of an interpreter. After matching pairs are chosen, "parallel analysis" is introduced to enforce lateral coherence because mismatches are inevitable. The method is similar in application to neural networks. But, it much depends on the judgement of an interpreter and the choice of the cost function. Unlike a neural network, the weight settings are fixed. This makes the method less robust in the face of change.

A fractal-based algorithm for detecting first arrivals on seismic traces was reported by Boschetti et al. (1996). The picking method measures the change of fractal dimension within a window, it then detects the difference in fractal dimension before and after the first arrival. It actually picks the first peak / trough after the first arrival rather than the first kick. It is claimed to cope with low SNR traces well but the cost of computation is high.

Tu (1995) proposed a multiplicative operator system to track seismic events automatically. The raw seismic data are reduced into a set of salient features (tokens) by local 2-D spectral analysis. The Multiple Hypothesis Tracking (MHT) tracker tree is used to prune vigorous crossing events when pixels near the intersection of multiple events have spatially changing orientations. The criteria for pruning are set based on such ideas that seismic events should be paraxially hyperbolic (assuming reflection and diffraction) and local measures for tracking tangled events. The details of the method can be found in Tu (1995).

All the approaches discussed above widened knowledge of the event-tracking problem. In general, fully automatic event picking methods are effective if data quality is high, but it is difficult for an unsupervised machine to cope with the full complexities of nature. Critical human observers must be brought interactively into the loop if the picking problem is at all complicated.

2.2 CONCEPTS OF SEISMIC EVENT PICKING

2.2.1 Seismic Events

A lineup on a number of traces, which indicate the arrival of new seismic energy, is called an event. An arrival is characterized by its phase or amplitude change on a seismic record (Sheriff, 1991). In the early of the 20th century, information used in seismic interpretation were almost always first arrivals since it was very difficult to identify any later arrivals in their coda (Dobrin and Savit, 1988). With modern instruments and high technology, later arrivals can be read and are used frequently nowadays. However, first arrivals still play an important role in seismology. In this chapter, we will concentrate on

studying two aspects of seismic event picking/detection: the first arrivals and the later arrivals. Figure 2.1 depicts the two types of arrivals. There are a few measurement points indicating the arrival of these events, such as the first break, the peak/trough or zero-crossing positions. Picking these positions seems easy at first glance. But it is not trivial in practice especially if one wants to automate the picking process on a computer. Before discussing more detailed picking strategies, it is necessary to take a close look at known problems of event picking.

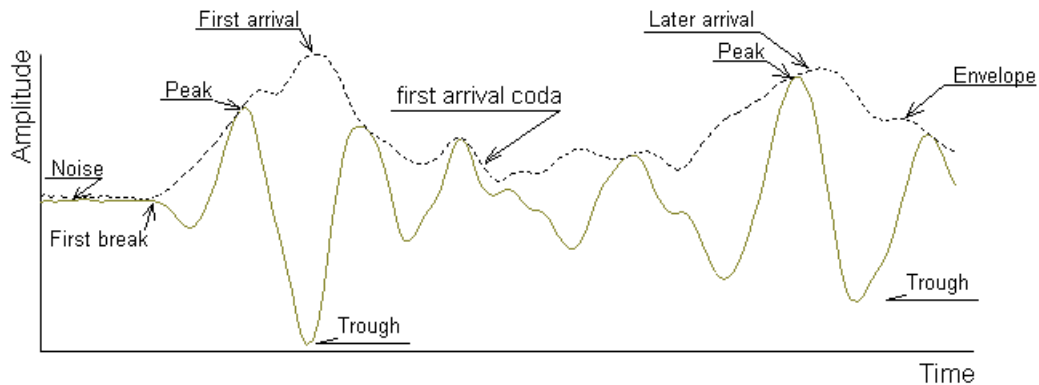


Figure 2.1 A diagram of the first arrival and later arrival measure points. The solid curve is a trace while the dashed-curve is the corresponding envelope.

2.2.2 Picking Positions

2.2.2.1 *The first break*

The onset of the first arrival (also termed by seismologists interchangeably as the onset, the first break, the first departure, the first kick), ideally, is defined as the first event marked by a clear change in gradient on a seismogram (Douglas, Bowers and Young, 1997). In fact, there is no sudden take off of the trace when disturbance arrives (Hatherly, 1982). In order to develop an automatic algorithm for picking first arrivals, we have to accept that:

- 1) There is normally very little energy at the first break point. To understand this, consider an impulse. When the impulse passes through the complex earth materials, energy is absorbed, partitioned, and it travels at different speeds through various mediums in various modes. As a result, the impulse becomes a wavetrain. The leading edge of the first arrival usually has very little energy. When the signal-to-noise ratio (SNR) is low, the first break motion may easily be buried in background noise.

- 2) Inhomogeneities, energy partitioning between modes, dispersion and attenuation all conspire to break the lock between the frequencies that form the first break.
- 3) Jamming can interfere with the first arrival. Micro-seismic noise may be spatially correlated as it sweeps across an array.
- 4) Every recording system response is different. Local patches of poor ground change the responses of seismometers, and shots.
- 5) Pre-filters distort signals (Douglas et al., 1997). Non-causal filters feed false precursors from strong early arrivals forward to compete with first breaks.
- 6) Cross-feed⁴ and shingling⁵ cause cycle-skipping, and make it hard to time a band limited first kick precisely (Hatherly, 1982).

The leading edge of the first arrival, in summary, is usually weak, spatially variant across an array, and hard to detect.

2.2.2.2 The peak/trough

Picking the maximum or minimum value by hand seems an easy task. On the computer screen, we only need to move the mouse and click the peak or trough position. However, when we zoom (i.e., increase the resolution) a peak, one finds that the peak flattens. Figure 2.2 shows a picked peak position in two different resolutions. In the zoomed picture (the right one), the peak position marked by the vertical line is no longer in the visual maximum position. Further more, even if we use the zoomed figure to pick the peak, the picking precision is limited by the sampling rate. This is illustrated by Figure 2.3. Therefore, if the true maximum position is determined by interpolating a local region in order to raise the sample rate, it gives a more accurate result than eyeball picking. This enables us to pick events accurate to sub-samples. The same concept can be used for finding true trough location to increase the picking accuracy.

⁴ or crosstalk, interference resulting from the unintentional pickup of one channel of information or noise on another channel (Sheriff, 1991).

⁵ Shingling is a loss of visibility of early cycles with increase in range (Sheriff, 1991).

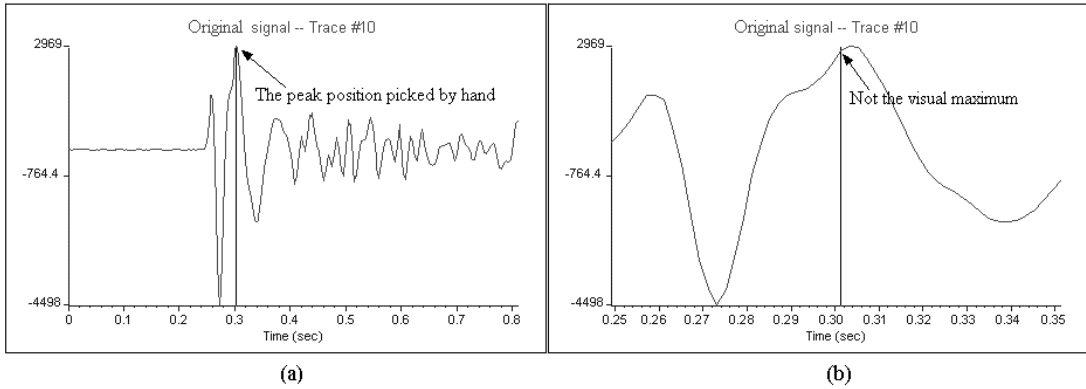


Figure 2.2 Hand picking result shown in two different resolutions. (a) The visual picked maximum position. (b) The enlarged (zoomed) section of (a).

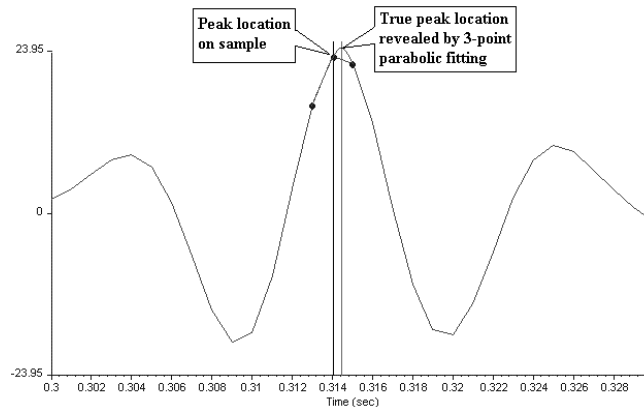


Figure 2.3 Illustration of 3-point parabolic fitting for locating the true local peak. The three adjacent points used for curve fitting are marked in dots. The peak location on sample and the true peak location computed by the curve fitting interpolation are indicated by the left and right vertical lines, respectively.

2.2.2.3 Zero-crossing

The zero-crossing is defined as the point where a seismic trace crosses the zero-deflection axis, the phase of a semi-periodic signal is zero or π (Sheriff, 1991). In practice, we use the mean value of a signal as its "zero-crossing" point as the field recording might contain a certain level of DC shift. Picking the zero-crossing position by hand is not as easy as finding a peak. Our eyes cannot identify the picking of an exact zero-crossing point, because zero-crossing points are determined by the average, which is not always at the zero value position. Figure 2.4 shows two common cases: one does not have a DC shift (Figure 2.4a), another one does (Figure 2.4b). Semi-automatic detection of a zero-crossing point is easier. For the latter case, we can find the zero-

crossing position which has the shortest distance to the mean value line in a user-defined length.

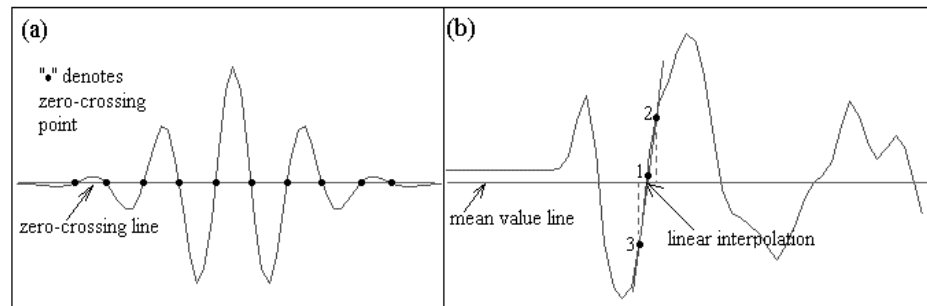


Figure 2.4 A diagram of picking zero-crossing points. (a) If a signal has zero mean value, its zero-crossing points are easily detected; (b) seismic signals do not have zero mean, zero-crossing points need to be detected carefully.

2.2.3 Picking Logic -- Hand Picking

Human eyes not only recognize patterns, but also can adaptively filter noise to extract necessary information. When an experienced interpreter does manual picking, he or she makes a decision based on the facts of the magnitude of the seismic wave, the shape of the phase and the coherent relationships between neighboring traces. When the noise is so predominant that even an experienced interpreter finds it hard to pick, the coherency of an event from adjacent traces may help. Hand picking by an experienced interpreter is considered reliable, but it is time consuming, tiring and it introduces an operator-specific bias. The picking precision will depend on the data's signal-to-noise ratio, the analyst's experience and understanding of the propagation process, prior knowledge of the problems at hand, the perception of human eyes, the sampling rate, the magnification and time scale of the display and the quality of the image's display.

Magnification is a non-negligible factor that affects the reading accuracy especially for the first break picking (Douglas et al., 1997). Figure 2.5 gives an example of a signal displayed with different magnifications. It is obvious that the first break reading (the top curve) will be later than the actual first arrival time when normal magnification is used for the display. Due to the presence of noise it is also very hard to decide by eye where is the exact first break point from the two magnified displays. The method of data display affects the precision of hand picking.

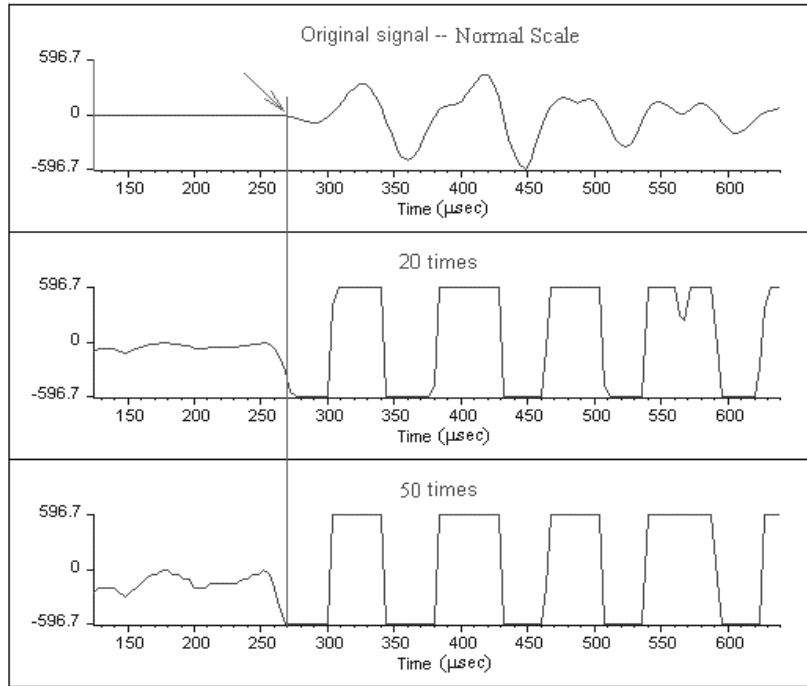


Figure 2.5 A signal displayed in three different magnifications. Top picture is in normal display scale, the middle one has 20 times more magnifications than the normal display scale while the bottom one has 50 times magnifications than the top one. The apparent first break position (arrow position) in the normal scale display is obviously not accurate.

Automatic picking is often designed to mimic human picking logic. Automatic picking is highly desired if data quantities are large. Numerous automatic time-picking methods have specifically been developed and designed for this purpose. The machine does not make subjective decisions, it depends completely on criteria set by humans. It can be made more tolerant of display magnification, but tolerance often comes at the price of robustness.

2.3 AUTOMATIC FIRST BREAK DETECTION WITH INTERACTION

Except for microseismics and false precursors produced by poor digital filters, first arrivals are the first recorded seismic arrivals after the source is excited, and first breaks lie at their leading edges. Because of wave dispersion, attenuation and equipment bandwidth limitations, the first arrival usually appears as a wavetrain instead of an impulse. Gain control, pre-filtering process and time sampling rate can all shift the apparent first arrival time.

2.3.1 Methods of First Break Picking

There are a number of published papers on automatic first break picking, such as Hatherly, 1982; McEvelly and Majer, 1982; Gelchinsky and Shtivelman, 1983; Ervin et al., 1983; Coppens, 1985; Baer and Kradolfer, 1987; Gu, Zhou and Zhang, 1992; Spagnolini, 1991; and McCormack, Earle and Shearer, 1994. The method based on the abrupt power change caused by a signal is the simplest. It is intuitively easy to explain and easy to implement. The most popular method uses the moving-window ratio function to detect the onset of the first arrival, especially in global seismic studies.

2.3.1.1 Ratio function method in the first break detection

A good example of the ratio function for detecting the first break was reported by Earle and Shearer (1994). The ratio function is obtained from the average envelope functions of two-moving windows. The envelope function $e(t)$ (or instantaneous amplitude) of a signal $x(t)$ is defined as (Yilmaz, 1987)

$$e(t) = \sqrt{x(t)^2 + y(t)^2}, \quad (2.4)$$

where $y(t)$ is the quadrature⁶ signal obtained from the Hilbert transform of a real signal $x(t)$. The ratio function is defined as

$$F(k\Delta) = STA/LTA, \quad (2.5)$$

where k is k th sample number, Δ is sampling interval; the short-term average STA of the envelope function is expressed as,

$$STA = \sum_{j=k}^{k+W_2} e_j / W_2, \quad (2.6)$$

and the long-term average LTA of the envelope function is,

$$LTA = \sum_{j=k-W_1}^k e_j / W_1, \quad (2.7)$$

where e_j is the j th envelope value along the trace; W_1 and W_2 are the window lengths in number of samples as illustrated in Figure 2.6. Function (2.5) is also called short-term-average to long-term-average ratio (STA/LTA) function (Earle and Shearer, 1994). The

⁶ The quadrature is a 90-degree phase-shift version of the recorded signal.

basic idea of this method is that the *STA* is considered to be sensitive to rapid increasing in the amplitude of a time series, while the *LTA* is an indication of the local background envelope amplitude. Therefore, the ratio in (2.5) is considered as a measure of local signal-to-noise (Earle and Shearer, 1994). When the ratio value exceeds a threshold, the first break is declared.

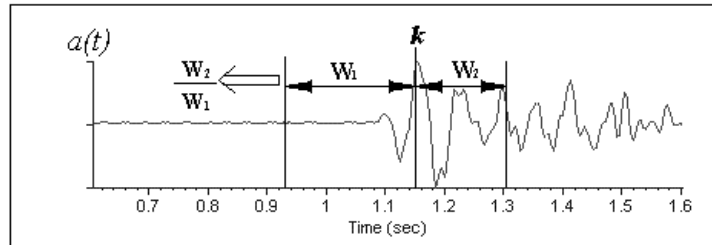


Figure 2.6 The diagram of calculating the ratio function. The energy ratio at point k is obtained from short-term-average W_2 to long-term-average W_1 .

Figure 2.7 is an example of the ratio function defined by Equation (2.5). Three different signals are used for testing. The first one in column (a) is a synthetic seismogram. The traces in columns (b) and (c) are real data. Different window length ratios are used to compute the ratio function in Equation (2.5). When the noise is not severe, the ratio functions give peak values near after the first break position with different window length ratios, as shown in column (a) and (b). The threshold can be generally decided by setting a percentage factor to the maximum ratio value (i.e., the peak value). For example, if the threshold is set to 100 (%), the threshold is actually the peak position of the ratio function. This causes the estimated pick to be later than the real onset. If a percentage factor is applied, the detected position can be moved backward from the peak position. When the SNR is very low, the peak position may no longer indicate the onset and there are risks of "false" picks (see the column(c)). Later verification is required.

Figure 2.8 shows the picking result by using the two-sided ratio function method. The data were collected by BHP coal in the Appin area. The threshold here was set as a product of 0.7 and the maximum value of the ratio function. This automatic method is generally good but it blows up when the SNR is low.

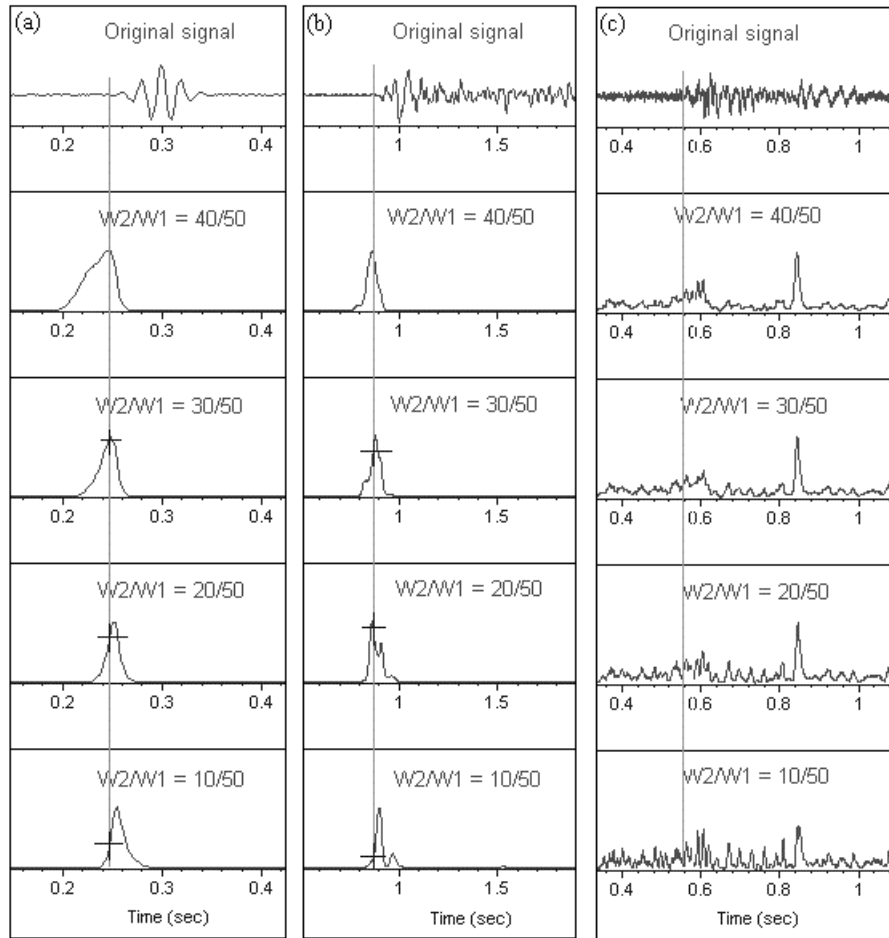


Figure 2.7 The two-sided ratio function. (a) A synthetic signal followed by ratio functions corresponding to different window length ratios (i.e., " $w_2/w_1=30/50$ " means that the short-term window length is 30 samples and the long-term window length is 50 samples). The column (b) shows a real signal, which was extracted from a fault proximity survey in the North Sea. Crosses mark the possible threshold. The vertical line indicates the estimated first break position. Column (c) shows a real signal extracted from the data collected in the Appin area by BHP Coal. Because of the low SNR, the threshold detection is at a big risk of "false alarms".

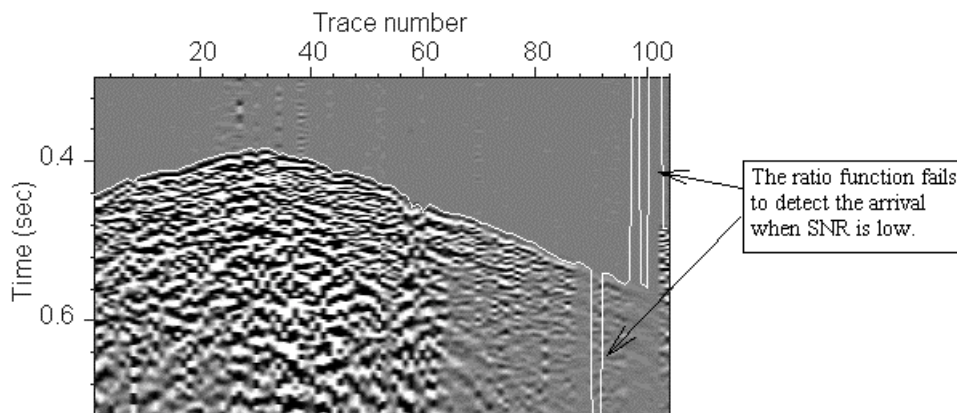


Figure 2.8 The picked result (the white curve) by using the two-sided ratio function detection. Data courtesy of BHP Coal (Appin Colliery).

There are a number of versions of the ratio function. Instead of taking the envelope function, the long-term and short-term average is sometimes obtained from the square of the envelope function (Baer and Kradolfer, 1987), and the absolute values (e.g., McEvelly and Majer, 1982) of the seismogram's amplitudes. Two-moving window lengths may be identical for a special case. In addition, Gu, Zhou and Zhang (1992) reported that they used two moving-windows both to the left side of current point k , the long-term average and short-term average are obtained from the square values of seismogram's amplitudes. The envelope function was believed more appropriate than the amplitude to measure of the instantaneous strength (Earle and Shearer, 1994). However, in practice, it is hard to say that one is much better than others as the *STA* and *LTA* are the averages of two term windows rather than the instantaneous values.

2.3.1.2 Methods for adjustment

After first stage processing, the onset time is picked at least approximately. The second stage is to evaluate the picking and adjust the estimated picks to apparent positions. Earle and Shearer (1994) calculated the average residuals between hand and automatic picking and applied a constant shift. Hatherly (1982) suggested using linear least-square prediction to evaluate the first stage picks; he then used a set of the first inflection points after the first kick to correct irregularities of the previous picking, and made uphole and reciprocal time corrections. Gu, Zhou and Zhang (1992) proposed the use of a dip angle scanning correlation algorithm to verify the first picks, and then used a peak value and an inflection correction method to refine the picks. Tu (1995) used a median filter to eliminate "jumpy" values.

2.3.2 Interactive Picking Methods

2.3.2.1 Envelope(/amplitude) threshold detection

One way to tackle the problems in first break picking is to train and supervise machines closely, if they are to cope with data variations. An interactive first break picking procedure involves the following steps:

Pre-processing: Seismic data can usually be pre-processed safely by subtracting instrumental drifts away from a zero-mean, and then be Hilbert-transformed to calculate seismic attributes such as envelopes. However, non-casual filters can throw false precursors ahead of the principle events.

Guided threshold detection: For any given shooting geometry there usually is a loosely defined boundary between the "noise alone" sector -- that before any signal could possibly have arrived from the source -- and a later sector within which it may be plausible to find signals buried in noise. This boundary is indicated by the "guide-line" shown in Figure 2.9(b). Instrumental spikes aside, the maximum of the envelope(/amplitude) of the signal-free part of each trace (before the "guide curve" in Figure 2.9(b)) is multiplied by a user-defined scalar (default 2) to set a threshold. A first approximation to the timing of the first break is given by the first instant after the guide curve, at which the trace's envelope(/amplitude) exceeds the threshold. In poor signal-to-noise conditions, the multiplying scalar can be reduced, at the price of increasing the user effort needed to pick the guide curve.

Phase adjustment: Skilled human observers can use powerful data adaptive "eye-ball" trace-to-trace correlation techniques to track first breaks back into the sub-unity signal-to-noise conditions that precede the envelope(/amplitude) threshold. These techniques are difficult, time consuming and subjective but they are none-the-less valid. Such a first break is indicated by the dot on the model arrival in Figure 2.9(a). A PC can be programmed to pick comparable points on neighbouring traces by cross-correlating the model arrival with its nearest neighbours. This operation adjusts the picks from previous pass to the ideal phase position indicated by the model.

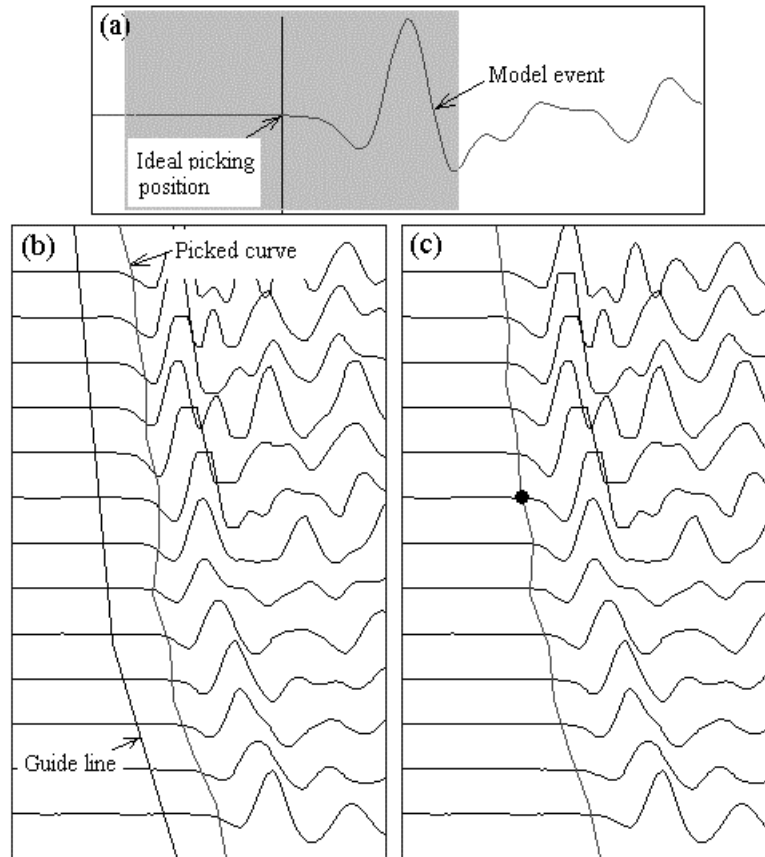


Figure 2.9 The picking procedure. The user picks the "Guide curve" before which no relevant energy could have arrived. After applying the envelope detector, the first pass picks are shown in (b). The model trace, shown in (a) with a vertical black line on the first break, is served as a reference for adjusting the first break picks on neighboring traces. The observer is free to pick as many model traces as the data quality might require, or as few as time constraints will allow. The final picks after the phase adjustment are shown in (c).

Arrivals vary in quality, and waveforms stretch. The range at which cross-correlation with a selected model arrival reduces to an unacceptable level changes from one seismic gather to another. There comes a point at which human intervention is required to pick another first break on a fresh model arrival. The number of model arrivals needed depends on user's judgment. The computer can easily be programmed to swing smoothly from one model to the next as first break picking progresses. Multiple model traces and local window lengths can be set by the user along the section to accommodate the variations of waveform. If there are still mis-picks after phase adjustment, they can be corrected manually.

Examples

Common shot gather

Figure 2.10 shows one common shot gather from the Tower 3D seismic survey carried out by BHP Coal. The top plot shows the picked curve of the first break on the section using the above procedure, the vertical lines on the arrivals shown in the windows at the bottom of the figure show the auto-pick positions. The white dot locates the model first arrival. A few sample traces of the result (without any further manual correction) are shown below the section. We can see that the picking result is satisfactory. If there are mis-picks, manual correction is needed.

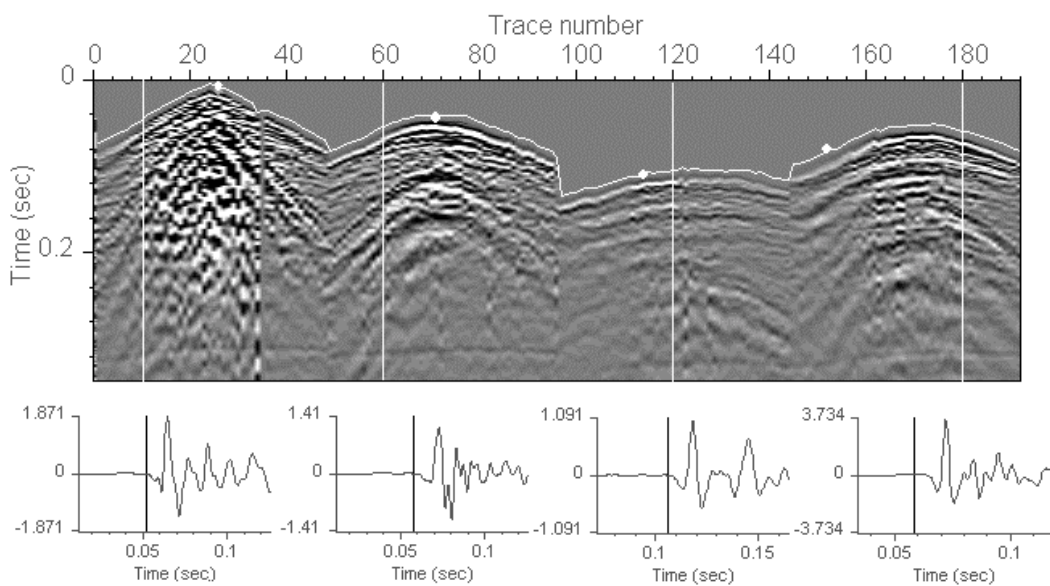


Figure 2.10 The first break picking result is shown on this common shot gather. The envelope threshold detection method was used. Sample pick traces and the model trace are shown below. The white lines mark the positions of the sample traces. The vertical line on these sample traces mark the final picking positions. The white dot on the section indicates the model trace position selected during picking. The data comes from BHP Tower Colliery.

Full waveform logging data

Figure 2.11 shows a portion of full waveform sonic data collected in a vertical water-filled hole drilled through sediments at Callide coal mine. The top plot shows the picked curve of the first break on the section using the above procedure, vertical lines on the arrivals shown in windows at the bottom of the figure show the auto-pick positions. The white dot locates the model first arrival. A few sample traces of the result are shown below the section.

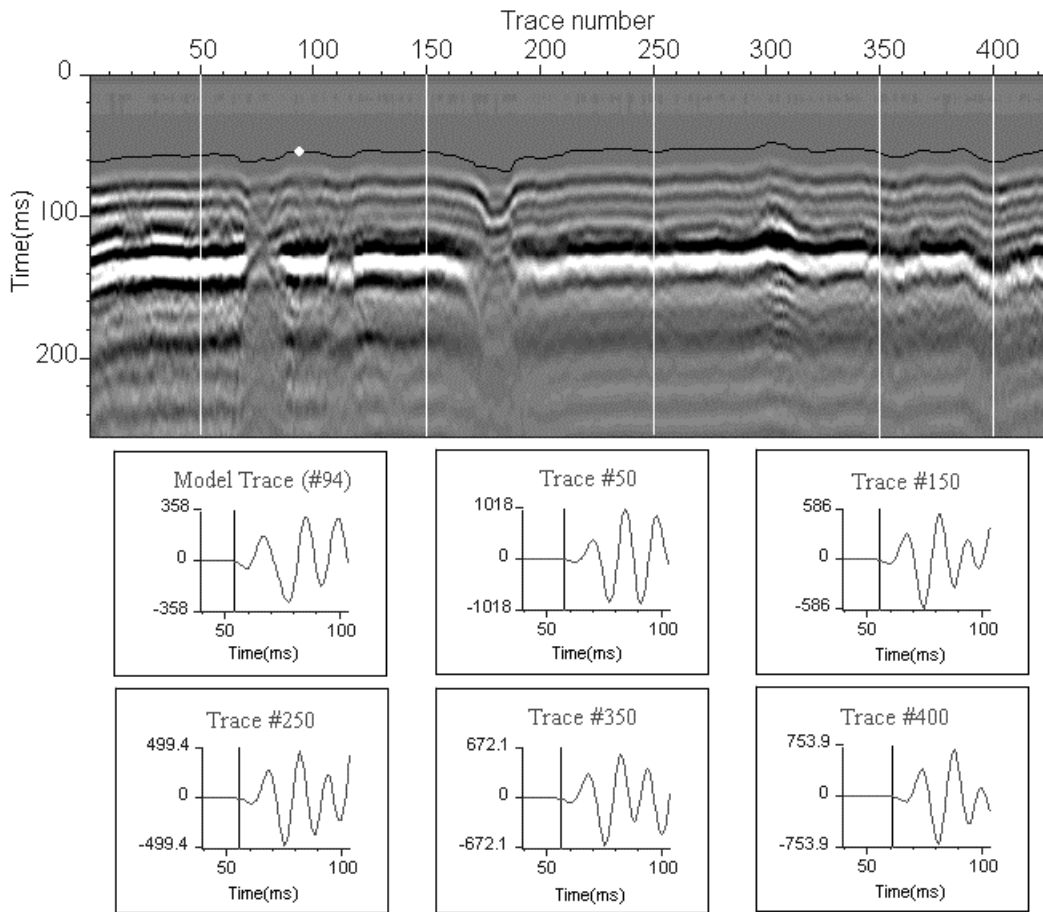


Figure 2.11 The first break picking result (the black curve) is shown on the full waveform sonic log section. Sample pick traces and the model trace are shown below. The envelope threshold detection method was used. The white lines mark the positions of the sample traces. The vertical line on these sample traces mark the final picking positions. The white dot on the section indicates the model trace position selected during picking. Data courtesy of Callide coal mine.

2.3.2.2 *The interactive ratio function detection*

The ratio function in Figure 2.8 is unstable when the SNR is low. One way to prevent the "jumping" is to force the computer to follow the coherent relationship of the data. It means that human guidance should be given. To implement the idea, a rough curve along the first arrival can be drawn manually. A search range is determined by this user-drawn curve. The computer then picks the first value that is higher than the threshold only in this limited range. Figure 2.12 illustrates the idea and shows an improved picking from Figure 2.8. A threshold of 70 percent of the maximum ratio value and 0.2 seconds (40 samples) for the search length was used in this example.

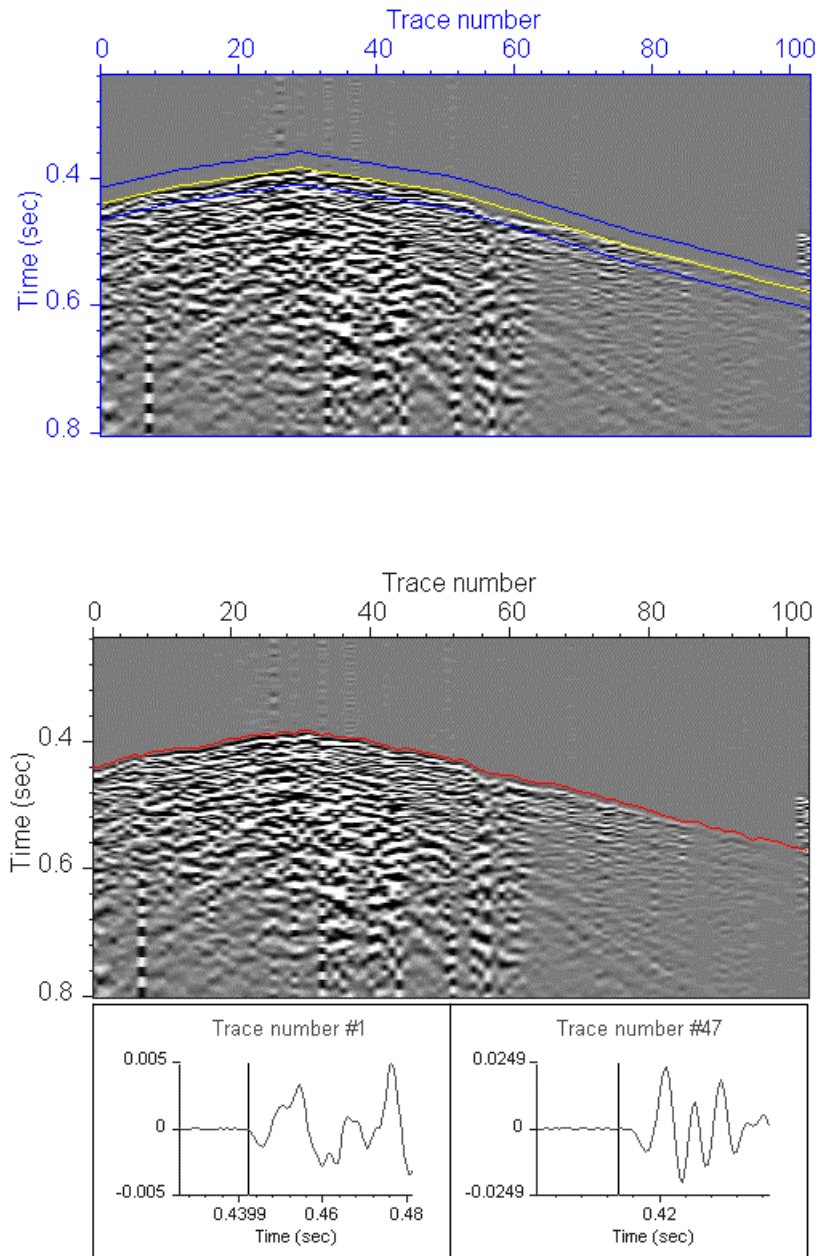


Figure 2.12 The upper diagram illustrates the idea of user guidance using the data in Figure 2.8, while the lower diagram shows the re-picked result.

2.3.3 Other Measurement Positions of the First Arrival

The earth has inhomogeneous, complex geological structures. The energy of the first arrival spreads as a wavetrain. Scattering and dispersion make tracking of the peak of the envelope(/amplitude) of the real signal easier than tracking the first break point, as the threshold setting is more straightforward. In practice, a significant peak or trough of the first arrival is also often measured.

One way of estimating the first break is to pick a local peak or trough and shift the picked position by a constant time backward. The local extreme can be detected when the first derivative of the function turns to zero and the computer finds the extreme in a pre-defined range. Figure 2.13 shows the general idea. Care must be taken to restrict the range to avoid the chance of cycle skipping, i.e., No. 2 peak is taken instead of No. 1.

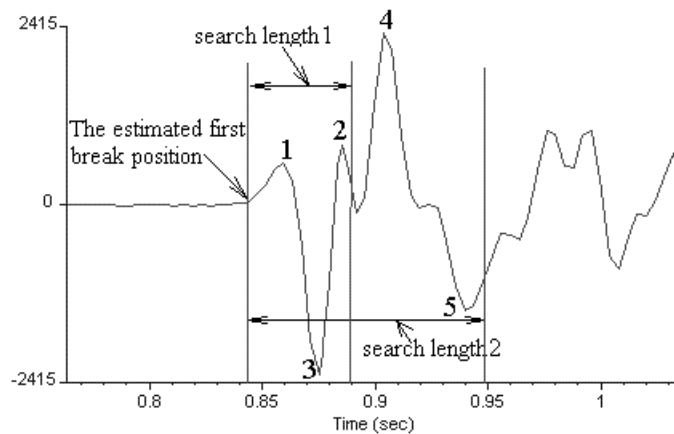


Figure 2.13 A diagram of the local maximum (/minimum). The search length determines the range the computer looks for the maximum value. Numbers 1-5 mark the peak and trough positions for two search lengths.

2.3.4 Discussion

The first break picking methods, the interactive ratio function detection and the envelope (/amplitude) threshold detection, were discussed. The amplitude threshold and the envelope threshold methods give similar results. However, the amplitude threshold detection shows a slightly better result than that of the envelope, as any filtering process might affect the picking result. The interactive ratio function can be used alternatively, but all of them need fine adjustment.

Nominating a model trace is important for fine adjustment. In this chapter, the closest model is used. In order to create a model that can characterize the gradual changes for each trace, one possible option is to derive a model of each trace from pre-selected models by interpolation. The new model created in this way may be more appropriate than the one selected by the closest distance.

2.4 INTERACTIVE SEISMIC EVENT TRACKING

Detecting the second and later arrivals is also a difficult task. When the shooting geometry is simple, later arrivals follow simple, often hyperbolic curves. Picking such seismic events is not a difficulty, as we can track the lateral coherence from trace to trace. However, when the shooting geometry becomes complicated, cusps appear with sharp changes in curvature and crossing events clutter up. In addition, multiples and the coda of preceding arrivals and noise make seismic event detection more difficult.

None of the automatic event tracking methods is perfect, as they break down under some circumstances. The best way to achieve robustness is to implement a human-interactive, semi-automatic method. The basic method for detecting a seismic event is to design a correlation detector which measures the best match position of two signals, or in other words, to measure the time delay between two signals. The cross-correlation is considered unreliable when the SNR is low and noises are correlated. Before we can decide whether the cross-correlation method is applicable, it is necessary to examine the conventional windowed cross-correlation function.

2.4.1 The correlation method

2.4.1.1 Windowed cross-correlation

Cross-correlation is a common method of finding time delay. The cross-correlation function measures the similarities between two signals at various time lags and the estimated delay time is taken when the maximum value of the cross-correlation is found. For two receivers, the measurements of a signal $g(t)$ and the same signal $h(t)$ with a time delay t_0 can be written as:

$$\begin{aligned}g(t) &= s(t) + n_1(t), \\h(t) &= s(t - t_0) + n_2(t).\end{aligned}\tag{2.8}$$

where $n_1(t)$ and $n_2(t)$ are unknown noise sources. The cross-correlation function $R_{g,h}(t)$ of two functions $g(t)$ and $h(t)$ is defined as (Bracewell, 1986):

$$R_{g,h}(t) = \int_{-\infty}^{\infty} g(u)h(u+t)du\tag{2.9}$$

Substitute Equation (2.8) into Equation (2.9) and assume the noise sources are zero-mean stationary random processes (Nikias and Pan, 1988), we have

$$\begin{aligned}
 R_{g,h}(t) &= \int_{-\infty}^{\infty} (s(u) + n_1(u))(s(u+t-t_0) + n_2(u)) du \\
 &= \int_{-\infty}^{\infty} s(u)s(u+t-t_0) du = R_{g,g}(t-t_0)
 \end{aligned}
 \tag{2.10}$$

Therefore, when the noise sources are independent with records, cross-correlation between two records is equal to auto-correlation at time delay t_0 , and $R_{g,g}(t)$ shows a peak at the time delay position. In practice, recorded signals have finite length and noise sources are not necessary zero-mean stationary random processes. The peak at t_0 might not show. It is common in a seismic section that a signal has similar wave patterns appearing at different times, and the cross-correlation function may not pick up the one that we wish to detect. Robinson (1978) discussed the cross-correlation in an automatic lithostratigraphic correlation study. He pointed out the pitfalls in applying the cross-correlation function, such as mis-correlations caused by unrestricted correlation range and by noise. A number of good suggestions like using prior information to restrict the correlation range were made.

2.4.1.2 The windowed cross-correlation method with interaction

A semi-automatic seismic event picking method is proposed by employing a windowed cross-correlation function. The computer searches for the best match within a window between the input signal and a model event. The model(\models) is selected from the record. The target event on the model trace is picked manually. The windows used here are defined by tracing a guide curve along the path of the event. The procedure is shown in Figure 2.14. When a number of models are needed, each trace on the record is cross-correlated with its nearest model.

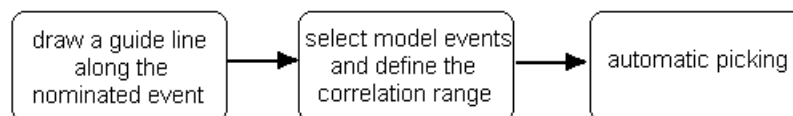


Figure 2.14 The picking procedure based on correlation.

Figure 2.15 is an example showing a portion of full waveform sonic data collected at Callide coal mine. The P-wave, S-wave and tube wave are evident on the time section. The desired target is the S-wave. The top plot shows the picked curve of the S-wave by

following the procedure in Figure 2.14. The two black zigzag lines are the user-defined correlation range. The locations of the zigzag lines are determined by the guide curve (the guide curve was not shown on this figure). The white dot on the picked curve indicates where the model arrival was taken from. The target event was picked successfully (the white curve).

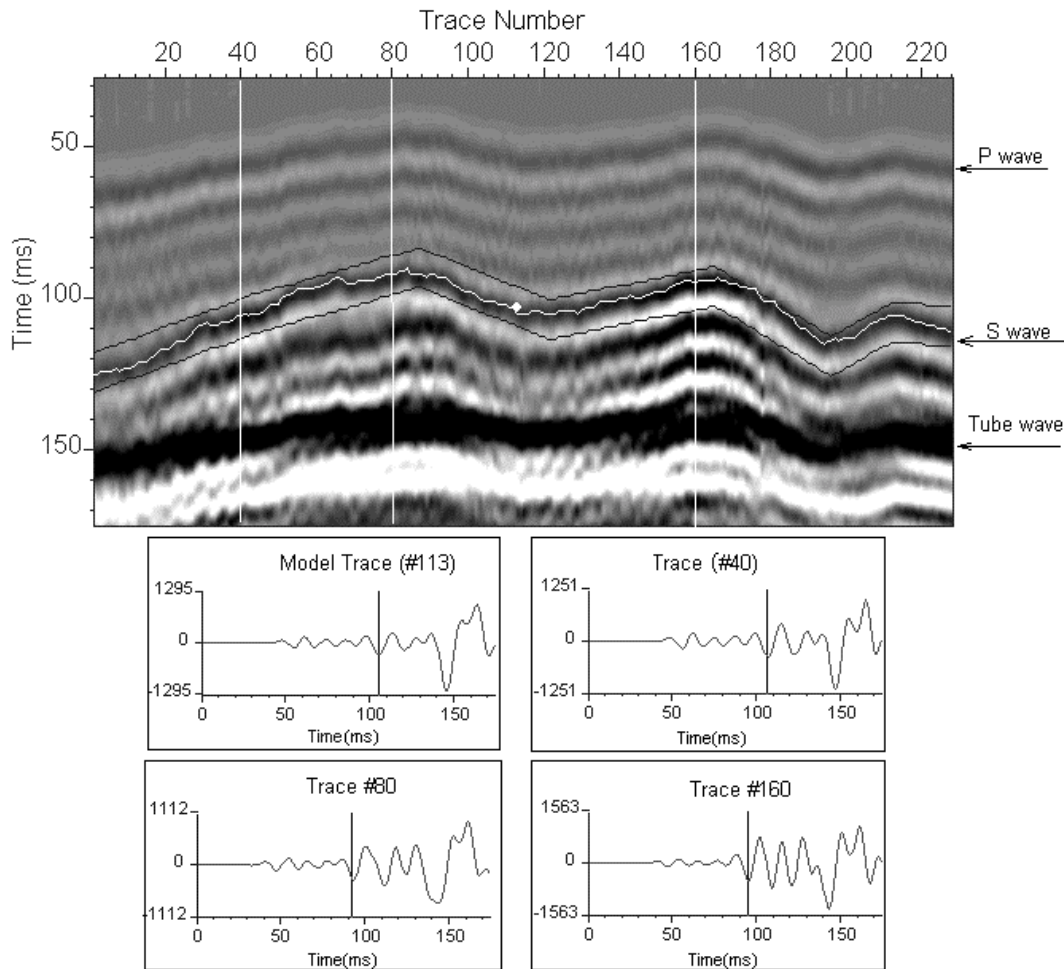


Figure 2.15 S-wave arrival picking within the user-defined correlation range marked by black zigzag lines. The white spot indicates the position where the model arrival was taken. The picked S-wave is shown by the white curve. The model trace and three example traces are shown below the section. Data courtesy of BHP Appin Colliery.

2.4.2 The Instantaneous Phase Picker

2.4.2.1 Instantaneous phase

It is possible to track seismic events by detecting the discontinuity of the instantaneous phase. According to Bracewell (1986), a complex function $q(t)$ can be obtained from a real function $x(t)$ by,

$$q(t) = x(t) - iy(t) \quad (2.11)$$

where $y(t)$ is the Hilbert transform of $x(t)$ and their relationship is,

$$y(t) = \frac{-1}{\pi} * x(t), \quad (2.12)$$

The counterpart of $(-1/\pi)$ in the Fourier domain is $i \operatorname{sgn}(\omega)$ and

$$i \operatorname{sgn}(\omega) = \begin{cases} i & \omega > 0 \\ -i & \omega < 0 \end{cases} \quad (2.13)$$

Therefore, only the phases of $y(t)$ are changed by $\pi/2$ according to the sign of ω and the amplitudes of spectral components are unchanged.

From a complex function $q(t)$, instantaneous phase can be represented as (Yilmaz, 1987)

$$\varphi(t) = \arctan[y(t)/x(t)]. \quad (2.14)$$

The instantaneous phase is independent of the reflection strength $a(t)$. The instantaneous phase display can bring weak signals (small amplitudes) and strong signals into uniform strength in display. A weak event can be seen clearer in the instantaneous phase display.

Computationally, the determination of instantaneous phase is interesting. In C++, the `atan` function returns a value between $-\pi/2$ and $\pi/2$, while the function `atan2` requires two input values: the imaginary part y and the real part x of an analytical signal. The function `atan2` returns a value between $-\pi$ and π excluding $-\pi$. The amplitude of the discontinuity is about 2π . The `atan2` is often used for the computation of the instantaneous phase. This actually makes the frequency of the instantaneous phase discontinuity match with the period of the waveform.

Figure 2.16 shows the comparison between the image display and the instantaneous phase display. The three white arrows in Figure 2.16(a) indicate three events that have in different strengths (i.e., different reflectivity). In Figure 2.16(b), the instantaneous display shows the three events (marked in black arrows) with the same strength and with

clear edge. Wiggle displays in Figure 2.16(c) and (d) are used to illustrate the relationship between the conventional and the instantaneous phase waveform corresponding to Figure 2.16(a) and (b). The complicated waveforms appear simpler in the instantaneous phase presentation: the phase shows a monochrome increase with a discontinuity at the trough positions.

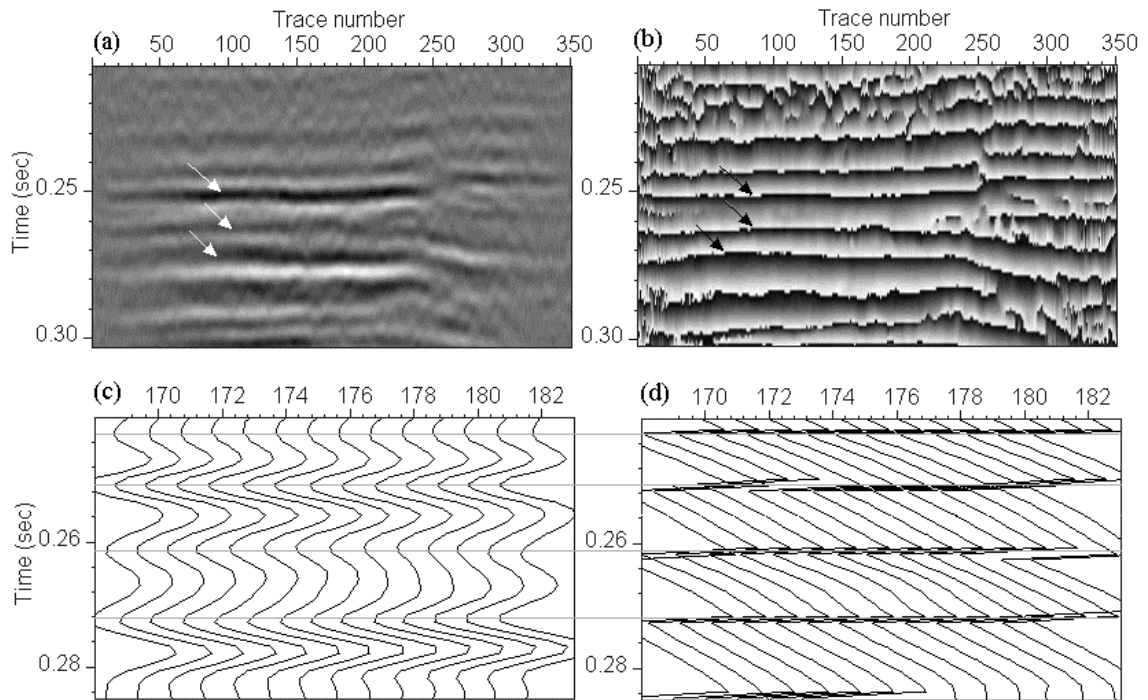


Figure 2.16 The comparison between the image display and the instantaneous phase display. The arrows in (a) and (b) show three events in two different displays. (c) Portion of section (a) displayed in wiggles. (d) Portion of section (b) displayed in wiggles. The horizontal lines across the wiggle displays are used to mark the trough of each event in the real signals in (c) and the corresponding positions in the phase display (d).

2.4.2.2 Event detection by using the instantaneous phase

An instantaneous phase picker tracks abrupt changes of instantaneous phase. This method is designed for picking the troughs or peaks of amplitudes of the target event. The picking procedure is illustrated in Figure 2.17. The calculation of instantaneous phase using atan2 simplifies the picking process as the discontinuity points of the instantaneous phase correspond only to the troughs of the signal. The target event is marked by a guide curve. The search length for finding the discontinuity can be defined by the user. There are two input parameters in this operation: the search length and the

pick position (peak/trough). The search window length centered on the guide curve can be specified by the user. The computer then searches for possible phase jump positions which exceed the threshold. The value 5.5 is used as the default threshold value because a period represents 2π . After the phase jump positions are located for each trace, the one closest to the guide curve is picked. Finally, the estimated picks are re-arranged to the closest extreme of the signal amplitude. 3-point parabolic fitting is used to locate the true local trough/peak.

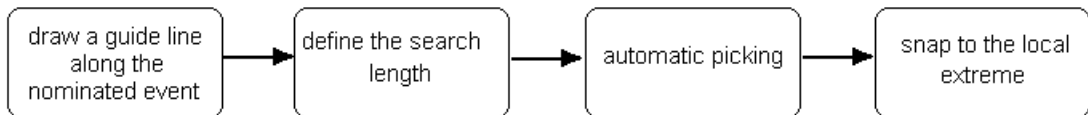


Figure 2.17 The picking procedure based on the discontinuity of the instantaneous phase.

Figure 2.18 shows a section of 3D seismic survey at Burton Coal mine. There is a graben-like structure. A guide curve was drawn (the yellow curve) by the user, the picked result is shown by the red curve.

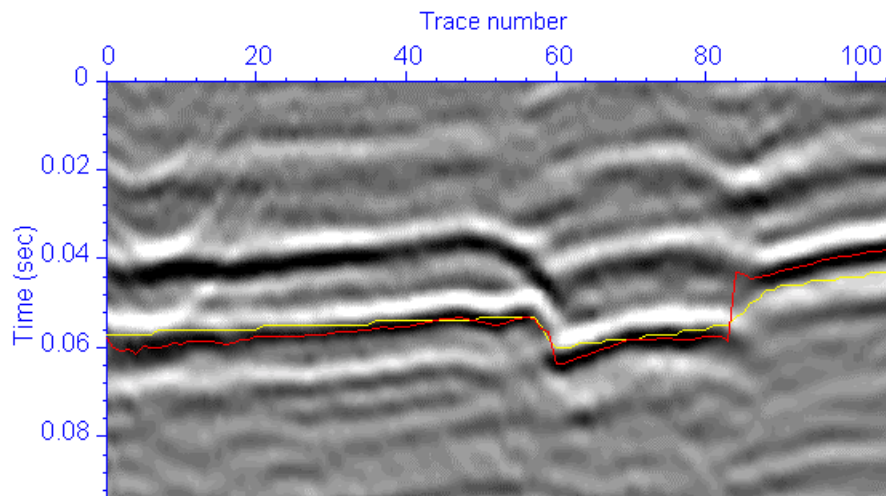


Figure 2.18 The result by using the instantaneous phase picker is shown in the image display and the instantaneous phase display.

The instantaneous phase picker can also be used to pick first arrivals if the first trough or peak position is required. A good example can be seen from Figure 2.19, which is a portion of a full waveform sonic data from Callide coal mine. The dark grey curve shows the final picks.

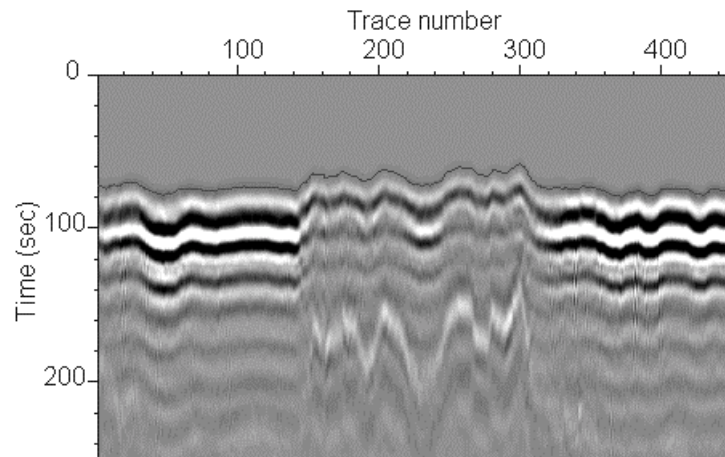


Figure 2.19 The first arrival of the full waveform sonic log segment was picked (the dark gray curve) by the instantaneous picker. Data courtesy of Callide coal mine.

2.4.2.3 Discussion

The correlation method and the instantaneous phase picker are two alternative tools for 2-D seismic event picking. The correlation method is based on the cross-correlation theory and it performs well in ideal conditions. However, the method is sensitive to signal-to-noise ratio and waveform changes. In some circumstance, mispicks are inevitable and need manual correction. The interactive method introduced in this chapter allows the interpreter to correct the mispicks easily as illustrated by Figure 2.20.

The instantaneous phase is easier to use. In numerous tests, it has been proved to have fewer mispicks when it is compared with the correlation method, because the instantaneous display has a more stable boundary between two adjacent events, especially when waveforms change and the signal-to-noise ratio is low. This can be seen from Figure 2.16.

A guide curve traced by the interpreter is a very important step, the picking accuracy depends on it. It is recommended to trace a target event as accurately as possible, it does not need much effort to do it but it benefits the picking process greatly.

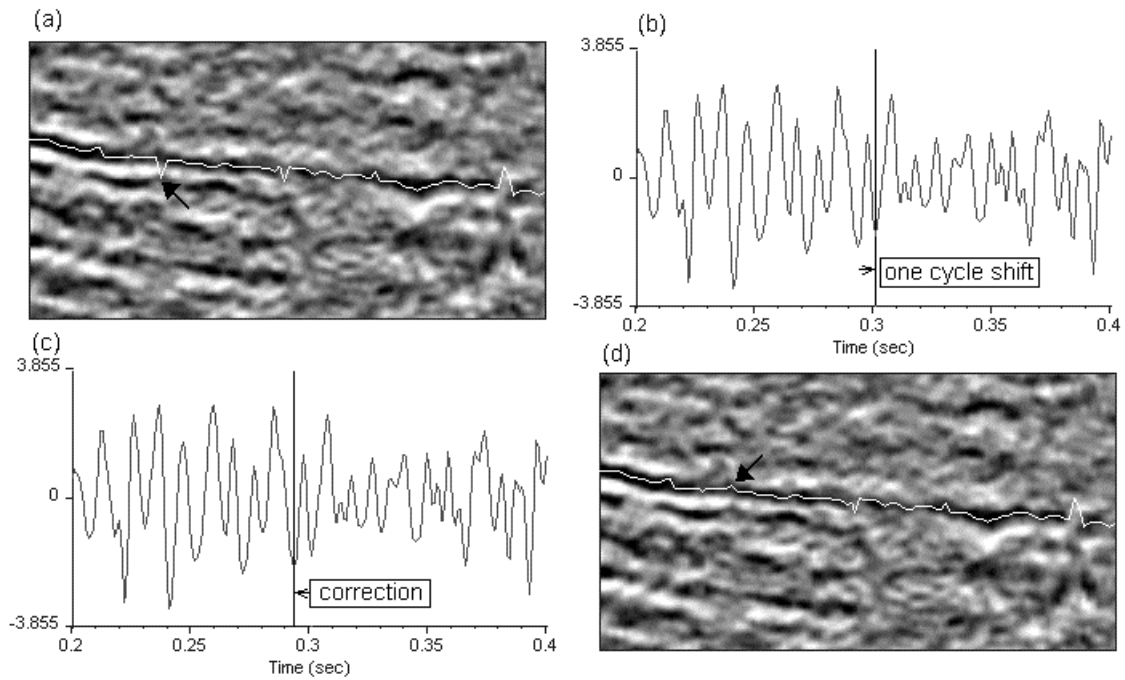


Figure 2.20 The interactive correction process. The black arrow on the image of (a) indicates a mispick occurred in the picking process. This mispicking position can be easily located as shown by (b) which indicates that the picked position had one cycle shift to the right. After moving the pick position manually one cycle to the left (c), the mispick is corrected (d).

2.5 CONCLUSIONS

A completely automatic method is ideal but it is a difficult goal. Picking operations are interpretative. Machines can cope effortlessly with enormous data volumes, but they cannot mimic the ability of a trained interpreter on dealing with various complex situations. Human guidance and intervention is essential, and machines are only an aid. A well designed picking machine should permit not only the easy detection, investigation and correction of event picking errors, but should also allow human guidance levels to be raised smoothly as lateral coherence diminishes and / or jamming by clutter increases. Design of picking algorithms was a main objective of this chapter.

The candidates, the ratio function method and the amplitude method for the first break detection, the windowed cross-correlation method and the instantaneous phase picker for other arrivals except the first break, have been tested to extract arrival times from full waveform sonic logs, reflection and tomographic in-mine borehole radar surveys. The

methods perform well in precision and speed. The picking scheme has proved flexible enough to enable observers to cope well with arrival identification.

CHAPTER 3 3-D HORIZON TRACKING

3.1 INTRODUCTION

An early 3-D seismic survey was shot by Exxon in 1967 (Dorn, 1998). Since then, 3-D data have played an increasingly important role in seismic interpretation. They are routinely acquired nowadays in the petroleum industry. 3-D surveys provide accuracy and reliability in seismic interpretation, and reduce the risks in development and exploitation. A 3-D seismic survey is especially beneficial for the detailed interpretation of smaller targets (Nestvold, 1992).

Time-derived horizon attribute analysis in 3-D interpretation is useful in defining subsurface targets. Rijks and Jauffred (1991) give a good discussion on attribute extraction strategy and the use of horizon attributes for fault interpretation. The precise measurement of two-way time values from the target horizon is essential because it ensures that information, such as dip magnitude and dip azimuth, can correctly construct a detailed subsurface image.

Geological conditions are crucial in appraisal and development planning in the coal industry. Correct identification of coal seam structures and subtle faults can offer good guidance for mine planning (Zhou and Hatherly, 2000). Interactive 3-D horizon tracking techniques play an important part in 3D seismic data interpretation.

Dorn (1998) provides a good review of horizon interpreting techniques. However, the computer implementation of automatic volume tracking has hardly been discussed in the open literature. In this chapter, two interactive 3-D horizon tracking methods on PC's are introduced and a few examples are given.

3.2 HORIZON TRACKING IN A 3-D DATA VOLUME

In a typical 3-D land survey over comparatively shallow coal measures, the receiver cables and shots frequently are arranged perpendicular to one another. This kind of

layout is known as swath shooting (Dobrin and Savit, 1988). Traces in 3-D data are rarely pre-stack migrated. More commonly they are sorted into common cell (bin) gathers. This computationally intensive but now routine procedure usually is carried out by contractors, using purpose designed commercial software such as Advance Geophysical's Promax®. Binning is not formally an inversion procedure, but it does reduce field data successfully if the geology is largely layer-cake. Binning compares to but differs geometrically from the common-middle point gathers for 2-D surveying.

The output from a commercial processing operation is a 3D grid of voxels, with a volume measured in hundreds of megabytes. The data volume confronts mine site interpretation geologists (who usually are only equipped with PC's) with a daunting but tractable task.

A grid covering the entire survey area is composed of rectangular cells (see Figure 3.1). In 3-D seismic interpretation we are dealing with vertical sections (both in-line and cross-line sections) and horizontal sections (time slices).

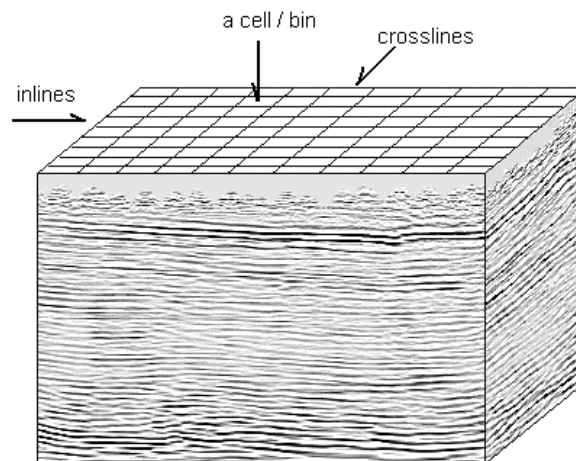


Figure 3.1 A sketch of common bin gathers in 3-D surveys

3.2.1 3-D Horizon Model Construction and Auto-picking

Figure 3.2 illustrates a model of a subsurface cut by in-line and cross-line sections. Normally, a 3-D data volume contains hundreds or even thousands of vertical sections. Those in-lines and cross-lines form a grid on the surface. A reflecting surface may be

any irregular curved layer. The reflections from this horizon will be evident on most vertical time sections. Once a horizon has been identified, a 3-D subsurface can be constructed by measuring the two-way reflection time of the target horizon from every point of the grid. There are several ways of mapping horizons. Beside voxel tracking⁷ and surface slicing (Dorn, 1998), horizon auto-picking is the most efficient tool for conveying the shape of a buried surface to an interpreter.

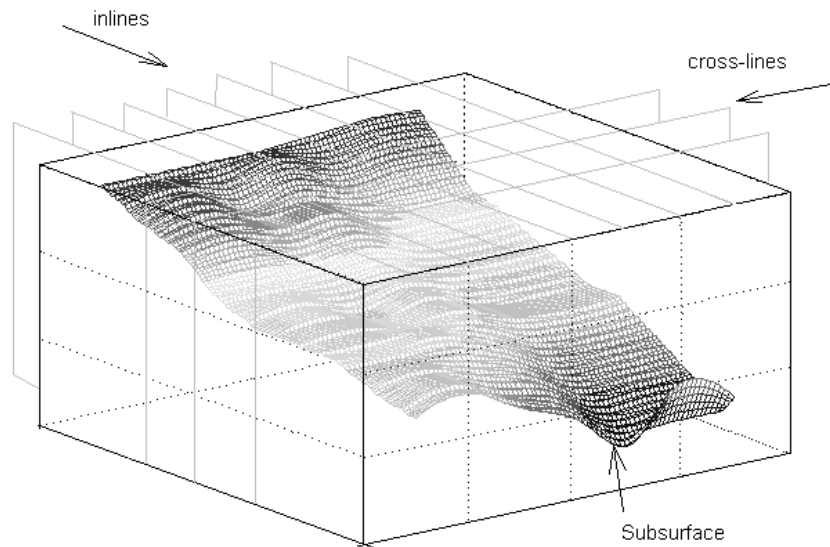


Figure 3.2 An illustration of a subsurface cut by in-lines and cross-lines. The in-lines and cross-lines construct a grid on the surface which covers the whole survey area.

3.2.2 3-D Horizon Tracking

3.2.2.1 *Related work*

Dorn (1998) divided automatic horizon picking methods into two classes: feature trackers and correlation trackers. The former search for a similar configuration of samples, i.e., a peak/trough, a zero-crossing etc., with a dip window. The latter is based on correlation techniques. A correlation horizon tracker takes a portion of a trace around the seed pick and correlates with neighbouring traces in a specified widow. Autopickers, as Dorn (1998) pointed out, are all sensitive to noise, and the path which the autopicker follows should be considered carefully.

⁷ A voxel is a three-dimensional pixel with dimensions equal to the bin spacing and sample interval (Kidd, 1999).

Rijks and Jauffred (1991) reported an optimal way to extract seismic attributes used by Shell. In their interpretation strategy, a number of pre-picked sections of the target horizon formed the control grid, which was used as input to an automatic tracking program which interprets the horizon over the entire data. Shell called their method the "horizon-oriented" approach.

The fundamental value of horizon autopickers, as Herron (2000) has pointed out, is that they quickly and accurately perform straightforward event correlation, thereby allowing an interpreter to devote greater attention to more difficult and complex tasks. It is an acceptable concept that autopickers cannot perfectly pick on their own, in the face of low signal-to-noise ratios and complex geological features. However, an autopicker can be more efficient and accurate if the interpreter holds tight control over the track. This requires user-machine interaction.

3.2.2.2 Interactive Horizon tracking method

3.2.2.2.1 Construct a control grid

The interactive 3-D horizon tracking method developed in this study is similar to the horizon-oriented approach (Rijks and Jauffred, 1991). Since the main difficulty in automatic horizon tracking is that a subsurface may have faults or discontinuous structures, autopickers often will fail to follow the right track. One solution to this is to define a control grid, which is used to define a 3D search zone for the autopicker.

Firstly, a general knowledge of the target horizon is needed. This requires the interpreter to scan vertical sections of the 3D volume carefully before the autopicker is launched. Then, a small number of 2-D seismic sections are selected from the volume in a coarse grid. These sections are called model sections. Their spacing depends on the quality of the data and the features of the stratigraphic structure. For example, if the horizon is almost planar or smoothly steep, a broad grid will do the job. On the contrary, a tight grid should be used in areas covered by faults or characterised by clutter and/or low SNR. Uniform control grids rarely are necessary because data quality usually varies significantly over the search volume.

Secondly, the target horizons on these 2-D model sections are traced. A control grid is then formed by linear interpolation across each vertical section parallel to the model sections. Figure 3.3 shows how seven in-line sections (model sections) from Figure 3.2 can be assembled to form the control grid. The thick curves represent the traced target horizon on each model section (inline direction), the solid black dots show the direction of linear interpolation between model sections.

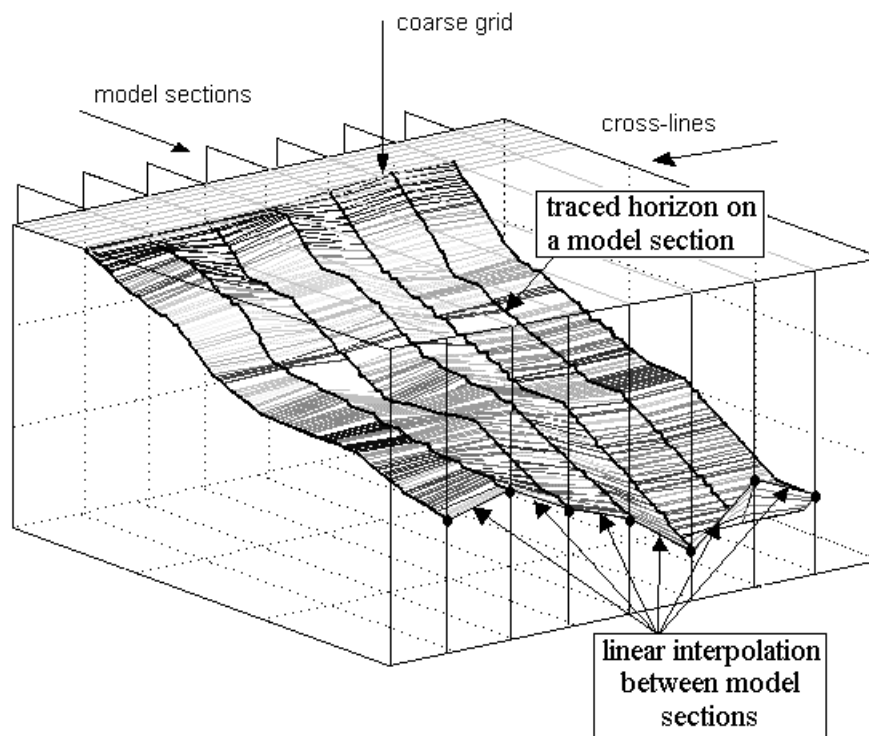


Figure 3.3 The coarse grid forms a control grid used for automatic horizon tracking.

3.2.2.2.2 Automatic tracking

Once the control grid is defined, a search zone can be defined along the time direction at each grid point, over which the correlations are sought to define the arrivals from the target horizon. This operation not only saves time on data scanning, but also reduces mispicking on similar events in the neighborhood. The control grid allows 2-D picking methods to be applied directly to map 3-D horizons. If the 2-D correlation method is used, the model events (called *seeds* in Dorn, 1998) are selected from the model sections. The control grid and the model events are used as references to perform correlations in their neighbourhood over the whole 3D data volume. The 2-D instantaneous phase picker

is the picker of choice if the SNR permits, because it is less computationally expensive, and therefore faster than the correlation method. Because the model is so simple -- an elementary phase change -- instantaneous phase pickers do not need the user to pick any model events.

The 3-D horizon tracking methods designed were embedded in *SeisWin*, and they were tested on seven recent 3-D land seismic reflection surveys which were conducted over faulted coal measures. The picking results from four of them will be shown here. The reader should be aware that all the 3-D displays in this chapter were produced by linking *SeisWin's* output to a widely available low cost (AU\$575) high quality display package called "Surfer®" { sold by Golden Software Inc.}.

3.2.3 First 3-D seismic survey in Appin area 4

The 2-D correlation method was tested using 3-D data collected by BHP coal at Appin Colliery Area 4 in February 1997. This was the first production 3-D seismic survey over a proposed extension to a coal mine in Australia⁸. The target reflections are from the Bulli seam. In this test, the control grid was made up of only 5 model sections, selected from 100 inline sections. Two model traces selected from each in-line model section were used. The events were picked with correlation method. Figure 3.4 shows the two-way reflection time contours without any manual corrections. The result is good as there are no obvious sharp changes in curvature or discontinuities on the map.

A few picked inline sections are displayed in Figure 3.5 as examples of the autopicking on vertical sections. The quality of this set of data is very good, as the SNR is high and there are no dramatic waveform changes of the horizon from the target Bulli seam reflections. The instantaneous phase picker was also tested and gave a similar result.

⁸ Experimental coal 3D seismic surveys at Appin and Newlands coal mines were conducted by Dr Peter Hatherly in the early nineties.

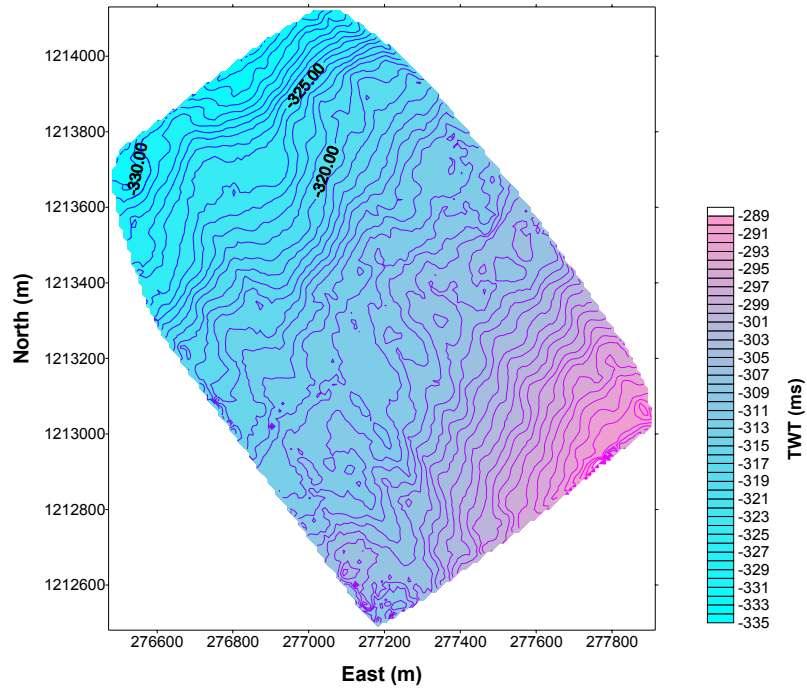


Figure 3.4 The automatically picked Bulli coal seam surface for the first 3D seismic survey at Appin Area 4 is displayed as a two-way reflection time contour.

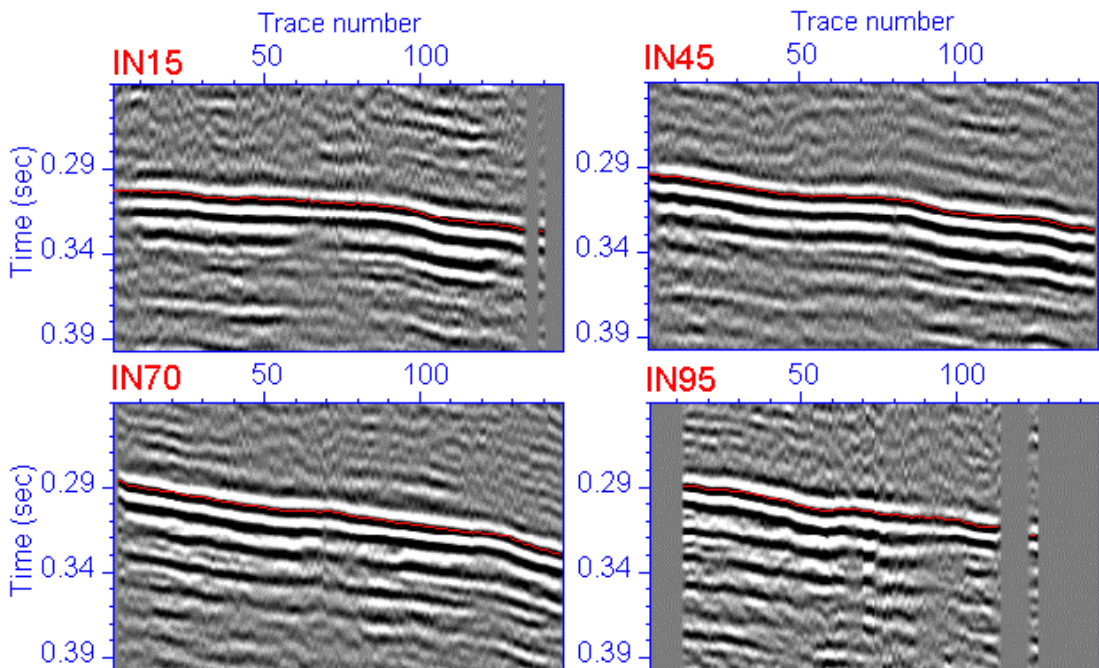


Figure 3.5 Examples of picked results (in red) on four inline sections for the first 3D seismic survey at Appin Colliery Area 4. The red label at each top left-hand corner of the image represents the corresponding inline number.

3.2.4 Second 3-D seismic survey in Appin area 4

Another 3-D seismic survey in Appin Colliery was conducted by BHP Coal in November 1997. The survey area lies to the southwest of the first 3-D seismic survey. The processed 3-D data has 184 in-line sections and 192 cross-line sections. Again, the target reflections are from the Bulli seam. This set of data is not as good as the first one. The SNR is low especially in the first 50 or so sections.

To pick the Bulli reflections, the model sections were selected at intervals of every 10 sections in the in-line direction except for the first 50 sections, which were picked interactively at non-uniform spatial intervals to screen out poor quality regions. Two model traces were defined for each model section. It took only 8 minutes to perform the entire 3-D picking process (Another 6 minutes were required to produce the contour map by applying the software Surfer).

The picked result is presented in the contour map shown in Figure 3.6. The many dark regions on the map are due to a limited display range and to mispicks. The picks on six sample sections are shown in expanded form in Figure 3.7. The maximum fluctuation on the picked curve is around 0.01 seconds. The color change of the picked event shows the variations of amplitudes and waveforms. The waveform variations cause much of mis-picking using the correlation method.

The instantaneous phase picker was also applied to this data set to map the Bulli reflections. The results are shown in Figure 3.8 and Figure 3.9. These are obviously better on the contour map where the contour curves are smoother, and fewer black spots can be seen. This is probably due to the fact that the instantaneous phase picker is less sensitive to the SNR. Figure 3.10 shows the comparison between the amplitude display and the instantaneous phase display. The instantaneous phase display has a clearer edge for a particular event and is easier to detect.

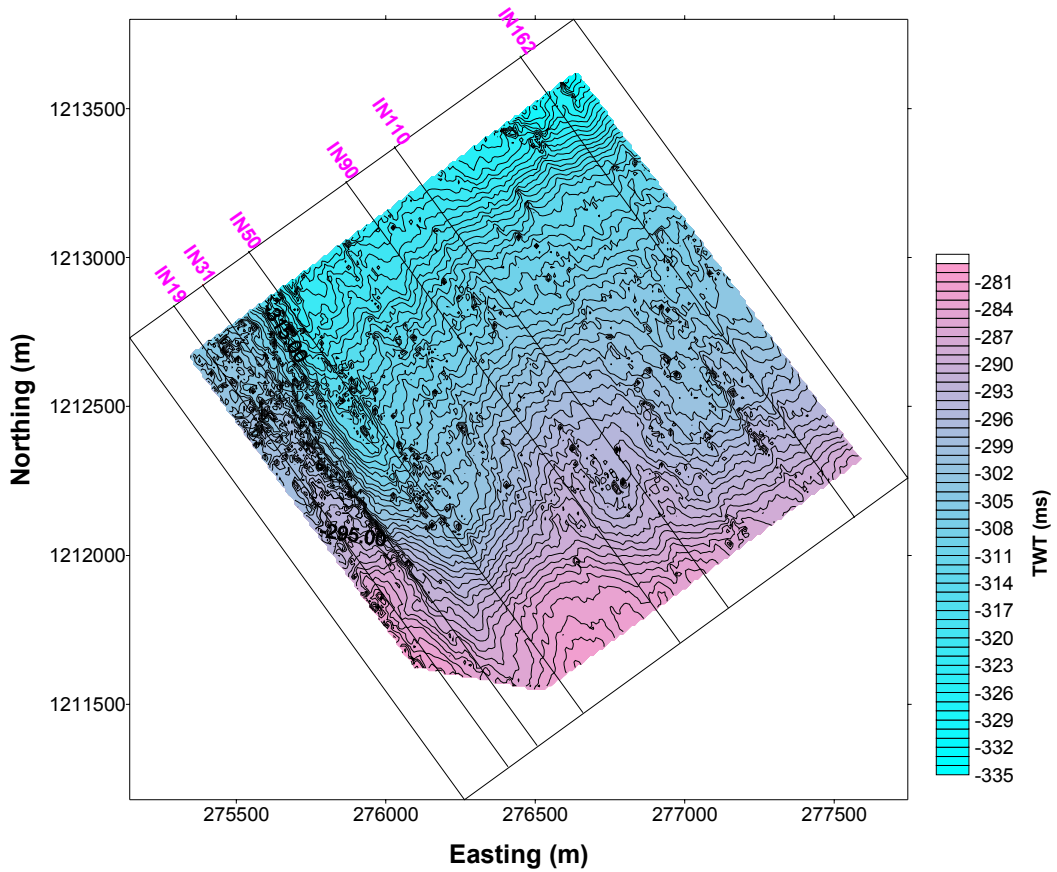


Figure 3.6 The contour map of reflection times for the Bulli Seam for the second 3D seismic survey at Appin Colliery, generated by the correlation method.

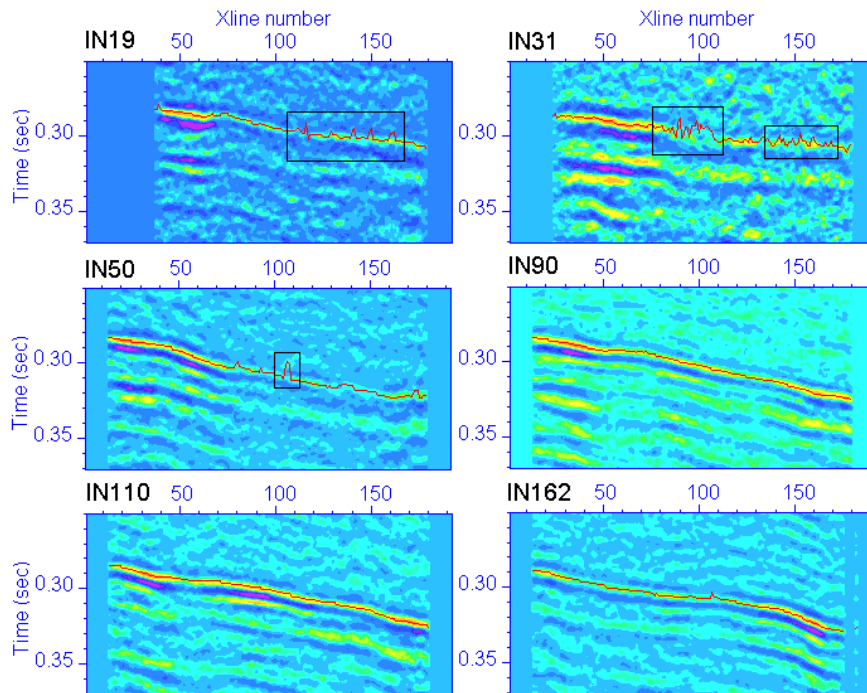


Figure 3.7 Examples of picked results shown on inline sections for the second 3D seismic survey at Appin Colliery. The label at each top left-hand corner of the image represents the corresponding inline number. The mispicks are marked by black rectangular areas.

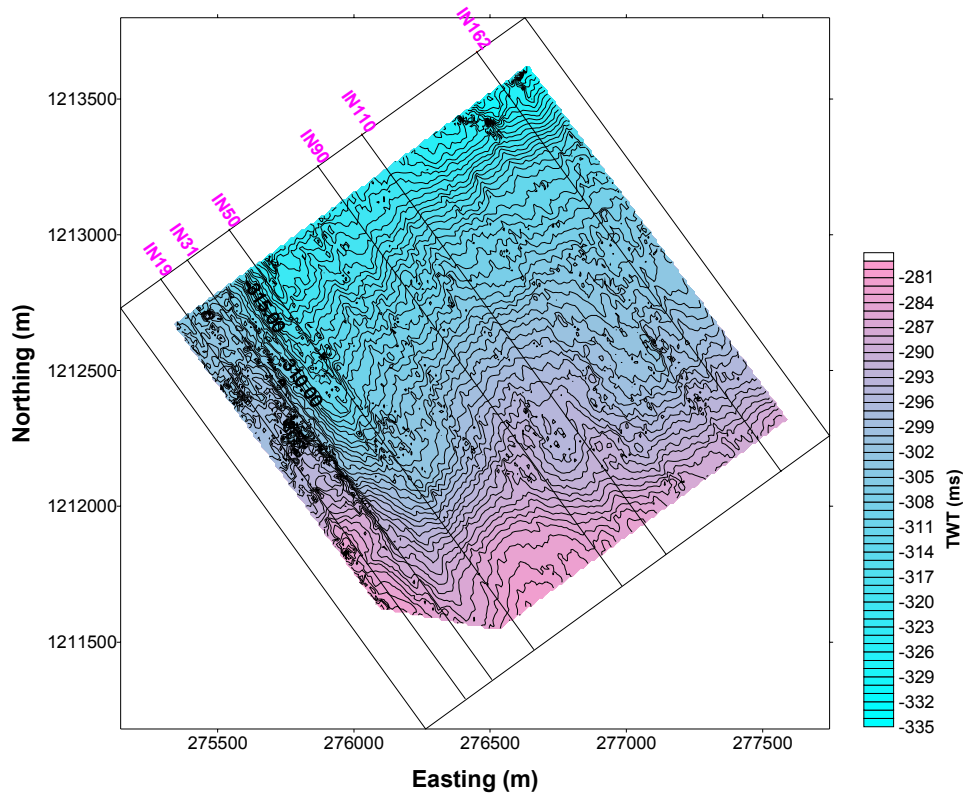


Figure 3.8 The contour map of reflection times for the Bulli Seam for the second 3D seismic survey at Appin Colliery. The reflection times were obtained from the instantaneous phase method.

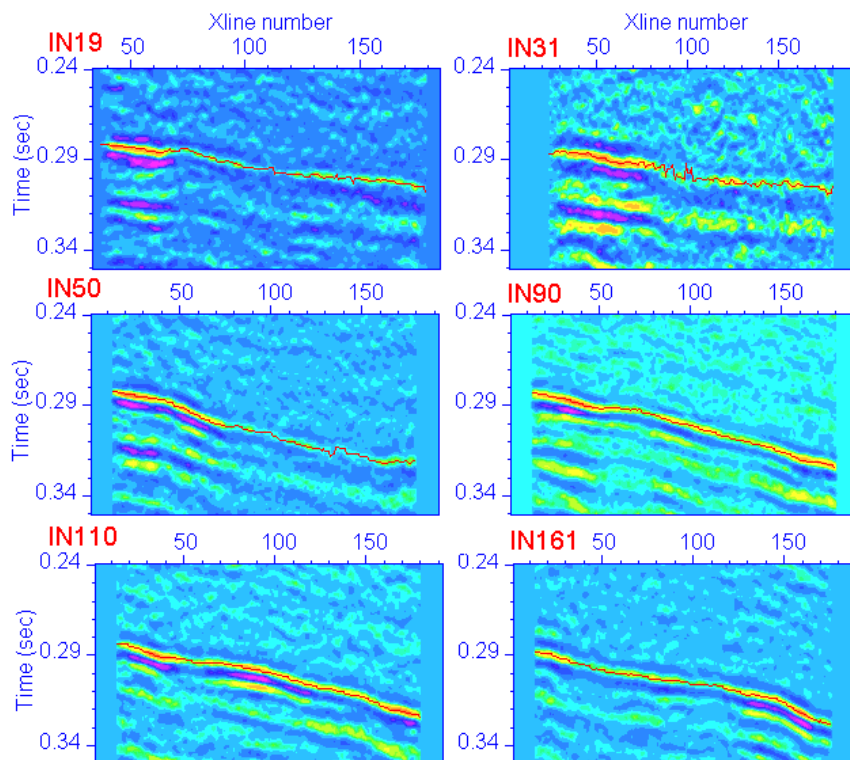


Figure 3.9 The picked result from the instantaneous phase method on some sections. The red label at each top left-hand corner of the image represents the corresponding inline number.

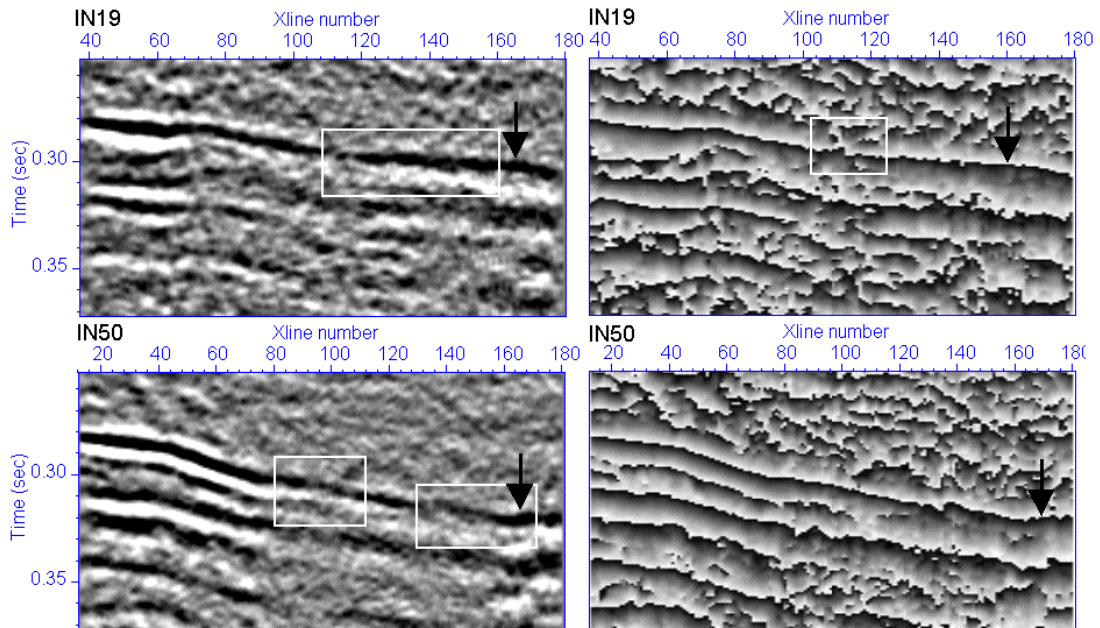


Figure 3.10 Since the instantaneous phase is independent of the amplitude strength, a horizon that appears with good signal-to-noise ratio looks clear and easy to follow, while the reflection strength on the same event is different from trace to trace. White rectangles are used to show the areas where most variation occurred between picking methods. The instantaneous phase picker will have less mis-picks due to its increased S/N ratio. Black arrows mark the same event on the two display styles.

3.2.5 3-D seismic survey in Newlands

Newlands Coal Mine carried out a 3-D seismic survey in early 1999 (Zhou and Hatherly, 1999). The processed 3-D data has 242 inline sections and 276 cross-line sections. The instantaneous phase picker was used to pick the reflections from the top of the Upper Newlands coal seam. In this example, the model sections were taken every 10 in-line sections. The whole picking process took about 17 minutes. The picked result in Figure 3.11 is displayed by using different displaying methods. The left-side plot shows the two-way reflection time contours of the Upper Newlands seam while the right is the shaded relief display of the reflection times (with the light source at 50 degrees east of south and 45 degrees above the horizon and a Z scale factor of 30). The shaded relief display emphasizes surface slope changes perpendicular to the light source rays, and shows up small faults clearly. This result is almost as good as the one picked carefully section by section.

Figure 3.12 shows some example sections picked by the instantaneous phase picker. These are inline sections run from south to north. The picked Upper Newlands seam reflections are marked in red. It is evident that the coal seam deepens from north to the south. The reflection quality in the south is better than in the north. This is also reflected in our picking result: the southern part is picked better than the northern part.

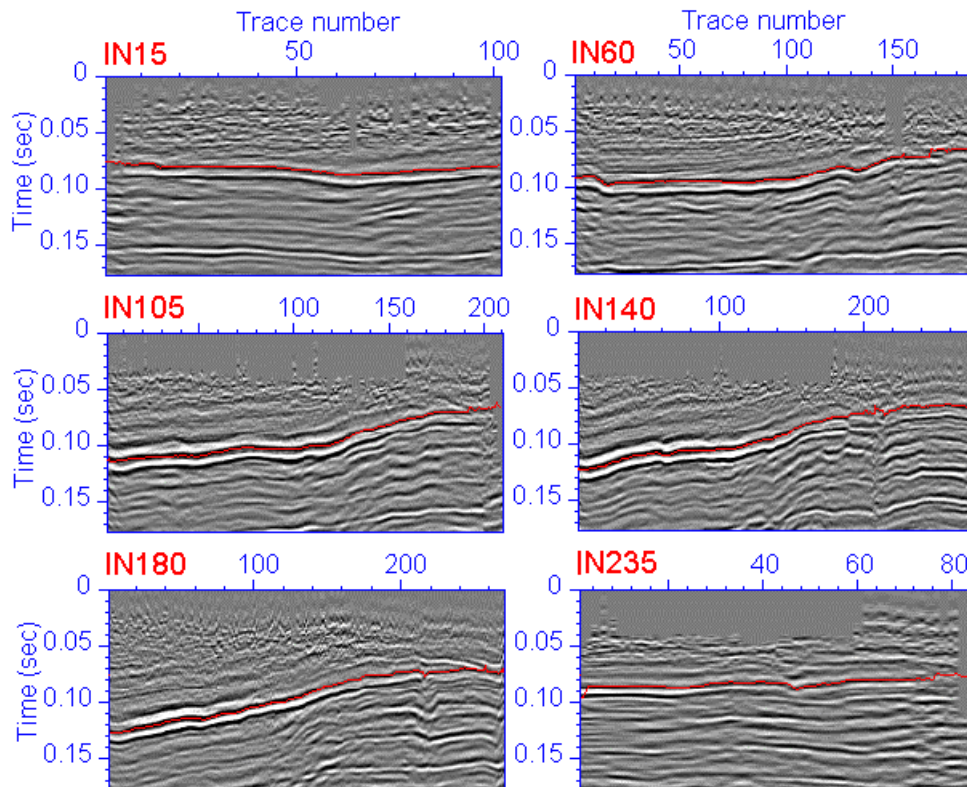


Figure 3.12 Sample sections show the picks (in red) by the instantaneous phase method for the Newlands 3D seismic survey. The label at each top left-hand corner of the image represents the corresponding inline number.

3.2.6 3-D seismic survey in Burton

A 3D seismic survey was commissioned by Burton Coal mine. The northern portion of the 3-D survey was acquired and processed by Velseis. The portion has 125 in-line and 105 cross-line sections. Faults can be seen when the data is scanned, thereby the selection of the guideline on 2-D model sections requires great care. The instantaneous phase picker was used in this application. About 15 in-line sections were selected to form a control grid. No further manual corrections were applied. Figure 3.13 shows the two-way reflection time contours of the targeted coal seam. Four major faults emerge. They trend from west to east. The picked examples from four in-line sections are displayed in

Figure 3.14. The faults were tracked correctly due to the careful initial guidance by the operator during the process.

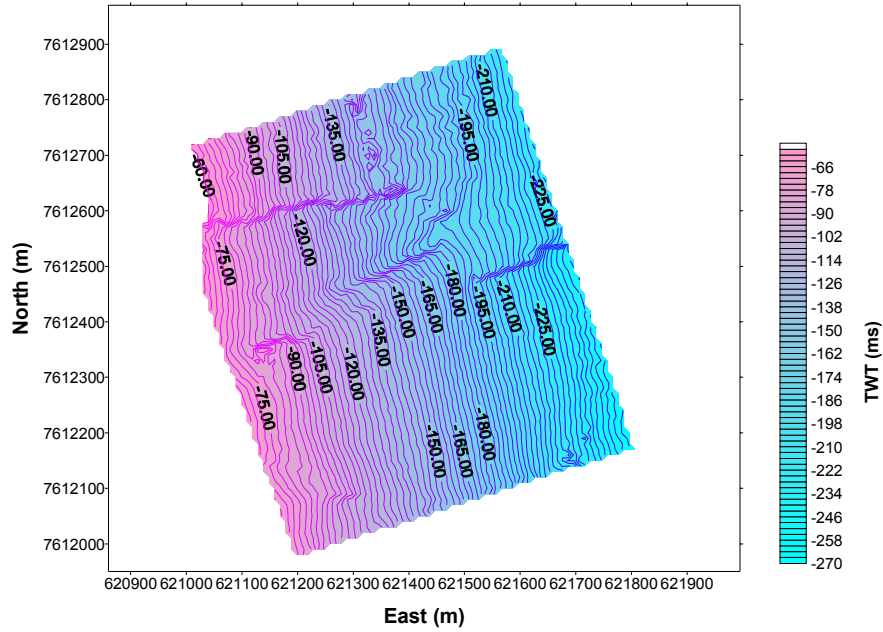


Figure 3.13 The two-way reflection time contours (left) of the Burton coal seam from a portion of 3D seismic survey at Burton Coal Mine.

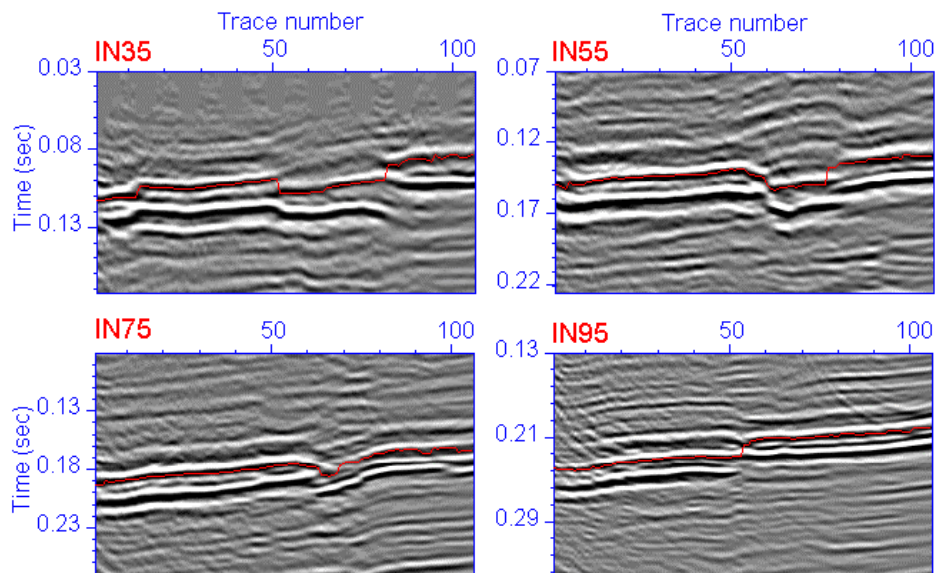


Figure 3.14 Four examples of picked sections (in red) from the 3D seismic survey at Burton Coal Mine.

3.3 CONCLUSIONS

The two 3-D horizon tracking methods, the correlation and the instantaneous phase method, were tested on 7 sets of 3-D seismic data surveyed over Australian coal mines. The methods enable the user to deal with various "poor data quality" situations interactively.

The selection of model sections depends upon a careful pre-examination of sections within and slices through the 3-D volume. The accuracy of the picks for each model section is of paramount importance. To ensure the accuracy of the picks on 2-D model sections, manual picking or correction may be required before the 3-D horizon tracking starts, especially when the SNR is poor. Tracing a target event (drawing a guide line) is easy and fast once the user has nominated the horizon. The better the control grid, the more successful the 3-D horizon tracking will be. Both of the correlation and phase picking methods can be used. Again, if the SNR is high enough to support it, and crossing events are few, the instantaneous phase method is easier and quicker to operate than a full blown correlation. Because it has built-in AGC, it has been found to give fewer mis-picks.

These methods do not guarantee robustness. Auto-picking must be interactive. The interpreter is responsible for the final checking and correction. *SeisWin's* architecture is such that it is easy to retrieve and manually correct mis-picks on either in-line or cross line sections.

CHAPTER 4 SEISMIC DISPLAY AND INTERPRETATION

4.1 INTRODUCTION

Digital image processing has been evolving continuously over the last 30 years since the early success in image processing made by NASA⁹ for lunar surface mapping (Baxes, 1994). As advances in computer hardware technology have allowed sophisticated digital image enhancement algorithms¹⁰ to be implemented at low cost, digital image processing has become increasingly popular and digital image processing techniques have found a wide range of applications.

Geophysicists study the earth by measuring its physical properties. Explosions, mechanical impacts or vibrations can generate seismic waves. These seismic waves are detected by instruments responding to the earth's motion. After their reflection, diffraction or refraction at interfaces between formations, various standard seismic processing techniques translate the recorded data into the final form ready for interpretation. The data display is vital as it is the primary point of information transfer. Owing to limitations of either visual perception or of the display medium, some weak but important features may not be seen even though the information is actually embedded in the data. Advances in digital image processing technology can enable us to improve the visibility of seismic information and extract details hitherto unseen. 3-D visualization techniques improve both the quality and efficiency of 3-D seismic interpretation (Dorn et al., 1995).

For years a number of image enhancing tools have been used either consciously or unconsciously by seismologists to improve the quality of the data display in seismic processing. The interpretation depends on the final display. Advanced digital image processing techniques give us powerful tools to break display limits, so we may reveal

⁹ stands for the National Aeronautics and Space Administration.

more subtle geological features. The final display is important but it seems to receive little attention from this large community. The objective of this chapter is to bring attention to the final display and to emphasize that this is also a vital procedure in seismic data processing, as poor image displays may keep useful information invisible. This chapter starts with a brief discussion on traditional seismic enhancing methods, then a number of tools used intensively in digital imaging enhancement are applied to seismic images. With advanced computer hardware and the interpreter's awareness and interaction, it is possible to find other ways to increase the visual perception of the final display. A number of examples are given.

4.2 BASICS OF SEISMIC DISPLAY

4.2.1 Seismic Display

Sheriff (1991) summarized a number of seismic display methods. Beside the wiggle trace display, there are variable area, variable-intensity, wiggle trace superimposed on variable area and color-coded wiggle trace displays. Figure 4.1 shows four display styles.

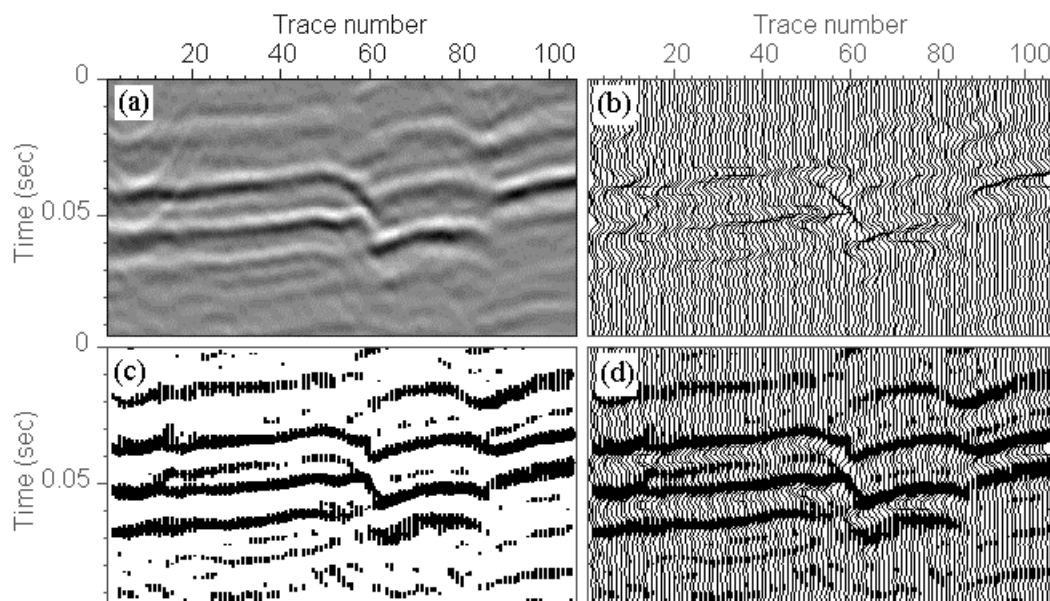


Figure 4.1 A few common used seismic display methods. (a) The image display; (b) The wiggle display; (c) The variable area display; (d) The superposition of the variable area and the wiggle trace.

¹⁰ Image enhancement is one fundamental class in digital image processing. It includes operations on improving an image's contrast and brightness, reducing its noise, raising small features above the detectable threshold and highlighting edges.

4.2.1.1 *Image display*

Signals usually are grouped into gathers, and presented as real, imaginary, envelope, instantaneous frequency & phase. Using the intensity of shades of gray to represent signal values creates a variable-density display (Sheriff, 1991). According to Feagin (1981) image displays, now popular, were hardly used before the eighties, because of limitations in computer hardware and the high costs of photographic copying.

With high-bit color resolution available in computer hardware and high resolution copying machines of low cost, the image display became popular and has some advantages over the convention display. Like the convention wiggle display, the image display also has dynamic range limitations. For example, with 256-color resolution (8-bit pixel) display, the range of the minimum and maximum value has to be re-scaled to the range 0-255. This means that a variable density display has a maximum possible dynamic range of 256 levels = $20\log_{10}(2^8)$ dB = 48 dB on a VGA computer monitor¹¹, the image display reveals smooth changes of waveforms.

4.2.1.2 *Wiggle display*

A map of the analogue line recorded by seismometers is called a wiggle display, known also as "wiggle lines", "squiggle" or "a conventional display" (Sheriff, 1991). Wiggle display has several styles, such as wiggles, variable area display, a combination of wiggle and variable area display and color-coded wiggle trace display. The variable area display shades the areas where amplitudes exceed a certain level and clarifies lateral coherence. Combinations of wiggle and variable area or color-coded wiggle trace are also used to make seismic events more easily perceived by the human eye. The drawback of wiggle display, pointed out by McQuillin et al. (1984) is that all final displays are severely restricted by the limited range between the smallest visible wiggle and the largest visible wiggle.

¹¹ On a monitor with 1024 horizontal pixels, the dynamic range for display of wiggle traces is $20\log_{10}\frac{1024}{N}$ dB, where N is the number of traces on the section. If $N=100$, the dynamic range is about 20 dB.

4.2.2 Instantaneous Seismic Attribute Display

Instantaneous seismic attributes include instantaneous amplitude (amplitude envelope), instantaneous phase and instantaneous frequency. They are used as aids in seismic interpretation. Discussions on instantaneous attributes can be found in Taner et al. (1979), Yilmaz (1987) and White (1991). Their definitions (Yilmaz, 1987) are listed in Table 4-1. Figure 4.2 displays three instantaneous attributes of a seismic section.

Table 4-1 Instantaneous attributes

Recorded seismic trace	$x(t)$
Hilbert transform	$x_H(t) = -\frac{1}{\pi} \int \frac{x(\tau)}{t-\tau} d\tau$
Analytical signal	$x_a(t) = x(t) + ix_H(t) = A(t)e^{i\theta}$
Instantaneous amplitude	$A(t) = \sqrt{x^2(t) + x_H^2(t)}$
Instantaneous phase	$\theta(t) = \arctan\left(\frac{x_H(t)}{x(t)}\right)$
Instantaneous frequency	$\omega(t) = d\theta(t) / dt$

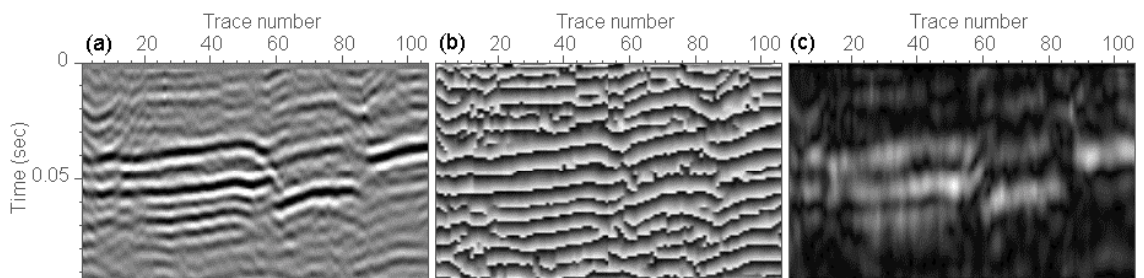


Figure 4.2 Three instantaneous attribute displays. Data courtesy of Burton Coal mine. (a) Real seismic section; (b) Instantaneous phase display of (a); (c) Instantaneous amplitude display of (a).

4.2.3 Zoom Function in Seismic Display

The zoom function is a frequently used tool to increase the data visibility or resolution. Figure 4.3 shows an example in which the zoom tool enables us to focus on a segment of the seismic signal.

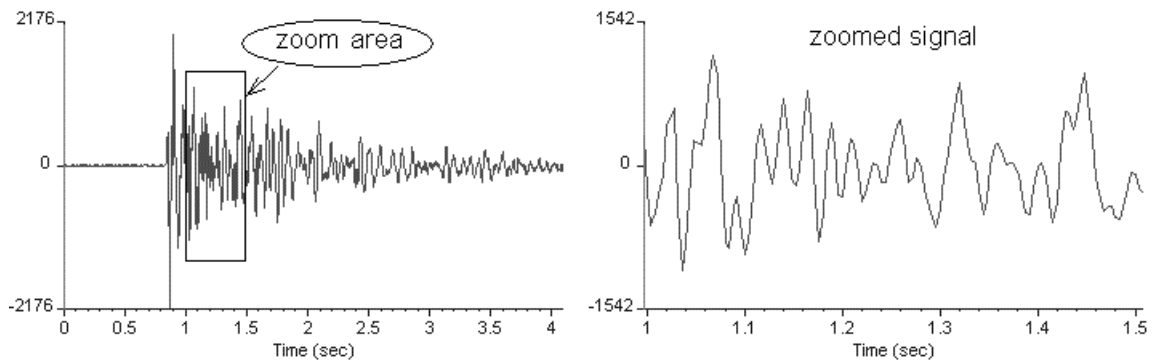


Figure 4.3 Zooming on a single seismogram.

A zoom area has to be carefully chosen to suit the purpose in hand. Improper horizontal and vertical scales may block subtle features. Figure 4.4(a) shows a vertical time section from a surface seismic line shot cross the Bulli seam at Appin Colliery Area 4. Only when the image is zoomed vertically, is the possible fault is revealed as shown by Figure 4.4(b). Figure 4.4(c) shows a zoomed version of Figure 4.4(b) in the horizontal direction. The fault seen on (b) is invisible because of the limited vertical scale.

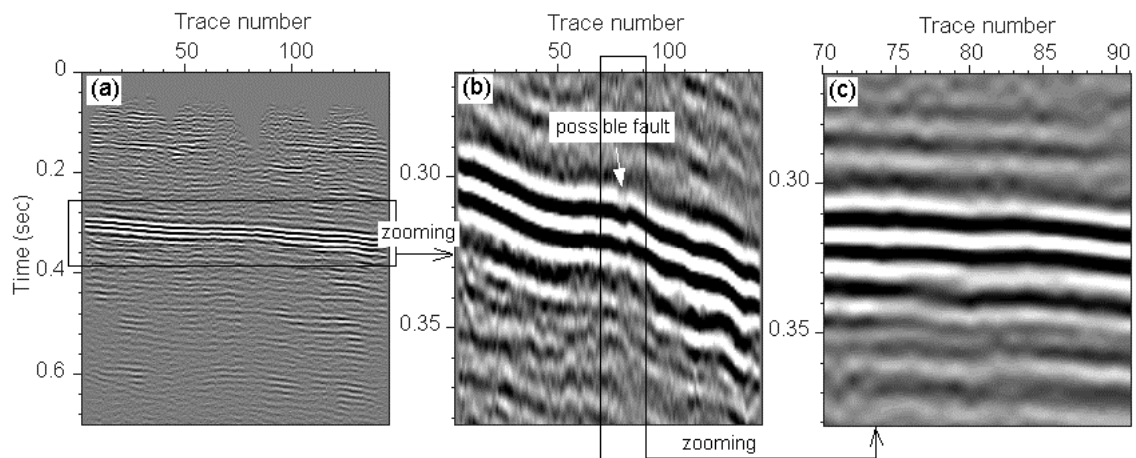


Figure 4.4 The zoom or re-scale is an important tool in seismic interpretation. By using different vertical and horizontal scale, some important feature may be revealed. (a) A vertical section from the Bulli seam; (b) The vertically enlarged version of the original image reveals a possible fault; (c) The horizontally enlarged version may conceal the possible fault.

A number of methods can be used to re-scale an image. One is to map the pixels in the source image to the approximated location in the destination image. This method is called *nearest neighbor interpolation* (Kabir, 1996). The quality of the destination image is not high. Another method is *bilinear interpolation*, described by Press et al (1992) as

being "*good enough for government work*," is a popular interpolation method. It is an extension of one-dimensional linear interpolation to two-dimensions. Others like *Bicubic interpolation* and *Polynomial interpolation* are among the popular methods for image mapping, but impose a computational burden which is usually not worth the outcome until central processors are improved. Bilinear interpolation is used in all of the images produced by *SeisWin* in this thesis.

4.2.4 Automatic Gain Control

AGC is a time-variant scaling operation. In seismology, the recorded amplitude is affected by a number of factors as waves travel through the earth. Instantaneous AGC is obtained from the RMS amplitude (*rms*) calculated from a time gate (window) on the input signal (Yalmaz, 1987). Figure 4.5 shows the process. The gain function is

$$g(i) = \frac{a}{\left(\frac{1}{2l+1} \sum_{k=i-l}^{i+l} x_k^2 \right)^{1/2}},$$

where a is an arbitrary number, l is a half of the gate length, x_k are the amplitudes of the samples in the gate. As the window steps down the trace, the gain function is computed¹². In computation the window length must be defined by the user. The effectiveness of the gain function depends on the window length. Figure 4.6 gives an example of AGC by using different window lengths. The dominant frequency of the image is 50Hz, i.e. the period is 20 milliseconds (ms). In this example, all images are improved after applying AGC, and the shorter window length does a better job than the longer window. However, the window length can not be arbitrary short. The amplitudes of the image will be saturated and the image details will gradually disappear when the window length is shortened below a half a period. For preserving the signal character, a window length of twice or three times the dominant period seems the best choice. The signal character is preserved with significant improvement on later arrivals. This can be seen from Figure 4.7, for a single trace taken from the images in Figure 4.6. However, AGC also boosts noise and a compromise has to be made.

¹²In the half length gate at each end of the signal, the nearest edge point is assigned the rms value of the first half gate. Then the gate expands down (or up if it is at the end) one sample, the new rms in the gate is assigned to the second nearest point from the edge, and so on till the full length gate is reached.

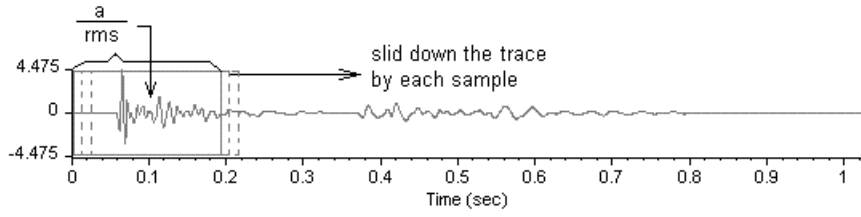


Figure 4.5 The gain function is calculated for each time gate.

Yilmaz (1987) describes another AGC similar to the one just mentioned (see "RMS Amplitude AGC", Yilmaz, 1987). The only difference is that the time gate steps to the centers of pre-partitioned time gates on the input trace, then the gain function is interpolated between each gate centers.

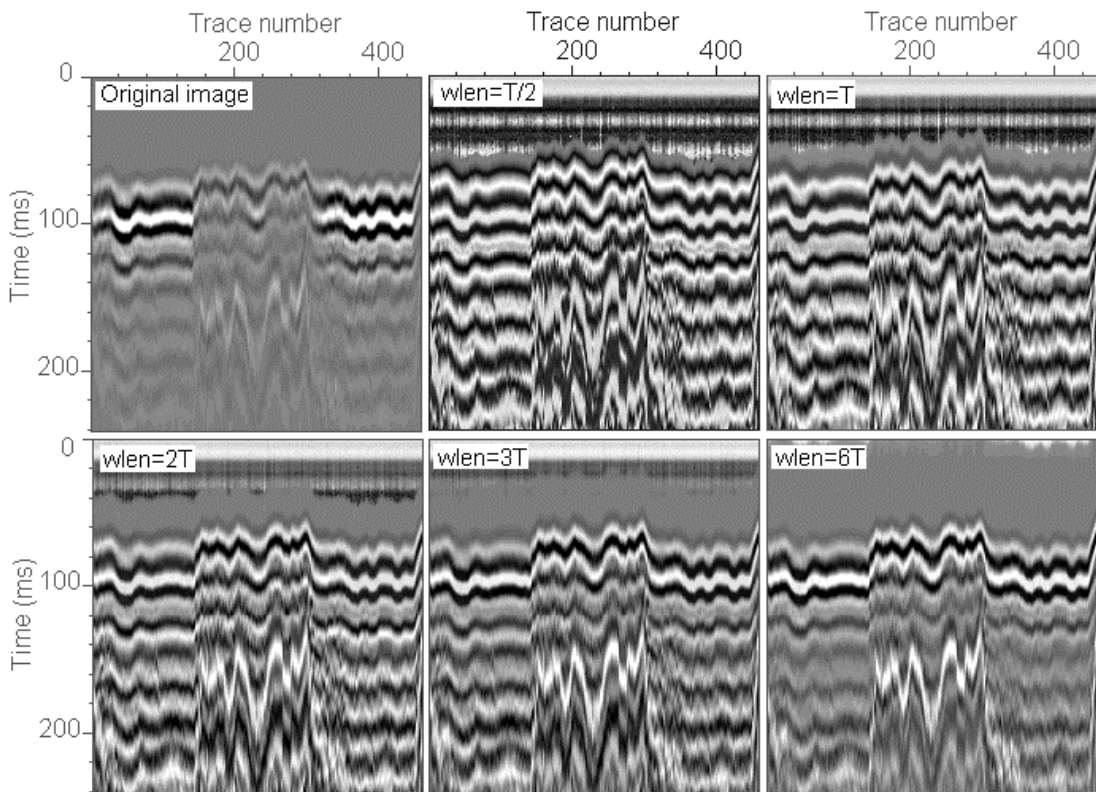


Figure 4.6 The results of automatic gain control. T ($=20$ ms) is the dominant period.

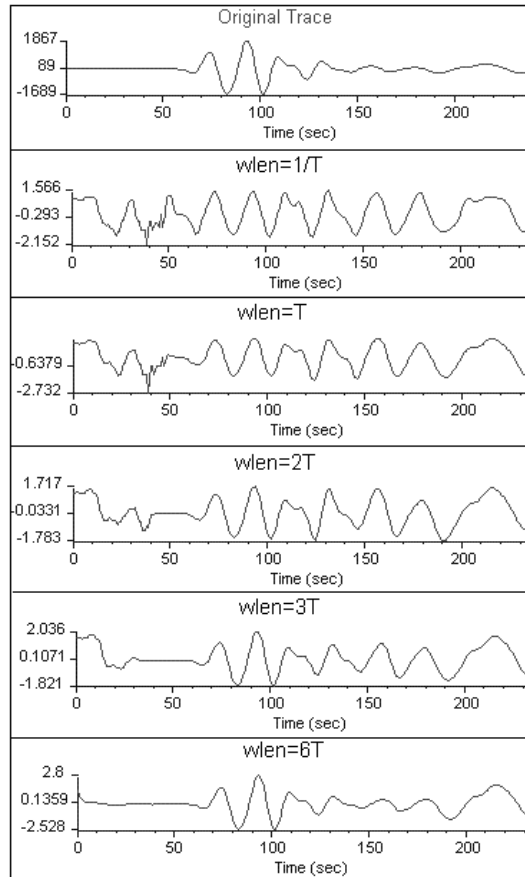


Figure 4.7 The signal shape after applying AGC. The window length is denoted by "wlen". T is the dominant period.

4.2.5 Clipping & Comanding

Data are normally presented with full dynamic range, i.e. from the minimum to the maximum values. Sometimes, the intermediate values may not be shown up on the section due to a skewed distribution of the data or the presence of wild values. In these cases the end values of the data need to be sacrificed to reveal the intermediate values, i.e. to compress or clip the dynamic range of the image. For example, an image array is sorted in ascending order. By setting a 2% clipping percentile, 2% of the total number of elements at each end of the sorted array will be clipped. Figure 4.8 is a diagram of the clipping concept. The modified range is re-scaled to fit the gray levels. Figure 4.9 shows the effectiveness of clipping. After applying 5% clipping on the original image, the contrast of the image Figure 4.9(a) was improved. When clipping values are too large, the details of the image drop out (see Figure 4.9(c) and (d)). Clipping is a simple and an effective way to improve an image's contrast, but severe clipping should be avoided.

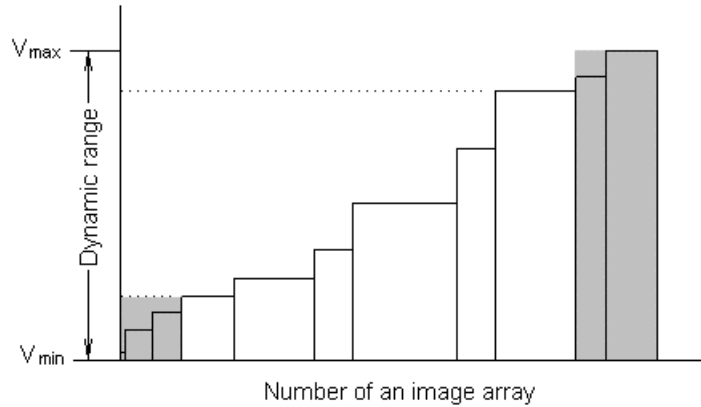


Figure 4.8 Value clipping. Dynamic range can be decreased by clipping some percentile of elements (shaded area) from two ends of the sorted array.

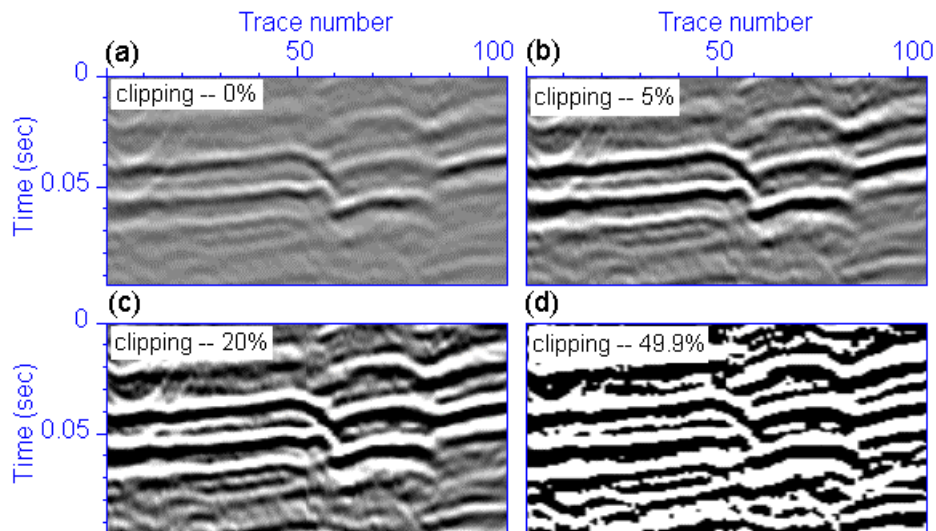


Figure 4.9 Different Clipping factors applied to an image.

4.3 IMAGE ENHANCEMENT AND SEISMIC DISPLAY

In this section, a number of imaging enhancing tools are applied to seismic data. These tools are not new in digital image processing, but some have not found wide applications in geophysics.

4.3.1 Using Filters

One popular method used to improve the appearance of an image is to perform a two-dimensional convolution between a spatial filter and the source image. The filter may be square, rectangular, circle, cross-shaped.

4.3.1.1 Median filters

Median filters are effective in spiky noise reduction. They are non-linear. When a median filter moves over an image, all the values in the filter are sorted in ascending order. The central pixel in the filter is replaced with the value in the middle of a sorted array. The median filter has two main advantages: removing impulse noise and maintaining edge features. However, median filters do have averaging effect even though they preserve edges. 2-D median filters may have various shapes.

Figure 4.10 shows three median filters. The rectangle-shaped window may wipe out thin lines and round up corners, while the cross-shaped and plus-shaped windows are better for preserving such features.

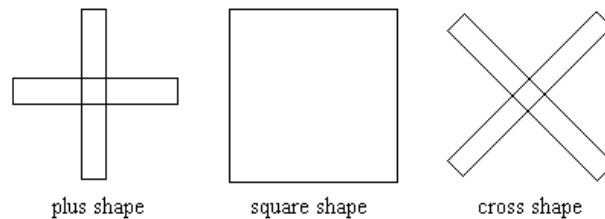


Figure 4.10 Median filters with different shapes.

One application of median filters is shown in Figure 4.11. The first break picks on a portion of full waveform sonic data, which is collected at Callide coal mine, is not smooth, as there are noise spikes in the data. I re-picked the first breaks after applying a 5-point median filter to each trace and the picks are obviously improved.

4.3.1.2 High-pass filtering

Small features are important in seismic interpretation. For various reasons, recorded seismic data lose high frequencies. High-pass filters such as those listed below can be used to restore fine details (see examples in Gonzalez and Woods (1993) and Kabir (1996)):

$$M1 = \begin{bmatrix} -1 & -1 & -1 \\ -1 & 9 & -1 \\ -1 & -1 & -1 \end{bmatrix} \quad M2 = \begin{bmatrix} 1 & -2 & 1 \\ -2 & 5 & -2 \\ 1 & -2 & 1 \end{bmatrix} \quad M3 = \begin{bmatrix} -1 & -1 & -1 \\ -1 & 8 & -1 \\ -1 & -1 & -1 \end{bmatrix}$$

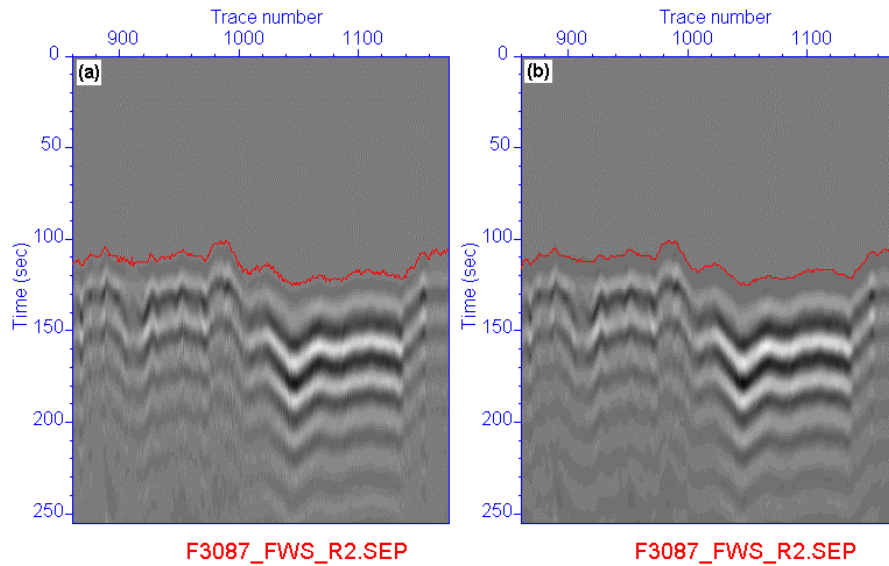


Figure 4.11 (a) The first breaks picked (the red curve) by amplitude threshold detection; (b) The first breaks are picked again after applying the median filter to the raw data.

These sharpening masks can reduce the intensity contrast in slowly varying areas of the original image, and emphasize edges. A high-pass filtered image can also be obtained from a low-pass filter by,

$$High_pass = Source - Lowpass \quad (2.15)$$

Figure 4.12 shows the mask M3 applied on a portion of full waveform sonic data collected in a vertical water-filled hole drilled through sediments at Callide coal mine. There are some weak longitudinal waves running almost vertically which can be seen on the original image. These waves become much more evident after high pass filtering. The gray scale of the resultant image is reversed to enhance visibility.

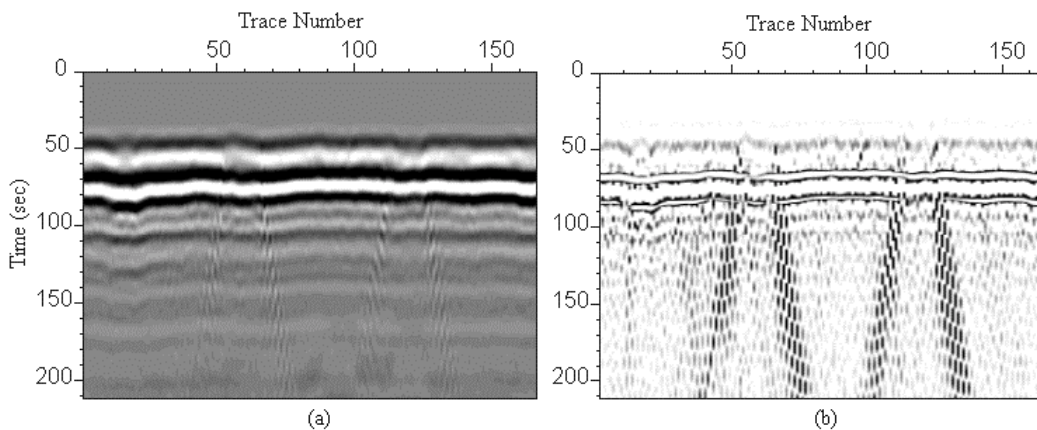


Figure 4.12 (a) Original image from part of full waveform sonic collected from Callide coal mine; (b) The result of high pass-filtering using M3 (displayed in the negative form of the actual image).

Figure 4.13 shows the mask M1 applying on a vertical section from the Burton 3-D survey (Inline 66). The filtered image obviously shows more details than the original.

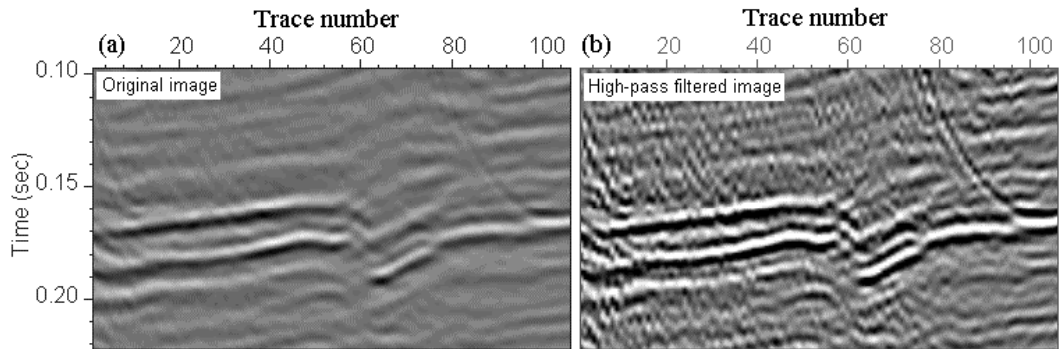


Figure 4.13 Using sharpening filter M1 to highlight details.

4.3.2 Edge Detection

Edges are important features of images. The edge of an image is characterized by distinct gray level between two regions. Edge detection raises similar problems to the first break and other arrival time detection issues that formed the subject of Chapters 2 and 3. The Sobel edge detector is used to find the image gradient in the horizontal (H) and vertical (V) directions. The mask is generated as (Kabir, 1996):

$$H = \begin{bmatrix} -1 & -2 & -1 \\ 0 & 0 & 0 \\ 1 & 2 & 1 \end{bmatrix} \quad V = \begin{bmatrix} -1 & 0 & 1 \\ -2 & 0 & 2 \\ -1 & 0 & 1 \end{bmatrix}$$

Figure 4.14 shows an edge detection result from a portion of in-line section from a 3-D survey. The original image is firstly convolved with the Sobel edge detector – the vertical operator, the result is then summed with the original image with an amplification factor $A=1.2^{13}$. The result reveals some discontinuities which could not be seen in the original image (as the white arrows indicate).

¹³ referred as high-boost filtering operation $High_boost = (A-1)(Source) + High_pass$ (Gonzalez and Woods, 1993).

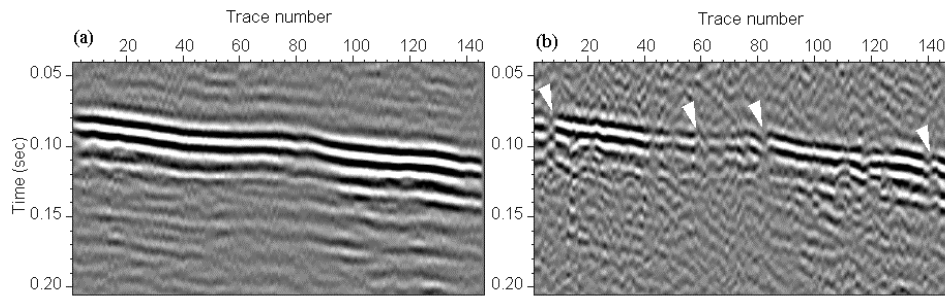


Figure 4.14 Edge detection. This portion of image is an inline section (#41) of the 3D data from BHP Appin Colliery. (a) The original image with 3% clipping; (b) The result yielded by the Sobel edge detection – vertical operator with high boost filtering. The white arrows mark possible geological discontinuities which can not be seen in the original image.

4.3.2.1 Laplacian operator

The Laplacian operator is the second derivative of a function $f(x, y)$

$$\nabla^2 f = \frac{\nabla^2 f}{\nabla x^2} + \frac{\nabla^2 f}{\nabla y^2}. \quad (2.16)$$

It approximates the magnitude of the second derivative at any point. An example of the mask is

$$M_L = \begin{bmatrix} 0 & -1 & 0 \\ -1 & 4 & -1 \\ 0 & -1 & 0 \end{bmatrix}$$

Figure 4.15(a) shows a subsurface¹⁴ two-way travel time image of the target coal seam derived from a portion of the 3D seismic survey at Burton coal mine. This image looks featureless due to the relative large dip of the coal seam to the northeast. However, the faulting structures are enhanced by applying the edge detection filters as shown by Figure 4.15(b) and Figure 4.15(c).

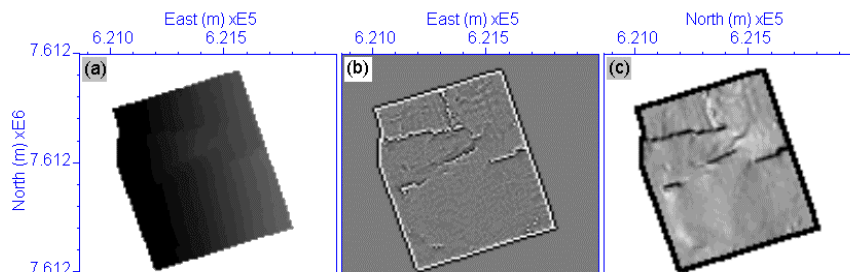


Figure 4.15(a) The original image; (b) After applying a Laplacian operator on (a); (c) after applying a Sobel operator on (a).

¹⁴ The subsurface image is produced by Surfer.

4.3.3 Histogram Processing

The range of image intensities refers to an image's dynamic range. When an image's dynamic range is much larger than the capacity of the display device, the image's contrast is low. Decreasing the dynamic range of an image is intuitive way to improve an image's contrast. On other hand, the dynamic range may be smaller than the capacity of the display device, modification of an image's contrast is necessary. A few ways to modify an image's contrast are discussed in this section.

4.3.3.1 Histogram stretching

The histogram of an image tells us the frequency distribution of pixel values in the image. It can be expressed as,

$$p(r_i) = n_i / n, \quad (2.17)$$

where r_i is the i th gray level and $i = 0, 1, 2, \dots, L-1$ is gray level range (e.g., an image with 8-bits pixels has gray level range 0-255), n_i is number of pixels in i th level and n is total pixel numbers in the image. It is not hard to see that Equation (2.17) describes the probability of occurrence of gray-level r_i .

The distribution of an image's pixel values can give an appropriate clipping guide. Figure 4.16¹⁵ is an example. The histogram of the original image in Figure 4.16(a) shows that most of the image values are concentrated between -20 and 20 . Therefore, we may redistribute the pixel values by excluding all the values beyond this range. Figure 4.16(b) shows the modified image and its histogram. This operation shows how to chop off insignificant gray levels safely.

¹⁵ The horizontal axis was converted into pixel values of the data rather than the gray level range (0-255).

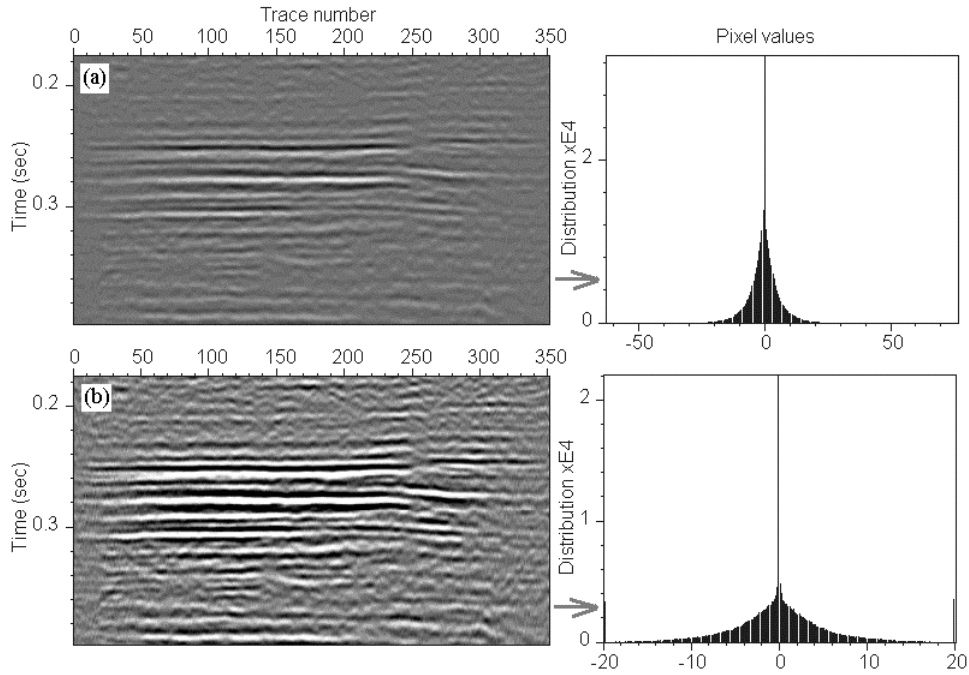


Figure 4.16 Clipping guided by the histogram. (a) The original image and its histogram (right side of (a)); (b) The clipped image guided by the original histogram and the new histogram.

4.3.3.2 Histogram equalization

The goal of histogram equalization is to create a desired image with a quasi-uniform distribution of pixel values. Therefore a transformation function has to be found. It is useful to consider the derivation of a transformation (Gonzalez and Woods (1992)). Let $P_r(r)$ be the probability density function of the source gray level r and $p_s(s)$ represents the probability density function of the desired gray level s , the transformation function should be written as $d = T[r]$. The relationship between two image gray levels and the transformation function is illustrated in Figure 4.17. According to elementary probability theory, the probability density function of the transformed gray levels is,

$$p_s(s) = \left[p_r(r) \frac{ds}{dr} \right]_{r=T^{-1}(s)} \quad (2.18)$$

Please note that the transformation function has initial assumptions that the pixel values are continuous quantities that have been normalized in the interval $[0,1]$, with $r = 0$ representing black and $r = 1$ representing white, and it must be single-valued and monotonically increasing in $[0,1]$. Suppose the transformation function is,

$$s = T(r) = \int_0^r P_r(w)dw \quad (2.19)$$

and the derivative of s respect to r is,

$$\frac{ds}{dr} = p_r(r). \quad (2.20)$$

From Equation (2.19) and (2.20), we have

$$p_s(s) = 1 \quad (2.21)$$

Equation (2.21) gives an important result: a transformation function which equals the cumulative distribution of an image's pixel value produces an image with a uniform density. The transformation in its discrete form can be written as,

$$T[i] = \sum_{n=0}^{i-1} h(n), \quad i = 0, \dots, N-1 \quad (2.22)$$

where $h(n)$ is the histogram of the original image. It is equivalent to the cumulative distribution of an image's pixel value producing an image with a uniform density. Figure 4.18 gives an example of histogram processing. The data is the same as in Figure 4.16. We can see that histogram equalization has considerable effect on the appearance of an image. The advantage of histogram equalization is that the gray levels of an image are spread out and extend across the amplitude range from black to white.

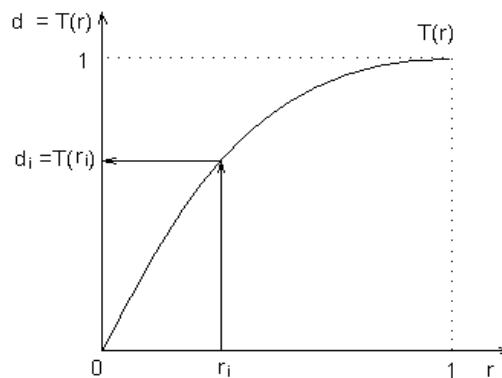


Figure 4.17 A gray-level transformation function. The horizontal axis presents the gray levels of the source image, the vertical axis presents the gray levels of the destination image. The transformation procedure can be considered as a mapping procedure as the arrows indicate.

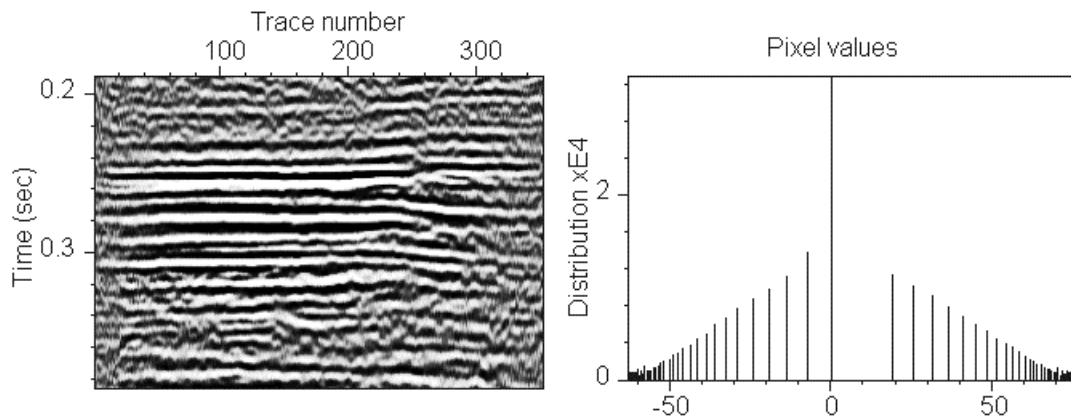


Figure 4.18 Histogram equalization processing. (a) The corresponding improvement to the original image which was shown in Figure 4.16(a). (b) The histogram corresponding to (a).

Histogram equalization enhances an image in a global sense. It is generally good, but is sensitive to noise. To remedy the problem, adaptive histogram equalization was introduced (Kabir, 1996). The idea is to get the transformation function needed for histogram equalization from a window area and assign the result to the central pixel of the window. The method is computationally expensive. This method is also a special case of histogram specification where any specified transformation functions may be applied with a window.

4.3.3.3 Histogram specification

A general form of histogram equalization is called histogram specification. In general the gray levels of an image can have any desired density rather than uniform density. Alternatively, the image's quality can be controlled by changing the shape of the transformation function directly. Figure 4.19 shows three images produced from CorelDRAW7 to illustrate the effectiveness of toning the transformation function. Their corresponding transformation functions are displayed below. When the transformation function is a diagonal line across the grid, the image's distribution remains unchanged. Otherwise, the appearance of the image will be different as the transformation function changes. This is a good way to choose the best image according to the user's visual desire and the user is in full control of it.

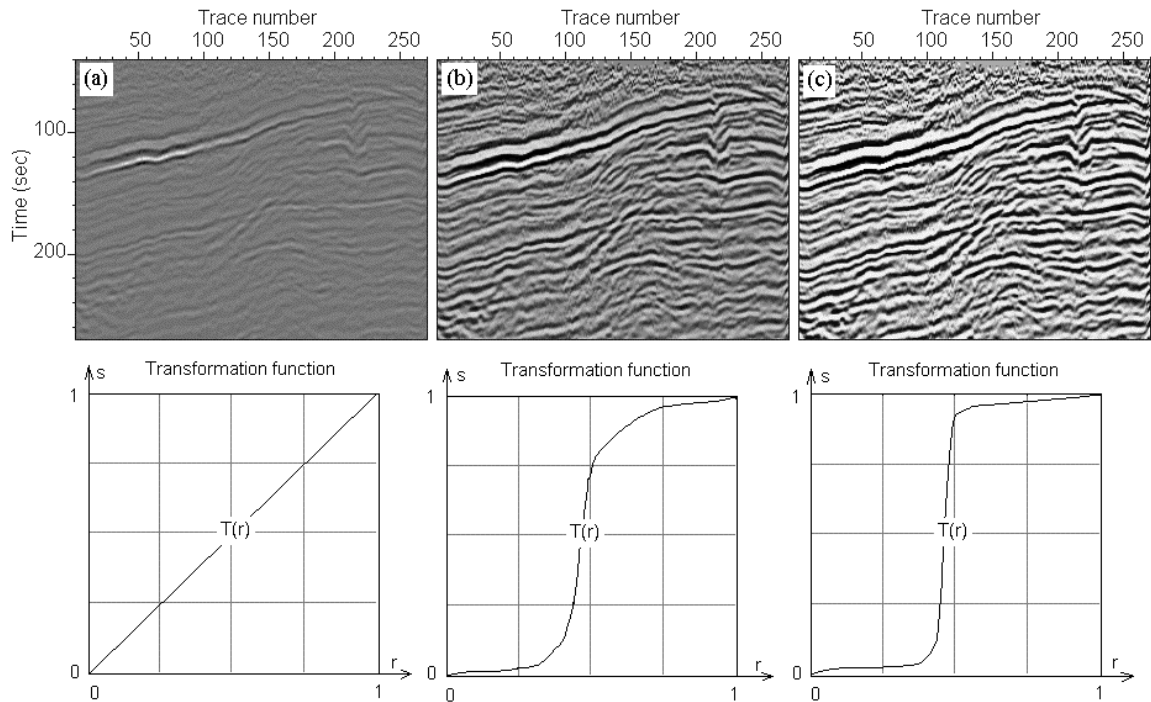


Figure 4.19 Histogram specification method. The transformation function for each image is placed right beneath it. (a) The transformation is a linear function and the original image is unchanged; (b), (c) The new images produced by the transformation function. The pictures were produced by using CorelDRAW7.

4.3.4 Local Enhancement

Another gain method used in digital image processing is called local enhancement (Gonzalez and Woods, 1993). The method uses a local mean and variance to measure the appearance of an image and calculates a gain value for it, as the intensity mean and the variance are considered to be measures of average brightness and contrast respectively. Local enhancement is applied to a neighborhood of pixels, and usually a rectangle-shaped or square-shaped area. The local gain can be obtained by applying the following formula at each pixel location (x, y) of an image:

$$g(x, y) = A(x, y)[f(x, y) - m(x, y)] + m(x, y)$$

Original image \swarrow
 $f(x, y)$
 Local mean \swarrow
 $m(x, y)$
 \searrow
 New image \swarrow
 $g(x, y)$

$$A(x, y) = k \frac{M}{\sigma(x, y)} \quad 0 < k < 1$$

Global mean \swarrow
 M
 Standard deviation \swarrow
 $\sigma(x, y)$
 Constant value \swarrow
 k

An application of local enhancement is shown in Figure 4.20. In this example, the local neighborhoods with 3x3 and 11x11 pixels were used. It is obvious that the display is brought up more evenly for the data as shown by the corresponding histograms beneath the sections. Local enhancement is very sensitive to noise when the mask size is small. The example in Figure 4.20 may not be the most appropriate one to show the effectiveness of the method, as the method is desired for balancing large excursions of intensity in isolated regions (Gonzalez and Woods, 1993).

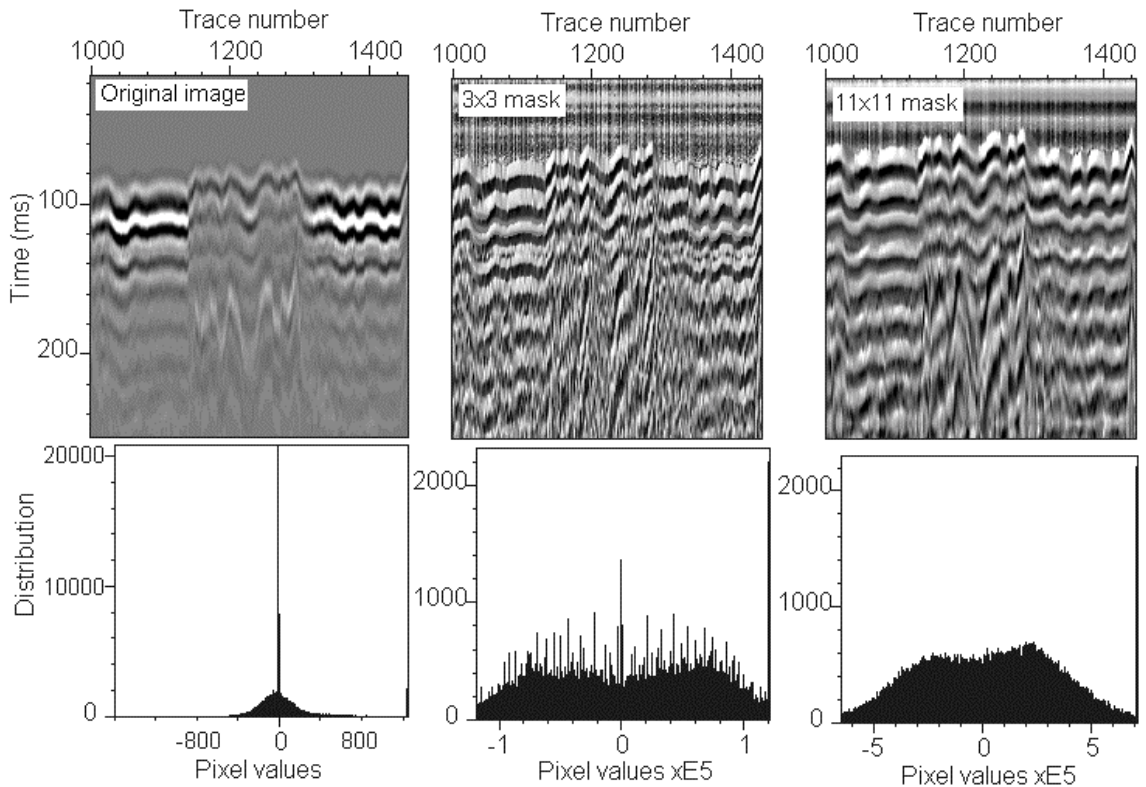


Figure 4.20 The local enhancement operation has made the original image more informative. Two different mask sizes are used for illustration. The histogram of each image was placed right underneath its image.

4.3.5 Gray Scale and Color Display

In the standard colormap, different color palette entries give different set of colors in the image. By changing the palette entry, we can change the contrast in an image. Figure 4.21 shows a few images represented with different palettes. The data are vertical sections from a 3-D survey at Burton Coal Mine. There are two strong events with faults at about trace number #63 and trace number #86. The plots (b), (c) and (d) convey more

information than the original plot (a). An appropriate palette entry can improve an image's contrast without changing the dynamic range of the data.

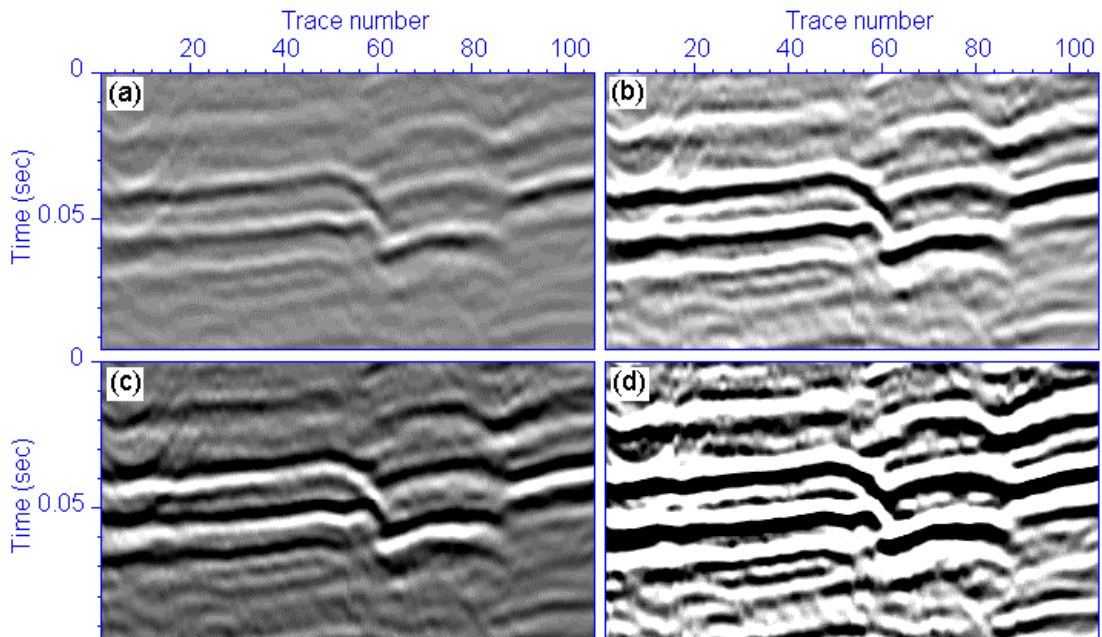


Figure 4.21 (a) is an original image. (b), (c) and (d) are the original image displayed with different entries of gray scale. The image contrast can be improve by choosing appropriate palette entry.

Colors may be more effective at emphasizing different seismic features. Figure 4.22 shows the comparison between a tricolor display and the gray scale display. Two different colormap displays are shown in Figure 4.23. The identification of a reflector is difficult on the gray scale display because of faults. Color eases identification because each color is associated with unique amplitude.

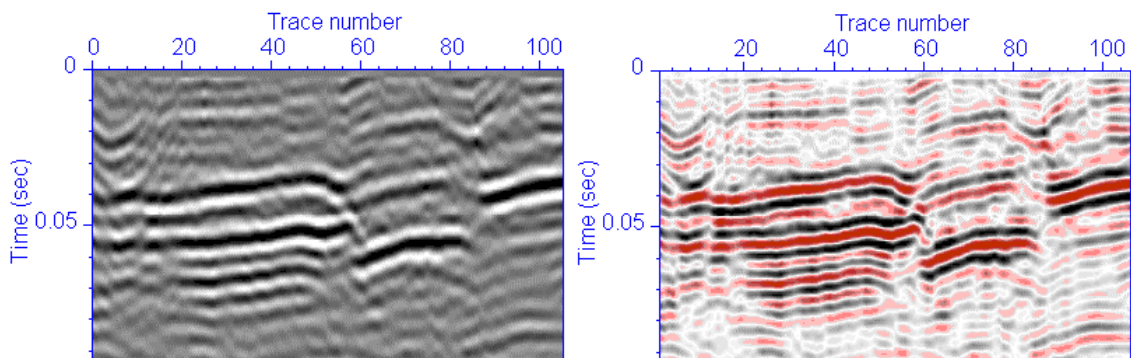


Figure 4.22 Tricolor and grayscale displays.

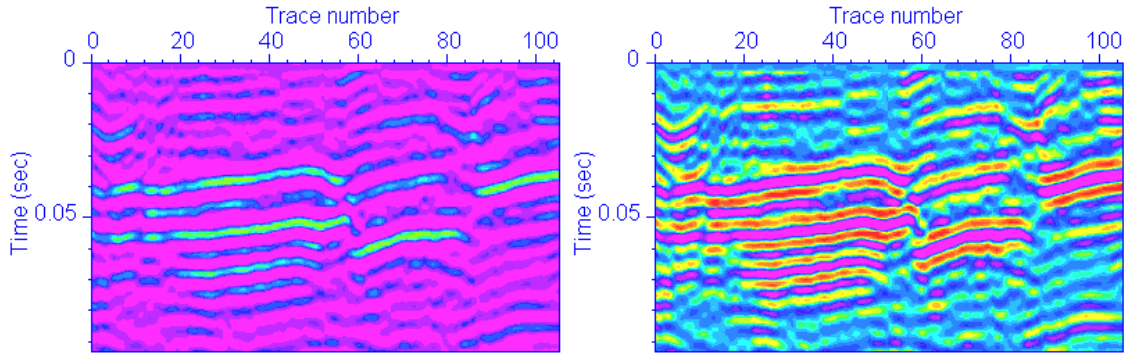


Figure 4.23 Colormap display.

4.3.6 Shaded Relief

Shaded relief can be thought of as an object illuminated by a point light source. If we display seismic data as Lambertian¹⁶ surfaces, then the brightness of each picture element on the surface depends on the angle between the direction to the point light source and the surface normal. If we let P_0 and Q_0 be east-west and north-south components of the vector pointing to the point light source, P and Q be the east-west and north-south components of the surface slope, θ be the elevation angle of the light above the horizon, and ϕ be the azimuth of the light source, the illumination of an object can be calculated according to Kowalik and Glenn (1987)

$$output = \frac{(1 + P_0P + Q_0Q)}{(1 + P^2 + Q^2)^{1/2}(1 + P_0^2 + Q_0^2)^{1/2}}$$

where

$$P_0 = -\tan(90 - \theta) \cos(\phi),$$

$$Q_0 = -\tan(90 - \theta) \sin(\phi),$$

and the slope parameters were calculated within a 3×3 window by

$$P = \frac{X(K+1) + 2Y(K+1) + Z(K+1) - X(K-1) - 2Y(K-1) - Z(K-1)}{m},$$

$$Q = \frac{X(K-1) + 2X(K) + X(K+1) - Z(K-1) - 2Z(K) - Z(K+1)}{m},$$

where $X(K)$, $Y(K)$ and $Z(K)$ are the input value within the window for row 1, 2 and 3; K is the K th column within the window and m is a scalar factor of the surface slope.

Shaded relief display uses different shades to indicate the surface slope and its direction relative to the light source direction. Shaded relief has been used for years in 3-D interpretation by seismologists (Rijks and Jauffred, 1991). It is a useful tool for revealing structure features, e.g. trends, subtle faults. The direction of a light source is critical in revealing features. Various illumination directions need to be investigated.

To show this, we used the shaded relief function of Surfer. Seismic data were reformatted into the Surfer grid format by using *SeisWin*. Figure 4.24 shows the shaded relief display of a seismic section from Newlands Coal mine. Figure 4.24(b), (c) and (d) show three images with different light positions. When the light source is placed at different positions, the appearance of the image changes and conveys different information. This is a fact that can help interpretation.

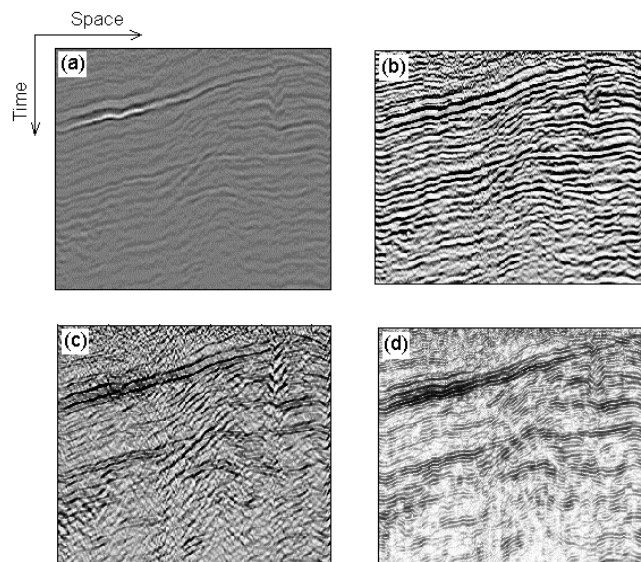


Figure 4.24 Shaded relief display. (a) The original image; (b) The light was from the north and the height of light was 45 degrees from the horizon; (c) The light was from the east and the height of the light was 45 degrees from the horizon; (d) The light was from the exact top of the image.

Another example also uses 3D seismic survey data from Newlands Mine. The two-way reflection times from the top of the Upper Newlands seam were picked using *SeisWin* (see chapter 3). Figure 4.25 shows the shaded relief image (using Surfer) with three

¹⁶ For those objects with dull and matte surfaces which exhibit diffuse reflection (Foley et al., 1991).

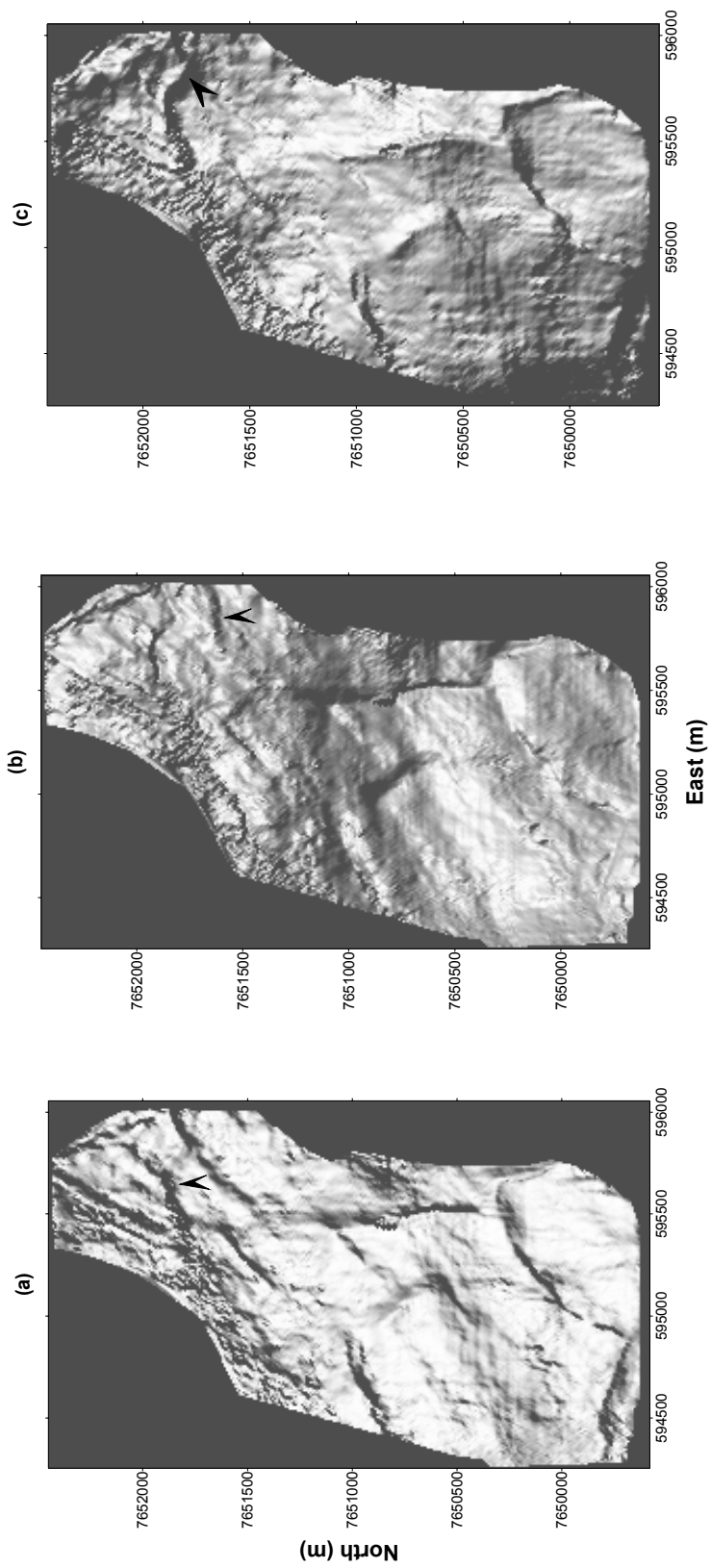


Figure 4.25 Shaded relief display of the Upper Newlands seam. (a) The light source is at 55 degrees from the east and 30 degrees from the horizon; (b) The light source is at 60 degrees from the east and 40 degrees from the horizon; (c) The light source is at 320 degrees from the east and 30 degrees from the horizon. Images are presented using Surfer. The black arrow in (a) indicates a trend extended toward top-right corner, while (c) reveals that this trend is also connected with another trend marked by the black arrow. The trend indicated by the black arrow in (b) can not be seen on the other two images.

¹⁷ in an anti-clockwise direction

different illumination directions. The black arrow in Figure 4.25(a) indicates a trend extended toward top-right corner, while Figure 4.25(c) reveals that this trend is also connected with another trend marked by the black arrow. The trend indicated by the black arrow in Figure 4.25(b) can not be seen on the other two images.

4.4 DISCUSSIONS AND CONCLUSIONS

Numerous tools for improving the quality of an image can be applied to seismic images to ease interpretation. Seismic images can be displayed in different colors and scales or styles. They can also be modified by image enhancement tools. Events on enhanced images may be easier to identify either manually or automatically (as in automating horizon picking).

In interactive data processing it is essential to be able to highlight important features of the data. Various filters are easy to implement and are efficient. Edge detectors help to detect faults and structural trends. Data can be improved significantly using image processing tools. However, care must be taken in using these tools. Interpreters must be aware that relative amplitudes usually change after image enhancement. It is obvious that care is needed to avoid the corruption of amplitude-variation-with-offset data fields or straight forward seismic sections.

Image recognition and interpretation is an important area in digital image processing. Machines can automatically extract patterns / textures from a background of irregular details and generalize this knowledge to recognize similar patterns in new circumstances. It is a promising study area and some techniques have already been used in seismic event detection. Display enhancement is an important aspect of this work. More studies on geophysical time sections are necessary.

3-D visualization techniques, such as volume rendering and animation sequences of reflection events, give a broad view of the data, and improve understanding of the structures and the surrounding environments before interpretations. Kidd (1999) and

Dorn et al. (1995) give good discussions on 3-D visualization techniques in seismic interpretation. Shaded relief can be vitally important because it can highlight features.

CHAPTER 5 NON-UNIFORM SPARSE DATA AND IMAGING

5.1 INTRODUCTION

It is ideal for geophysical data acquisition to achieve dense coverage and the uniform illumination of targets. However, these ideals cannot be approached in many practical instances. In mining geophysics in particular, acquisition arrays are often sparse and non-linear. Boreholes and mine drives are often twisted. Targets subtend almost any angle to the access drives. Uniform illumination of the subsurface is rare. Data sets are limited – even to the extent of attracting the need for isolated trace correlation. In summary, mining geophysicists have no option but to work from the known – or at least geologically plausible – with sparse data sets.

Seismic reflector imaging has been studied intensively. Numerous approaches, like conventional migration stack technology (e.g., Rockwell, 1985; Zhe and Greenhalgh, 1999), ray tracing based methods (e.g., Chang and MaMechan, 1986) and wave equation techniques (e.g., Claerbout, 1971; French, 1975; Stolt, 1978; Loewenthal and Hu, 1991) have been used for mapping seismic reflectors. However, most methods used for seismic reflector mapping were designed for well sampled seismic arrays rather than sparse data sets.

In this chapter, we start from very basic and simple geometric considerations and their relationship with standard patterns of seismic reflection. These fundamentals help us to work towards more complex situations in the later sections of the chapter. For imaging reflector purposes, a few 2D modeling methods are discussed. Those methods have close relationships with the important issue of the chapter – the dependence of sparse array seismic reflection mapping methods on the a priori assumption of the nature of a target. The concepts developed in this chapter apply both to seismic and to geo-radar data. Two methods involving sparse data mapping are event migration and common tangent line stacking. Both were developed especially for sparse data sets and used for mapping

reflectors. Both will be illustrated using numerical examples and real data sets from borehole radar surveys .

5.2 BASIC PATTERN OF REFLECTIONS

By studying simple interface models, we can obtain standard patterns of reflection or diffraction response from the subsurface. Good understanding of the fundamentals can aid the later study of more complex geophysical patterns.

5.2.1 Reflection Models

5.2.1.1 Horizontal Reflector

5.2.1.1.1 A single horizontal layer

The simplest model is a horizontal homogeneous reflector. If a number of geophones are placed on both sides of a source along a line (a split-spread arrangement) on the surface, the time-distance curve of the reflection can be shown in Figure 5.1. The shortest traveltime (t_{min}) along the hyperbola is at zero-offset position. This is also referred to as the normal incidence traveltime¹⁸. For a horizontal interface, the normal incidence reflection time is identical at any point on the surface.

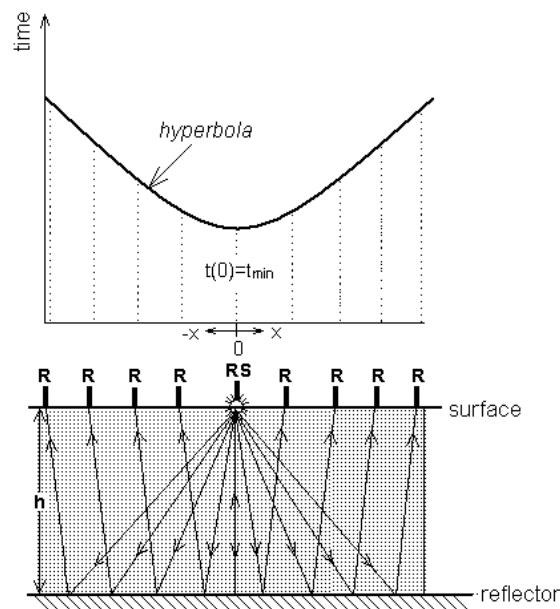


Figure 5.1 Diagram illustrating the reflection raypath and its traveltime curve for a horizontal reflector– a hyperbola of time-distance relationship.

¹⁸ the time which a ray travels perpendicular to the subsurface and back along the same raypath.

According to the law of reflection, the travelttime equation is derived based on Pythagoras' theorem

$$\begin{aligned} t^2(x) &= \left(\frac{2h}{v}\right)^2 + x^2 / v^2 \\ &= t^2(0) + x^2 / v, \end{aligned} \quad (5.23)$$

where x is the offset, v is the average velocity for the medium above the reflector, $t(0)$ is a two-way zero-offset travelttime as indicated in Figure 5.1.

5.2.1.1.2 Multiple horizontal layers

The travelttime equations for multiple horizontal layers were derived by Taner and Koehler (Yilmaz, 1987) as

$$\begin{aligned} t^2(x) &= t^2(0) + x^2 / v_{rms}^2 + \text{higher_order_terms} \\ &\approx t^2(0) + x^2 / v_{rms}^2, \end{aligned} \quad (5.24)$$

where the travelttime is approximated by dropping higher order terms assuming a small-spread arrangement; and the velocities used for stratified layers are no longer internal velocities, but root-mean-square (*rms*) velocities instead, defined as

$$v_{rms}^2 = \frac{1}{t(0)} \sum_{i=1}^N v_i^2 \Delta t_i(0), \quad (5.25)$$

where $t(0) = \sum_{i=1}^N \Delta t_i(0)$, and Δt_i is the normal incidence travelttime through the i th layer, v_{rms} is the time-weighted rms velocity.

5.2.1.2 Dipping Reflector

If, again, a number of geophones are placed on both sides of the source in a line (a split-spread arrangement), the relationship between the reflection travelttime curve and the geometry of a single dipping reflector is shown in Figure 5.2.

The 2-D travelttime equation from a dipping reflector can be obtained using the "law of cosine" (Levin, 1971) as

$$t^2(x) = t^2(0) + x^2 \cos^2 \phi / v^2, \quad (5.26)$$

where ϕ is the dip angle, x is the offset and v is the average velocity of the media. The curve is an asymmetric hyperbola, the shortest traveltimes (t_{min}) along the hyperbola is no longer at the zero-offset position (the normal incidence point), but moves to the up-dip direction.

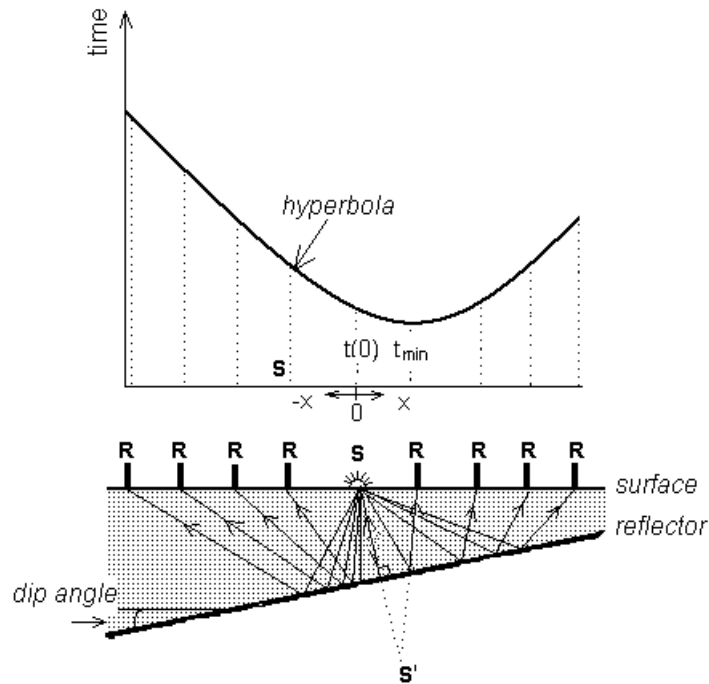


Figure 5.2 A traveltime curve for a dipping reflector— an asymmetric hyperbola.

5.2.2 Diffraction Model

When seismic waves strike a sudden change in the curvature of a subsurface, diffractions will be generated. In many cases, sharp changes in curvature act like a point source (or a line source) which radiates spherical (or cylindrical) waves. A "diffraction" hyperbola is seen on a time section if seismic waves meet sharp changes in curvature (Burger, 1992).

Figure 5.3 shows a diffraction traveltime with its geometrical relationship. We assume the source is placed at S . When energy arrives at the diffractor, waves begin to travel outwards towards receivers laid along the surface. The traveltime is usually hyperbolic and is determined by two components: the time travel from the source to the diffractor and the travel time from the diffractor to the receiver. The traveltime equation can be written as:

$$\begin{aligned}
 t_d &= t_1 + t_2 \\
 &= \frac{(x_1^2 + h^2)^{1/2}}{v} + \frac{(x_2^2 + h^2)^{1/2}}{v}
 \end{aligned}
 \tag{5.27}$$

where v is the average velocity of the media, h is the depth of the diffractor, and x_1 and x_2 are the offsets of the two components. Please note that x_1 is a constant, but x_2 differs with the distance from position O . However, in a special situation (known as common midpoint shooting), when the source and the receiver are coupled together, i.e. $x_1 = x$ and $x_2 = -x$, the diffraction travelttime equation becomes:

$$t_d = \frac{(x^2 + h^2)^{1/2}}{v} + \frac{(x^2 + h^2)^{1/2}}{v} = \frac{2(x^2 + h^2)^{1/2}}{v}
 \tag{5.28}$$

The same equation arises if $x_1 = x = x_2$. This is known as "zero offset shooting".

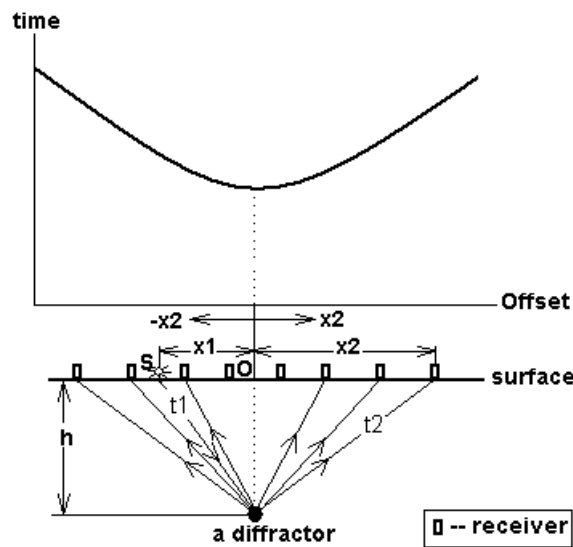


Figure 5.3 Diagram illustrating diffraction raypaths and corresponding travelttime curves.

Diffraction patterns are an important aid in identifying and tracing fault surfaces (Dobrin and Savit, 1988) or isolated ore bodies. In addition, a portion of a diffraction curve may be used for velocity analysis by matching with simulated diffraction patterns of various velocities. On the other hand, diffraction patterns may cause interference on seismic sections and mislead the interpretation of interfaces.

5.2.3 Hyperbolic Move-out

It is customary for a reflection survey in which a large number of geophones are laid on a line with a source at center to record reflection motions. The recorded data are translated

from these offset positions to the middle point between the source and the receiver as if all traces were recorded as zero-offset. The correction is often divided into two categories: normal moveout (NMO) and dip moveout (DMO).

5.2.3.1 Normal Move-out

For a horizontal reflecting interface, the NMO¹⁹ correction is carried out to convert non-zero offset data into zero-offset data at the mid-point between the source and geophone locations. The NMO-corrected data are stacked together according to common middle points (CMP) to improve the signal-to-noise ratio. According to the definition of NMO and Equation (5.23), the traveltime at any offset position (Burger, 1992) is,

$$\begin{aligned}
 t(x) &= t(0) \left(1 + \frac{x^2}{v^2 t^2(0)} \right)^{1/2} \\
 &= t(0) \left(1 + \frac{x^2}{2v^2 t^2(0)} - \frac{x^4}{8v^4 t^4(0)} + \frac{x^6}{16v^6 t^6(0)} + \dots \right) \quad (5.29) \\
 &\approx t(0) + \frac{x^2}{2v^2 t(0)},
 \end{aligned}$$

then the NMO is,

$$(T_{NMO})_x = t(x) - t(0) \approx \frac{x^2}{2v^2 t(0)}, \quad (5.30)$$

which indicates that the NMO correction can be approximated by dropping off higher order terms from Equation (5.29) when the offset is much smaller than reflecting depth. For multi-layered interfaces, Taner and Koehler (1969) gave NMO as,

$$(T_{NMO})_x \approx \frac{x^2}{2v_{rms}^2 t(0)}, \quad (5.31)$$

where the average velocity of a layer is substituted by v_{rms} .

The stacked section can be, ideally, equal to a zero-offset section, that is, as if data are collected from the arrangement which the source and the geophone are coupled together.

¹⁹ the difference in reflection time from a horizontal reflecting surface due to variations in the source-geophone distance (Yilmaz, 1987; Burger, 1992).

In general, the primary reflections are enhanced while multiples are suppressed during the CMP stacking. However, for reflectors with various degrees of dip, the NMO process smears events in the stack. This leads to a need for a correction known as the dip factor.

5.2.3.2 Dip Move-out

There is a residual moveout remaining in the data after NMO correction, which is caused by the reflection dip. This residual moveout is usually removed by dip moveout (DMO) processing. DMO is defined as a process which corrects the effect of dip in the data after normal moveout correction and transforms it to "true" zero-offset data (Deregowski, 1982). Many different DMO algorithms can be found in the literature. One application based on NMO and DMO corrections will be discussed later in this chapter.

5.3 TWO-DIMENSIONAL SEISMIC IMAGING

The main applications of geophysics are in imaging structures and locating drilling targets. The picture of a reflection profile may not reveal true spatial positions and orientations of the reflectors because of the complexities of the survey geometry. We can obtain the structure model in space by forward modeling, or by approximating an inversion. A full elastic wavefield inversion is computer-time intensive and rarely if ever justified by the quality of available field data.

Migration is one of the most common approximate inversion methods in seismic data processing. Migration operations rearrange seismic data so that the true structure information can be reconstructed. One consideration of the inversion process is to discover the impulse response of non-zero-offset or zero-offset reflection for a constant velocity model. As each travelttime from a pair of source-receiver via various paths can form a unique ellipse for a constant velocity, we can obtain many ellipses corresponding to various reflection times. These ellipses superimpose and form the subsurface image. The forward modeling process considers each point in the subsurface as a diffractor. The image is created when spatially well-sampled diffraction wavefields superimpose.

Many modeling/inversion techniques, such as Kirchhoff-based methods, finite difference methods, and ray tracing methods, are often used. Normally, finite difference methods are good in dealing with lateral varying media but need fine grids (a coarse grid causes data aliasing). Ray tracing and Kirchhoff-based methods are better suited to dealing with a subsurface containing relatively simple velocity structures (Wang and Waltham, 1995). A few modeling/inversion processes will be briefly reviewed in order to develop a framework for the discussion in the later section.

5.3.1 Conventional Pre-Stack Migration

Consider Figure 5.4. The traveltimes from the source S to the point P , then from P to the receiver R appears the same for a constant velocity, provided the point P is on the elliptical curve. This ellipse equation can be determined by:

$$\frac{(x - x_0)^2}{\left(\frac{v \cdot t}{2}\right)^2} + \frac{(z - z_0)^2}{\left(\frac{v \cdot t}{2}\right)^2 - h^2} = 1, \quad (5.32)$$

where v is the constant velocity, t is the traveltimes and h is the half distance of the source and the receiver. When all ellipses corresponding to various reflection traveltimes are drawn, a common tangent line to those ellipses defines the true position of a reflector. This leads to a general concept of conventional pre-stack migration. When a shot and receiver coincide with each other, the ellipse becomes a circle and the pre-stack migration becomes a post-stack migration.

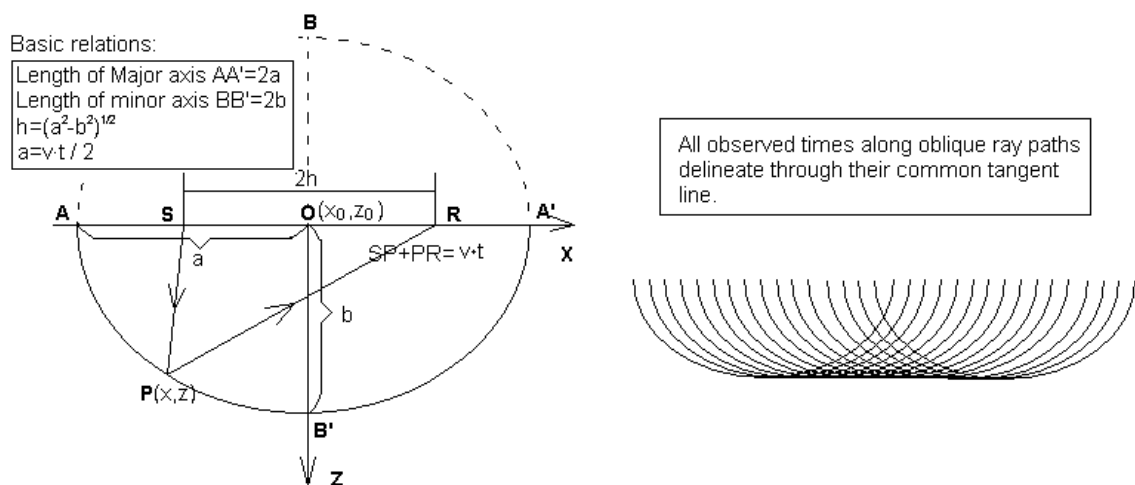


Figure 5.4 Illustration of pre-stack migration for sub-surface reconstruction..

The computing implementation of the conventional migration stack technology was described by Rockwell (1985). It maps the reflections according to their travel times from different pairs of shot-receiver onto the migrated section, and sums all the amplitudes landing at the same grid cell till the entire time section is processed. The migrated section is formed to show the patterns of true sub-surface structures.

5.3.2 Diffraction Summation

An alternative way to consider migration imaging is to think of it as a forward modelling process which is mainly based on Huygen's principle. The characteristic signature of a Huygens' secondary source is a semicircle in the space plane and a hyperbola in the time plane. Diffraction summation methods and the Kirchhoff-type migrations are derived from the above principles (Yilmaz, 1987). Consider each of points on the migrated section as a diffraction point. The method establishes the energy distribution on the time section by summing the amplitudes along a particular diffraction curve, and mapping the summation result to the unique position corresponding to the curve on the migrated section. The true diffractor must be in the position from where the diffraction hyperbola is coincident with the observed one. The diffraction trajectory is determined by Equation (5.27). The computer implementation of the method is illustrated in Figure 5.5. For any given cell (x, y) on the grid of output space, we have a unique hyperbola in time space. By summing the amplitudes along the curve, we can map back to the position (x, y) in the output space. When the diffraction hyperbola is coincident with an observed one, the position (x_0, y_0) will have constructive stacking with strongest energy. The diffraction position will then be imaged.

Factors taken into account in the summing process are the directivity factor, the spherical spreading factor and the wavelet shaping factor. The first two factors describe the amplitude strengths which are determined by wave propagation directions and travel distances, and the last one considers certain phase and frequency characteristics of each Huygens' secondary source. In addition, there are other important considerations such as aperture width and velocity. Details can be found in Lee *et al* (1993).

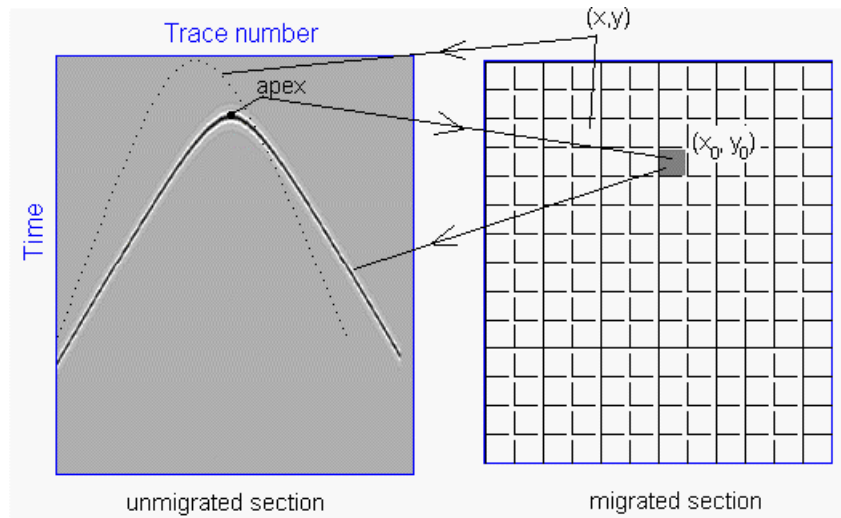


Figure 5.5 Illustration of the computation procedure of diffraction summation.

Figure 5.6(a) shows a synthetic zero-offset diffraction hyperbola generated for a borehole radar survey. A velocity of $109 \text{ m}/\mu\text{s}$ was used in the generation of the data. The trace spacing is 2.5 m. Diffraction summation is used to migrate the data in Figure 5.6 (a) and the result is shown in Figure 5.6(b). There are two mirror diffractor images around the borehole in Figure 5.6(b). The mirror image is a result of the ambiguity of the single borehole configuration. Diffraction summation collapses the diffraction hyperbolas into two dot images, even though we can see fragments of hyperbola which were not collapsed completely. There might be two reasons to explain this incompleteness. First, summation along the hyperbola is always with limited aperture. Second, the amplitude of the synthetic hyperbola does not vary with the direction and distance, i.e., it is not perfectly matched to the arrival.

Aperture width is an important parameter in the practical implementation of Huygens-Kirchhoff-type migration (Yilmaz, 1987). Figure 5.7 displays results for three different aperture widths. The three aperture widths are 125, 10 and 80 traces. The synthetic data has 256 traces. The largest aperture makes the image the most compact. However, in practical data processing, when velocity field variations are unknown, excessively large apertures may raise aberration levels and introduce false detail. More details can be found in Yilmaz (1987) and Lee *et al* (1993).

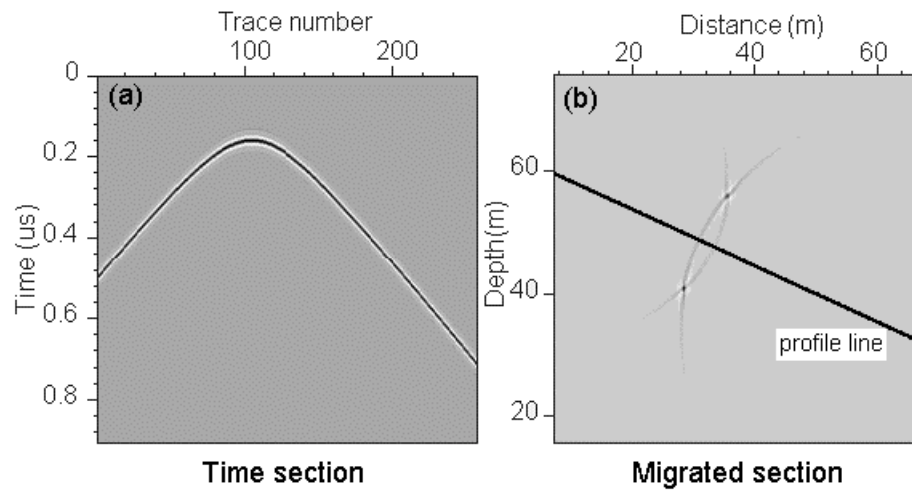


Figure 5.6 (a) The synthetic diffraction hyperbola for a borehole radar survey. (b) The migrated sections shows two mirror images.

The velocity field determines the shape of the move-out hyperbolae (Figure 5.8). Moveout can be used in turn to determine the velocity. We use the same synthetic data as in Figure 5.6 to illustrate migration with different velocities. The results are in Figure 5.9. A velocity higher than the media velocity causes over-migration, one lower causes under-migration.

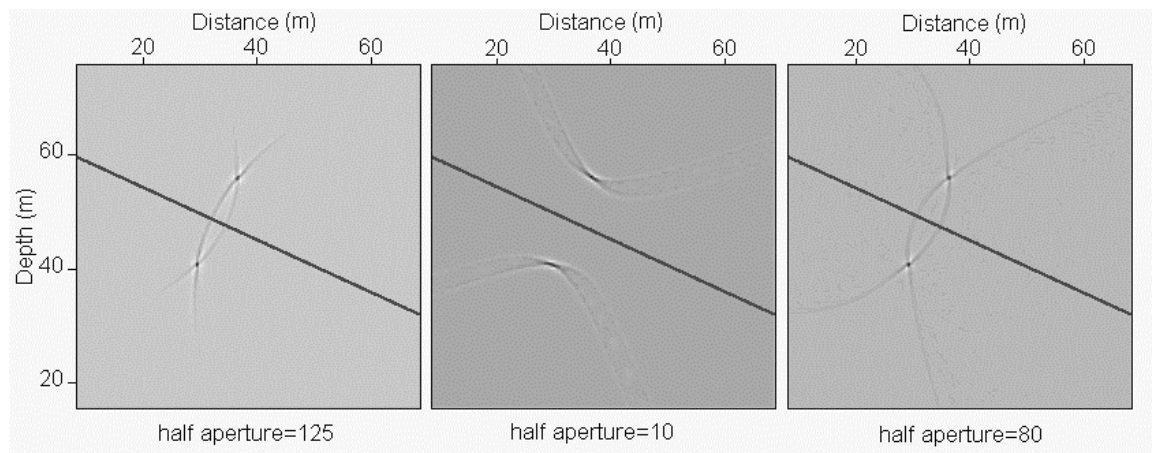


Figure 5.7 The migration results of a synthetic hyperbola with different migration apertures. Large apertures compact the diffraction image.

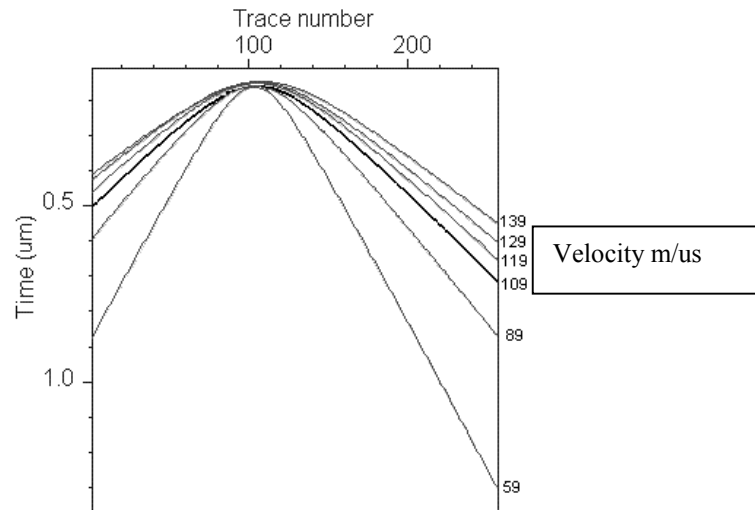


Figure 5.8 Velocity governs the shape of diffraction hyperbolae.

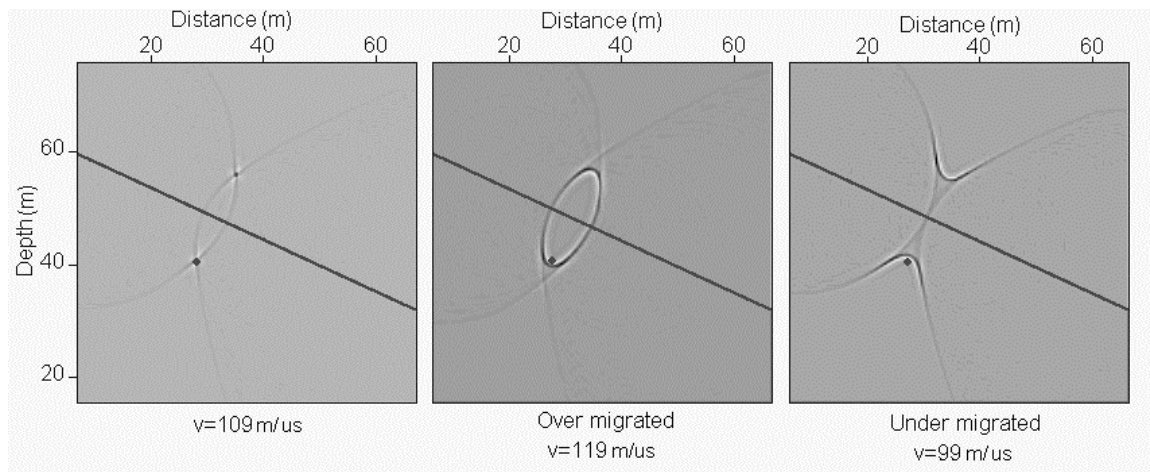


Figure 5.9 The relationship of migration & velocity. The dot indicates the expected point.

5.3.3 Interactive migration on a personal computer

Seismic modeling relates two planes: time-space and space-space, otherwise known as the time section and the base map (Stone, 1994). The ultimate goal of a seismic survey is to map the geological structure onto the base map in 3D space.

With a base map and its corresponding time section, we can view the relationships between the two on a computer screen. We call this interplay. The interplay between a base map and its time section helps in recognizing standard arrival patterns. One can relate simulations to the observed patterns, and vice versa. In this section, we mainly focus on forward modeling.

5.3.3.1 Reflection simulation

This is a simple example of forward modeling. We assume that a reflector is plane, then pick any two points on that plane on the base map and use the traveltime equation (5.26) to calculate the traveltime.

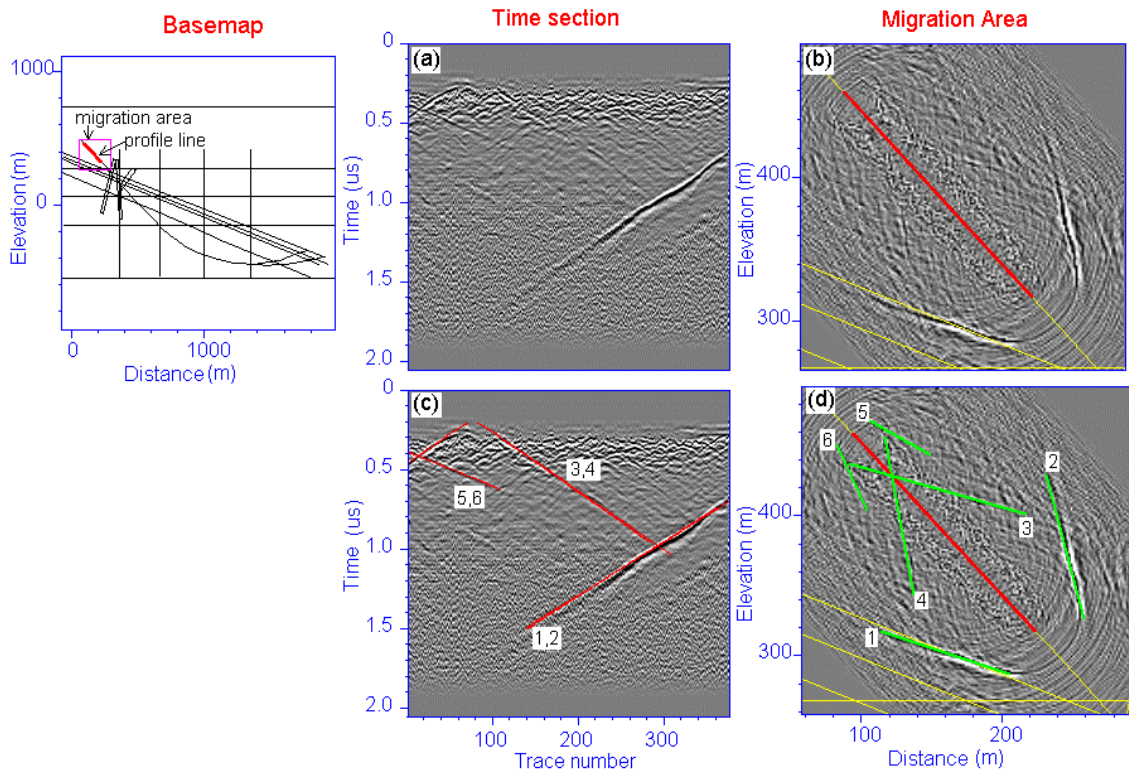


Figure 5.10 A borehole radar survey in South Africa was simulated by reflection modeling. (a) The time section of the profile line shown on the base map; (b) The migrated section; (c), (d) Reflection simulation (green lines) and corresponding reflectors drawn by the computer simultaneously on both maps.

Figure 5.10 shows an application of the reflection simulation procedure. This is a borehole radar survey conducted at Mponeng mine in South Africa. The average velocity of the host rock is about $125 \text{ m}/\mu\text{s}$. By applying diffraction summation, we have a migrated section with the profile line shown Figure 5.10(b). There are six possible reflectors marked by number marks in Figure 5.10(d). With the reflection simulation, the reflectors (green lines) were identified separately. The reflection simulations were mapped onto the time section in Figure 5.10(c) (red lines). The numbers indicate the corresponding reflectors on Figure 5.10(d). The six reflectors actually are three pairs of mirror images.

5.3.3.2 Diffraction simulation

Given a point on a subsurface, we can always simulate the diffraction onto the time section. Like reflection simulation, this can be implemented interactively. The mouse cursor can move over the base map, with by a simulated diffraction curve on the time section. When the simulated curve matches an observed diffraction event, the cursor position on the base map is assumed to be a diffractor.

In Figure 5.11 we simulate a number of closely laid diffractors (in magenta) from a reflector in Figure 5.11(b). The simulated hyperbolas on the time section are shown in Figure 5.11 (a). We can see that these hyperbolas delineate the observed event, if the reflected wavefield is spatially well sampled.

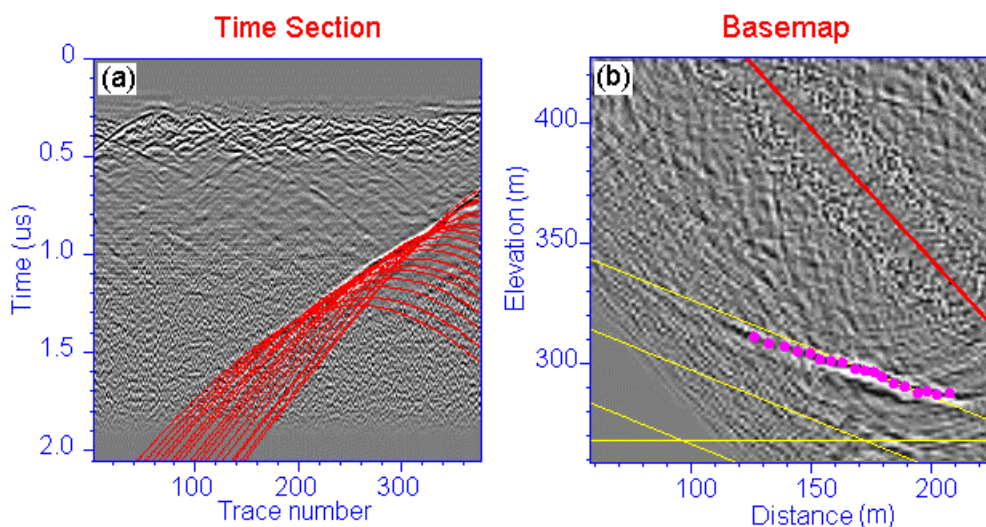


Figure 5.11 A migrated reflector (marked by the magenta dots on (b)) is tangent to the diffraction curves (the red curves on (a)).

Another example of diffraction simulation is given in Figure 5.12. A borehole radar survey of the nickel sulphide ore shoot was carried out at Hunt mine, Kambalda, West Australia. A basemap and shotline is shown in Figure 5.12(a). The average velocity used for migration was $110 \text{ m}/\mu\text{s}$. The hyperbolic diffraction patterns on the time section become, after diffraction summation (b), dark ridges track ore channels (see Figure

5.12(c)). We considered those dark ridges as isolated diffractors. The simulated diffraction curves match well with the observed diffraction patterns.

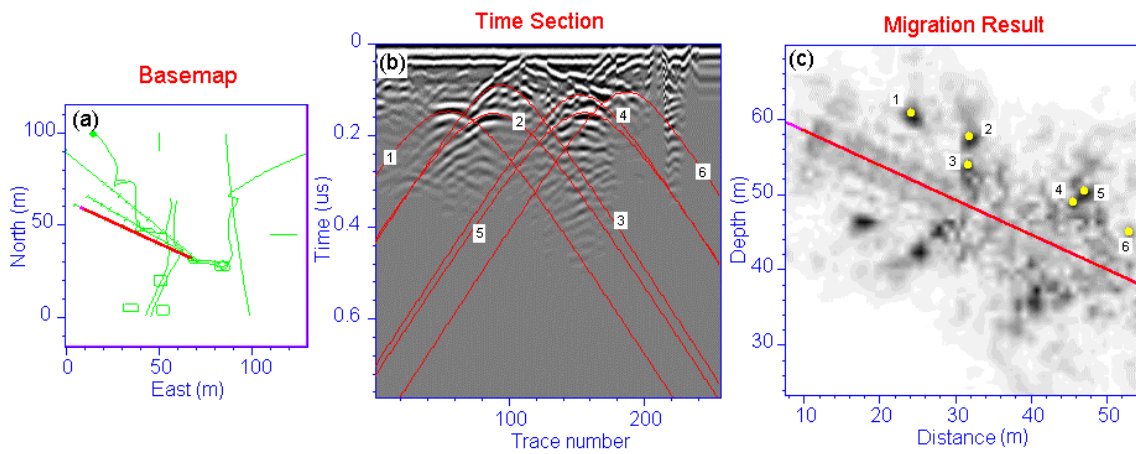


Figure 5.12 The hyperbolic diffraction patterns (red curves) on (b) match those scattering locations (yellow dots) on migrated image (c).

5.3.3.3 Interplay with velocity-time space

When the migration velocity is unknown, one can find the velocity by the best fitting observed diffraction hyperbola on the time section, see Figure 5.8. The simultaneous velocity adjustment allows the user to do simple velocity analysis on the screen by moving the mouse cursor around time-velocity space.

5.4 IMAGING WITH SPARSE DATA

Aliasing occurs when the sampling rate is lower than the limit, that is, the sampling frequency is less than twice the Nyquist frequency. When the spatial sampling rate is very low, the image can not be formed properly. We call the data array sparse. In this section, we discuss non-uniform sparse data problems and solutions in imaging with sparse data sets.

5.4.1 Event Migration

Non-uniformly sampled sparse data sets frequently occur in mining and environmental geophysics. With non-uniform and very sparse arrays, seismic mapping of reflectors becomes difficult. Figure 5.13 shows an example of a synthetic common-offset reflection section. The diffraction summation method migrates a dense sampled array into a well-defined reflector (top row). When the sampling rate drops significantly, we get a set of rings which fail to describe the tangent reflection plane.

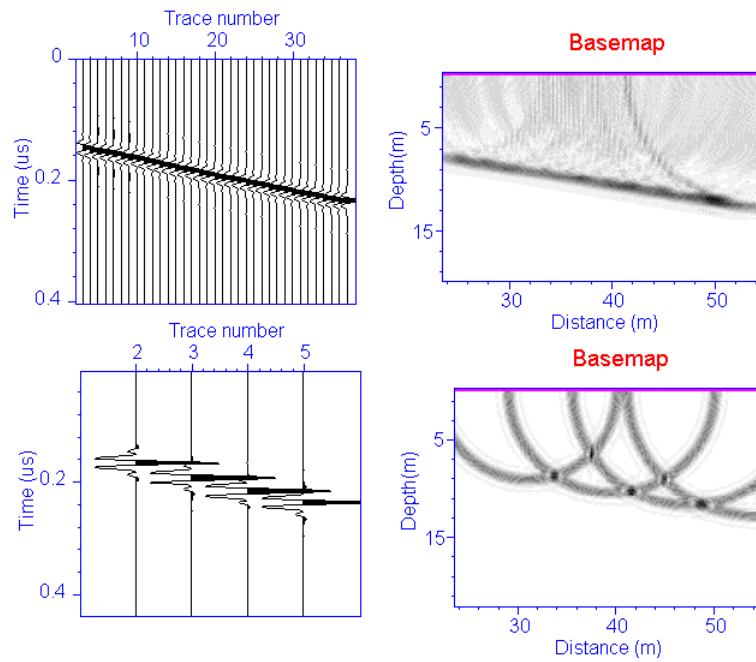


Figure 5.13 Diffraction summation for dense sampled data (on the top row); (b) Diffraction summation for a very sparse data set (on the bottom row).

Instead of simulation from the base map to the time section as described in the previous section, we can invert the process, i.e. interplay from the time section onto the base map. We call this process event migration. Event migration migrates any two points on a time section to their true reflection positions based on the common tangent line relationship of the two corresponding elliptical reflectors. In Figure 5.14 there are three possible relationships of two ellipses: (a) no intersection (four possible common tangent lines/solutions); (b) intersection (two possible solutions) and (c) one ellipse inside the other (no solution), as shown by Figure 5.14. The multiple solutions of a reflector in 3D space can be reduced by other prior geological information.

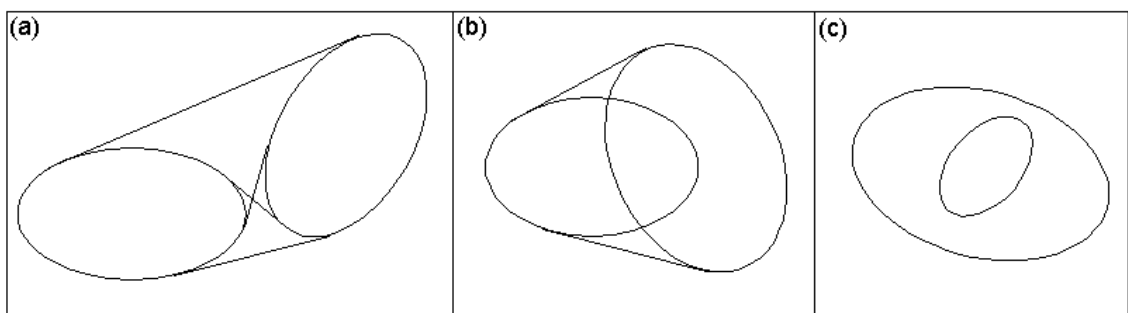


Figure 5.14 Event migration seeks common tangents of two elliptical reflectors. There are three possible relationships of the two ellipses as shown here. This can give upto 4 possible solutions/tangent lines.

The event migration method can be illustrated by the geometrical relationship shown in Figure 5.15. We assume that we have two source-receiver pairs laid along a line on the surface. Their corresponding midpoints are at $M1$ and $M2$. We need to find out the position $R1$ and $R2$ of the true reflection points according to the reflection times t_1 and t_2 .

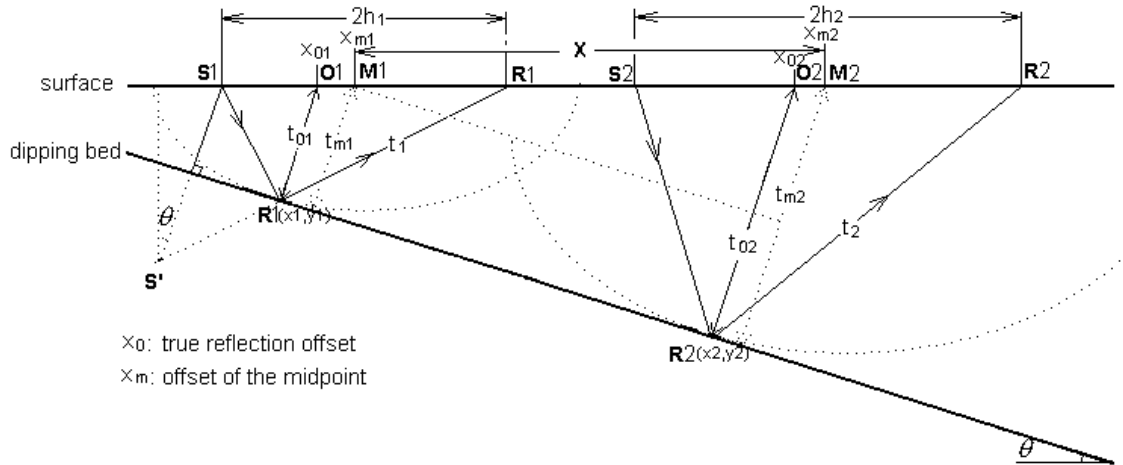


Figure 5.15 The geometrical relationship between CMP and the true reflection point for a dipping reflector.

According to the traveltime equation (5.26), the traveltimes between the source-receiver in Figure 5.15 can be written as

$$\begin{cases} t_1 = \left[t_{m1}^2 + \left(\frac{2h_1 \cos \theta}{v} \right)^2 \right]^{1/2} = \left[t_{m1}^2 + \left(\frac{2h_1}{v} \right)^2 - \left(\frac{2h_1 \sin \theta}{v} \right)^2 \right]^{1/2} \\ t_2 = \left[t_{m2}^2 + \left(\frac{2h_2 \cos^2 \theta}{v} \right)^2 \right]^{1/2} = \left[t_{m2}^2 + \left(\frac{2h_2}{v} \right)^2 - \left(\frac{2h_2 \sin \theta}{v} \right)^2 \right]^{1/2} \end{cases} \quad (5.33)$$

We can partition equation (5.33) into two processes (Zhou et al., 1995): one is called NMO,

$$\begin{cases} t_1^2 = t_{n1}^2 + \left(\frac{2h_1}{v} \right)^2 \\ t_2^2 = t_{n2}^2 + \left(\frac{2h_2}{v} \right)^2 \end{cases}, \quad (5.34)$$

and the other is called DMO,

$$\begin{cases} t_{m1}^2 = t_{n1}^2 + \left(\frac{2h_1 \sin \theta}{v}\right)^2 \\ t_{m2}^2 = t_{n2}^2 + \left(\frac{2h_2 \sin \theta}{v}\right)^2 \end{cases}, \quad (5.35)$$

where t_{n1} and t_{n2} are equivalent to the time at midpoint after NMO correction which can be obtained by the conventional NMO equation (5.23); t_{m1} and t_{m2} are the normal two-way traveltimes at the midpoints.

Next, we need to find the dip angle θ . From the geometry relationship shown in Figure 5.15 we have,

$$t_{m2} = t_{m1} + \frac{2x \sin \theta}{v} \quad (5.36)$$

If we let $y = \frac{2 \sin \theta}{v}$, equation (5.35) and equation (5.36) become

$$\begin{cases} t_{m1}^2 = t_{n1}^2 + h_1^2 y^2 \\ t_{m2}^2 = t_{n2}^2 + h_2^2 y^2 \\ t_{m2} = t_{m1} + xy \end{cases} \quad (5.37)$$

From equation (5.37), we can solve the variable y ,

$$y^2 = \begin{cases} \frac{-b^2}{(2ab - 4x^2 t_{n1}^2)}, & \text{for } a^2 = 4x^2 h_1^2 \\ \frac{-(2ab - 4x^2 t_{n1}^2) \pm \sqrt{(2ab - 4x^2 t_{n1}^2)^2 - 4b^2(a^2 - 4x^2 h_1^2)}}{2(a^2 - 4x^2 h_1^2)}, & \text{otherwise} \end{cases}, \quad (5.38)$$

where $a \equiv h_2^2 - h_1^2 - x^2$, $b \equiv t_{n2}^2 - t_{n1}^2$. The dip angle is then obtained by

$$\theta = \sin^{-1}(vy/2)$$

Note that y has four possible solutions, so does the dip angle. By using Levin's relationship (1971),

$$\begin{cases} t_{01} = t_{m1} - \frac{h_1^2}{t_{m1}} \left(\frac{2 \sin \theta}{v} \right)^2 \\ t_{02} = t_{m2} - \frac{h_2^2}{t_{m2}} \left(\frac{2 \sin \theta}{v} \right)^2 \\ x_{01} = x_{m1} - \frac{h_1^2 2 \sin \theta}{t_{m1} v} \\ x_{02} = x_{m2} - \frac{h_2^2 2 \sin \theta}{t_{m2} v} \end{cases},$$

the true reflection locations $R1$ and $R2$ can be obtained by ,

$$\begin{cases} x_1 = x_{m1} - \frac{h_1^2}{t_{m1}} \frac{2 \sin \theta}{v} - \frac{t_{01} v}{2} \sin \theta \\ y_1 = \frac{v t_{01}}{2} \cos \theta \\ x_2 = x_{m2} - \frac{h_2^2}{t_{m2}} \frac{2 \sin \theta}{v} - \frac{t_{02} v}{2} \sin \theta \\ y_2 = \frac{v t_{02}}{2} \cos \theta \end{cases} \quad (5.39)$$

As the dip angle has a maximum of four possible solutions, equation (5.39) can have a maximum of four pairs of solutions. Event migration maps any two reflection points on a time section into their true position on the space map. The true reflection locations R_1 and R_2 are the common tangential locations of the two corresponding ellipses produced by the two reflections of the reflector.

With equation (5.39), we can migrate any two points on the time section onto the base map. The procedure is as follows:

- 1) Pick travel time t_1 and t_2 on the seismic/radar section.
- 2) Compute NMO corrected travel times t_{n1} and t_{n2} at the common middle points $M1$ and $M2$ using equation (5.34).
- 3) Compute y using equation (5.38).

- 4) Calculate the DMO-corrected travel times t_{m1} and t_{m2} at $M1$ and $M2$ by equation (5.35).
- 5) Compute the true reflection locations $R1$ and $R2$ on the base map by equation (5.39). (There are four possible solutions).

Event migration is an inversion process. It gives the user a direct view of the migrated result as with the other interplay functions mentioned before. An application of event migration can be found in Figure 5.16. We use the same data set in Figure 5.10 but we do the interplay in the opposite way this time. The three events (marked with A, B, C in the time-space plane) in Figure 5.16 (a) were picked separately on the time section. They were mapped onto the base map (shown in Figure 5.16(b)). The green lines are the common tangent lines calculated from the three events. Each letter denotes the same group of common tangent lines that an event produced. The results match observed reflectors well. With the constraint of prior geological information, we can remove those common tangent lines with conflicting directions and update the result as shown in Figure 5.16(c).

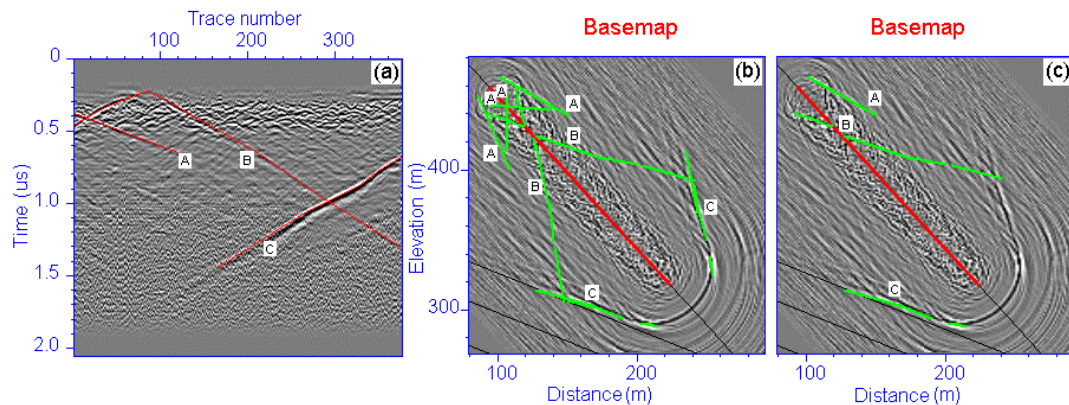


Figure 5.16 (a) Radar data mapping of events A, B & C with event migration; (b) Mapped events on the basemap with their mirror images; (c) Mirror images in (b) eliminated according to prior geological knowledge. The background image in (b) & (c) is the Kirchhoff migration result of (a).

5.4.2 Common tangent line stacking

Conventional stacking migration algorithms cannot image the reflector properly when the data are sparse, since there are not enough data to make the stacking constructive. In Figure 5.17, there are five transceivers with a reflector model (a common tangent line).

Diffraction summation migration gives five circles spreading in the plane. In this case, we can image the reflections along the common reflection tangent lines rather than the reflection ellipses. In fact, it is easier to identify where the true reflector lies by stacking common tangent lines of any two reflection ellipses. If we accumulate all the reflection energy along the common tangent lines, the true reflector will be constructively stacked up. We call this method common tangent line stacking. This method can be realized as either an inverse mapping process or a forward modeling procedure as described below.

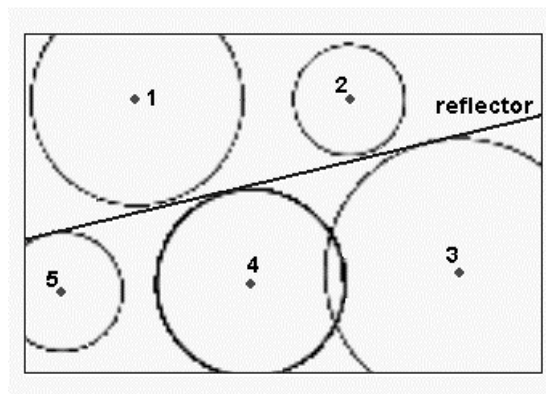


Figure 5.17 Each pair of circles has at least two common tangent lines. After all possible combination of two circles common tangent lines are mapped, the hypothetical reflector should accommodate the most repeated common tangent lines from mapping.

5.4.2.1 Inverse mapping

This method is an extension of the event migration in Section 5.4.1. The procedure can be divided into three steps. Firstly, each pair of common tangent points can be obtained from two traveltimes, which are combined from any two samples over the entire time section. We calculate the energies²⁰ at these time samples. Finally, the energy production of two picked points on the time section is used to accumulate on the grid points along the common tangent line segment on the base map. This process will continue until every tangent line from the entire time section is mapped and stacked onto its space plane (the base map). The mapped true reflectors are expected to have significant larger energies compared to others, as the energies along the true reflector will constructively accumulate. The method is simple and fast, since the number of traces on the time section is small. The method works for any source-receiver geometry. Two synthetic examples of common tangent line stacking are given in the following section.

5.4.2.2 Synthetic Examples of Sparse Data Imaging

A synthetic model of a dipping reflector and two-trace section were tested in Figure 5.18. Diffraction summation methods could not image the reflector as the two-trace records produced two intersecting half circles. However, by applying the common tangent line stacking method, the hypothetical reflector was mapped correctly.

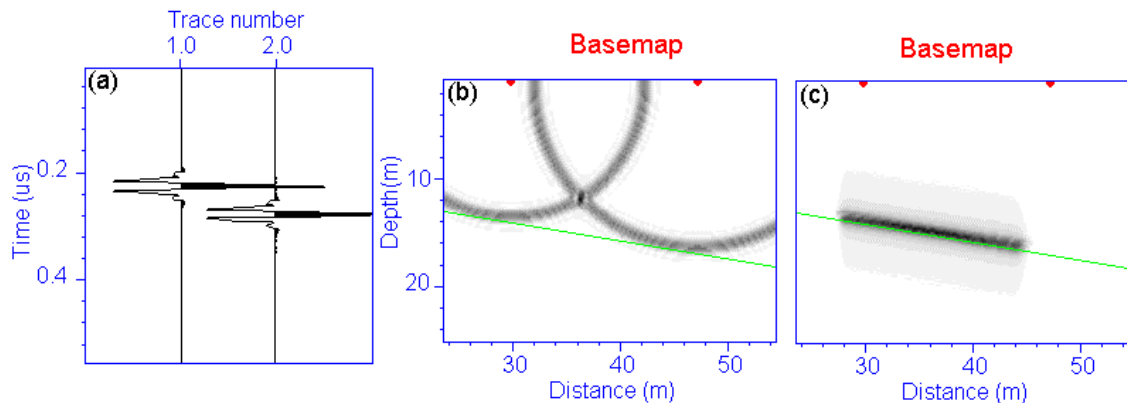


Figure 5.18 Inverse mapping. (a) A synthetic two trace data set and its base map. The green line indicates the reflection plane and two red dots show the receiver positions; (b) Diffraction summation results in two semicircles on the base map. (c) Common tangent line stacking provides the correct reflector image.

Another synthetic example took the situation of a borehole radar investigation of karsts at nitrocellulose plant in Lavrion (Mason et al., 1995), where the subsurface was faulted in vertical blocks. Surface ground penetrating radar was restricted in the area and boreholes provide the only option for subsurface mapping. The hexagonal borehole layout is mimicked and virtual reflectors are modeled as the green lines shown in Figure 5.19(a). Diffraction summation migrates the data into 9 circles (Figure 5.19(c)) which makes it hard to locate the two common tangent planes. By applying common tangent line stacking, all common tangent lines are mapped and stacked to yield Figure 5.19 (d) and (e). It is evident that the common tangent line stacking makes the two desired reflectors more prominent, especially after the modification of the gray scale as shown in Figure 5.19(e).

²⁰ the envelope function calculates the instantaneous power

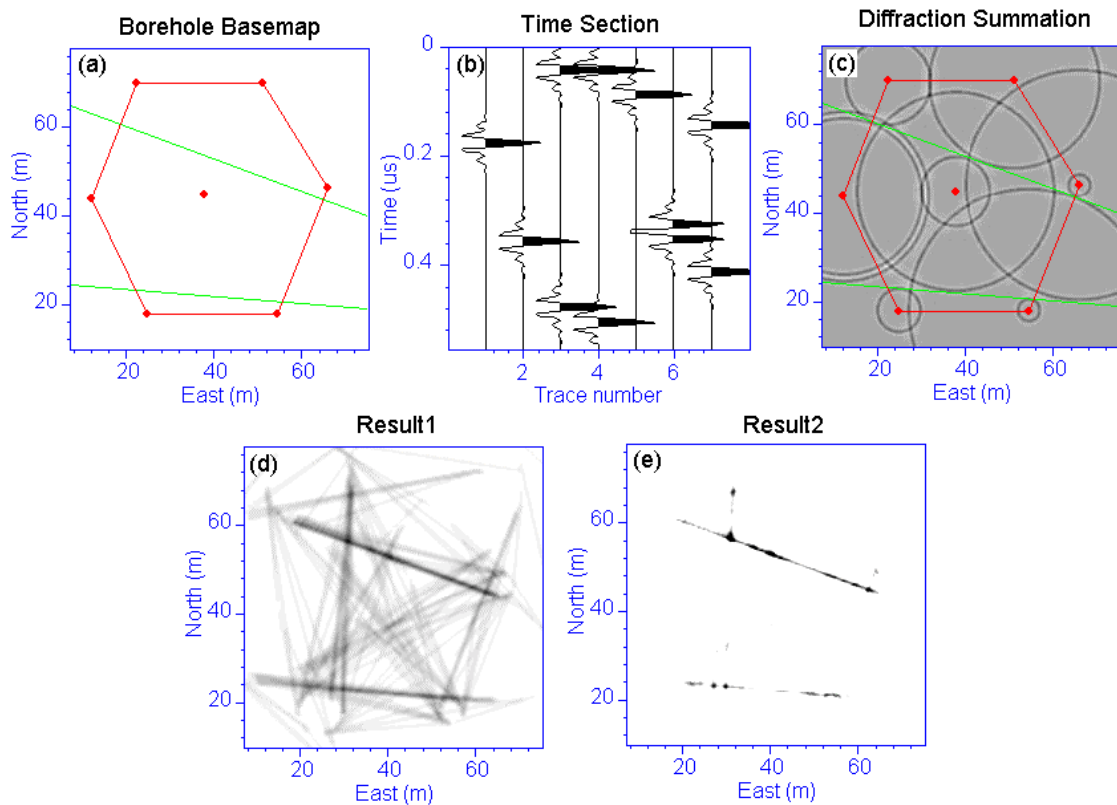


Figure 5.19 Inverse mapping. (a) A base map model shows 7 receivers (marked by red dots) and two reflection planes (green lines) corresponding to the synthetic sparse data in (b); (c) Diffraction summation migrates the data into circles; (d) The result from common tangent line stacking; (e) The image from (d) with different gray levels.

5.4.2.3 Forward mapping

An alternative way to image with sparse data is to construct the process as a forward modelling procedure as illustrated in Figure 5.20. If a shot line is fixed, we can compute the travel times and the reflection positions from each shot-receiver pair for any given reflector. Every travel time can be traced to the corresponding position on the time section. A window of the envelope function around each traced time is taken. The average product between any two windows is calculated and distributed/accumulated along the line segment between the corresponding reflection positions on the migrated section. If this operation is repeated for all possible reflectors on the base map, true reflectors will be enhanced.

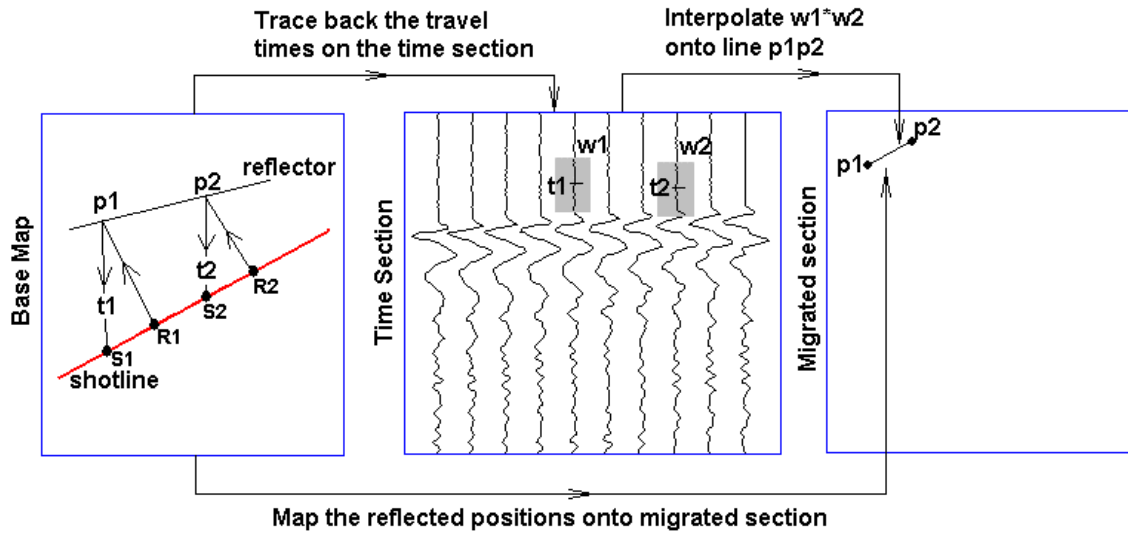


Figure 5.20 Forward mapping procedure. For any given reflector, we can trace the corresponding travel time to the time section. The average energy of the product of travel time t_1 and t_2 is assigned to line p_1p_2 on the migrated section. An accumulation of energy should reveal the real reflector in theory.

5.4.2.4 Synthetic examples

The same synthetic model used in Figure 5.18 was used to test the forward mapping method. The result in Figure 5.21 reveals the reflector.

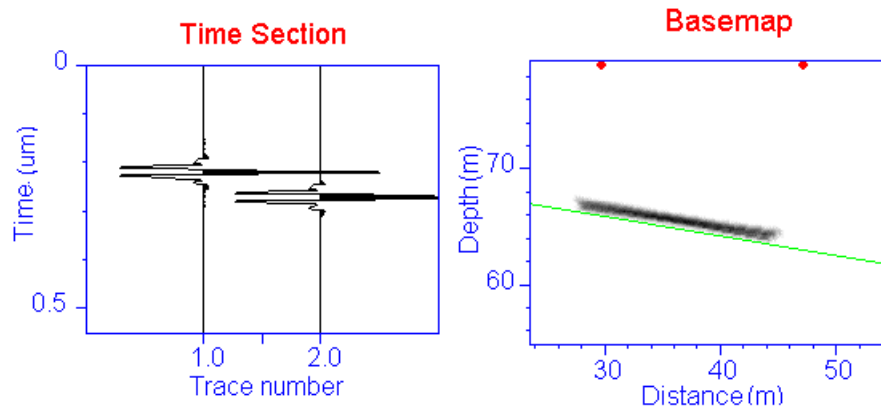


Figure 5.21 Forward mapping. The green line indicates the reflection plane and the two red dots show the receiver positions.

Figure 5.22 shows the result of the forward mapping process using the synthetic model of Figure 5.19. The results from two methods are similar. The result from Figure 5.22(e) is slightly inferior as the accumulated energy on the reflectors was not strong enough to suppress unwanted energy. The phenomena may be caused by discrete angles of steep reflectors which would result inhomogeneous coverage over the basemap plane.

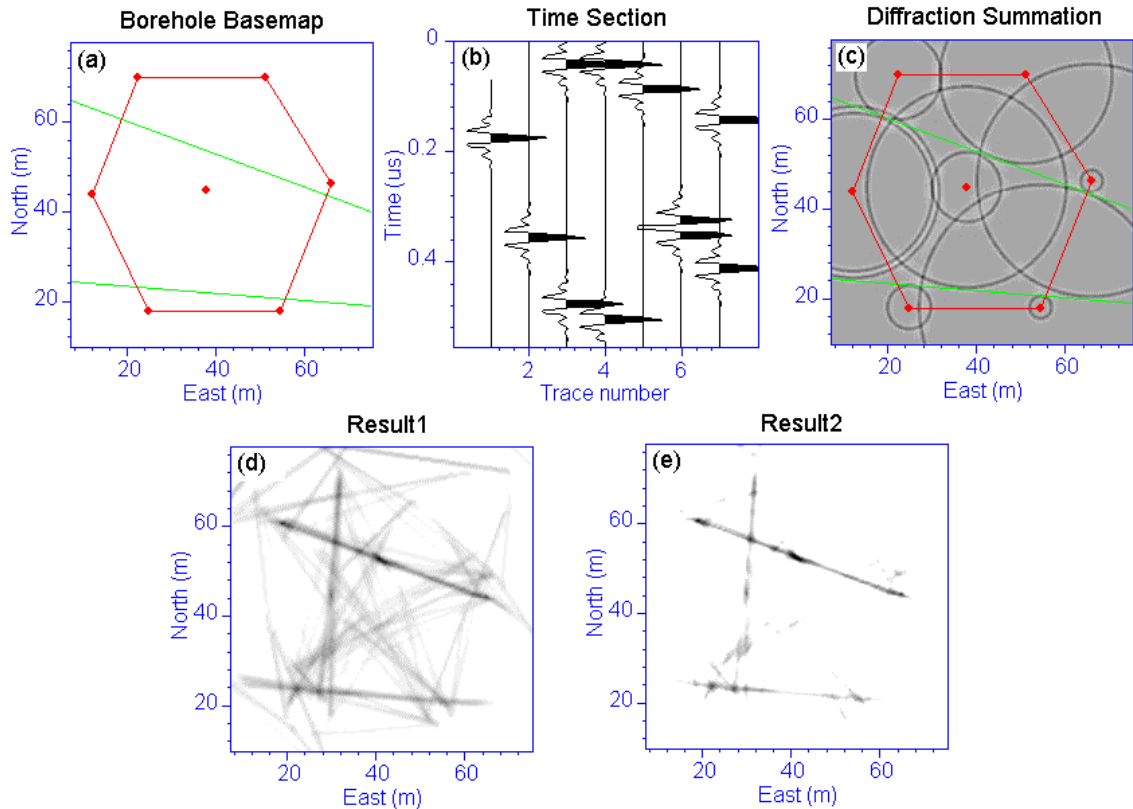


Figure 5.22 Forward mapping. (a) A base map model shows 7 receivers (marked by red dots) two reflection planes (green lines) corresponding to the synthetic sparse data in (b); (c) Diffraction summation migrates the data into circles; (d) The result from common tangent line stacking; (e) The image from (d) with different gray levels.

5.5 DISCUSSIONS AND CONCLUSIONS

The computer enables the interplay between space-space, space-time and velocity-time, which helps us to recognize the standard patterns in a complicated environment, so that the quality of geophysical interpretation can be improved.

Working with non-uniform and sparse data is always difficult. Wave equation based techniques cannot deal with very sparse data sets. Event migration and common tangent line stacking can assist in mapping reflectors with very sparse data sets. These methods are not as widely used as they should be. The common tangent line stacking method maps reflectors by accumulating the energy from the common tangent lines on any two possible reflecting points on the space plane. It can be realized in two approaches: inverse and forward mapping. They were tested on synthetic data. The results were

promising. However, the methods are computationally costly operations and not suitable to dense data arrays.

Event migration is derived under the assumption that the focus points of two ellipses are in a line. In general this assumption is untenable (Figure 5.23(a)), event migration gives only an approximated result. The approximation can be achieved as event migration can be partitioned into two processes: NMO and DMO. NMO corrected data can be approximated as zero offset data. The ellipse of a source-receiver pair becomes a circle, and the centers of any two circles can be in the same line (see Figure 5.23(b)). It means that we can still apply event migration, derived in a special case, into a general situation. For more accurate imaging, the above event migration algorithm needs to be modified to accommodate the more general situation.

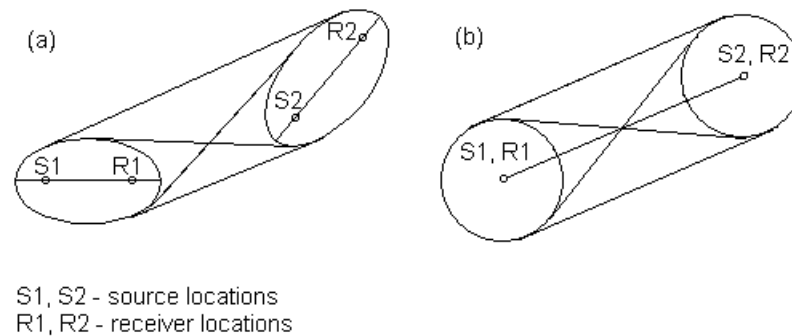


Figure 5.23 The event migration algorithm developed in this chapter is not applicable to the general case where the major axes of any two ellipses are not necessarily in a line. (b) The event migration can be approximated by converting the non-zero offset data into zero offset.

CHAPTER 6 DISCUSSION AND CONCLUSION

Seismic surveys collect a great amount of data. These data must be processed and interpreted in order to extract useful information about the earth. Data processing and imaging techniques rely heavily on computers. Research on the development of effective interactive computing methods is needed. This thesis is only a start.

Event picking is an important step in seismic data reduction. The task is similar in many ways to that of edge detection in picture processing, or automatic echo detection in long range radar. However, these tasks are known to be difficult to automate, but they are no more so than that of building a seismic interpreter's knowledge and judgment into a machine. We need interactive picking in which the interpreter, while he may be remote, always stays in control.

There are two approaches to interactive picking. One is based on cross-correlation, either visual or mathematical; the other is based on using the instantaneous phase to capture the instant at which either the real or the imaginary part of the arrival passes through zero. The choice of which method to implement is left to the discretion of the interpreter.

The software package *SeisWin* was used as a vehicle to test interactive picking concepts. The interactive picking system that was implemented there included a number of procedures for picking the first break, later arrivals for 2-D data and as well as a technique for horizon tracking in a 3D data volume. Experience of the dynamics of user interaction was gained by testing different combinations of picking and pick-correction on a wide range of field data, such as full waveform sonic data, reflection and tomographic in-mine borehole radar data and seismic 3D data. The procedures implemented proved efficient and flexible enough to deal with a wide range of complex situations. The main issue was found to be not so much algorithm complexity as the quality of the dialog between interpreter and machine. We found it possible to build a

workable picking machine, with sufficient interactive capability to ease the detection, investigation and correction of event picking errors.

The second part of the thesis was concerned with issues of seismic display. Seismic interpreters depend on the quality of the final display. Improper display parameters, such as dynamic range and display scales, can contribute to a poor interpretation of seismic data. In order to maximize information transfer from machine to interpreter, it is necessary to optimize display quality. Various traditional methods used to enhance the visibility of an image were analysed. We showed that some of the standard tools of digital image processing could be applied with advantage to seismic images. Filters like high-pass and median filters are easy to implement and efficient. Edge detectors are also good in detecting faults and structural trends. Different approaches on gain, contrast modification and uses of color-map were also discussed.

Uniform coverage and uniform illumination of targets is ideal in seismic data acquisition. Sparse and non-linear arrays however can not be avoided. Wave equation based imaging techniques do not work for sparse data. Event migration and the common tangent line stacking are developed especially for reconstructing a plane. Event migration maps any two points on the time section to its space plane, and allows a direct view of the migrated result. Common tangent line stacking maps the reflector by accumulating the energy from the common tangent lines on any two possible reflecting points on the space plane. It can be realized in two approaches: inverse and forward mapping. The two approaches were tested on synthetic data and the results were found to be satisfactory. Common tangent line stacking is computationally costly and not well suitable to densely populated data arrays.

All of the new functions developed through this study have been implemented within the package *SeisWin*. This software has attracted industry users especially interested in tracking 3D seismic horizons. An ACARP project with support of industry users group has been awarded for further development of the software.

BIBLIOGRAPHY

- Baer, M. and Kradolfer, 1987, An automatic phase picker for local and teleseismic events: Bull. Seism. Soc. Am. 77, 1437-1445.
- Baxes, G. A., 1994, Digital Image Processing – Principles and Applications, John Wiley & Sons Inc.
- Bois, P., 1980, Autoregressive pattern recognition applied to the delimitation of oil and gas reservoirs: Geophys. Prosp., 28, 572-591.
- Boschetti, F., Dentith, M.D., and List, R.D., 1996, A fractal-based algorithm for detecting first arrivals on seismic traces: Geophysics, 61, 1095-1102.
- Bracewell, R. N., 1986, The Fourier transform and its applications (second edition, revised), McGraw-Hill Book Company.
- Burger, H. R., 1992, Exploration geophysics of the shallow subsurface: Prentice-Hall, Inc.
- Chang, W. F. and McMechan, G. A., 1986, Reverse-time migration of offset vertical seismic profiling data using the excitation-time imaging condition: Geophysics, 51, 67-84.
- Claerbout, J. F., 1971, Toward a unified theory of reflector mapping: Geophysics, 36, 467-481.
- Cochran, M. D., 1973, Seismic signal detection using sign bits: Geophysics, 38, 1042-1052.
- Coultrip, R. L., 1993, High-accuracy wavefront tracing traveltimes calculation: Geophysics, 58, 284-292.
- Coppens, 1985, First arrival picking on common-offset trace collection for automatic estimation of static correction: Geophys. Prosp., 33, 1212-1231.
- Deregowski, S. M., 1982, Dip-moveout and reflector point dispersal: Geophys. Prosp., 30, 318-322.
- Dobrin B. and Savit, C. H., 1988, Introduction To Geophysical Prospecting, Fourth Editions, McGraw-Hill International Editions.

- Dorn, G. A., Cole, M. J. and Tubman, K. M., 1995, Visualization in 3-D seismic interpretation: The Leading Edge, 14, 1045-1049.
- Dorn, G. A., 1998, Modern 3-D seismic interpretation: The Leading Edge, Vol. 17, 1262-1272.
- Douglas, A., D. Bowers and J. B. Young, 1997, On the onset of *P* seismograms: Geophys. J. Int., 129, 681-690.
- Earle, P. S., and Shearer, P. M., 1994, Characterization of global seismograms using an automatic-picking algorithm: Bull. Seism. Soc. Am. 84, 366-376.
- Ervin, C. P., McGinnis, L. D., Otis, R. M., and Hall, M. L., 1983, Automated analysis of marine refraction data: a computer algorithm: Geophysics, 48, 582-589.
- Feagin, F. J., 1981, Seismic Data Display and Reflection Perceptibility: Geophysics, Vol. 46, 106-120.
- Foley, J.D., Dam, A.V., Feiner, S.K. and Hughes, J.F., 1991, Computer Graphics: Principle and Practice, Second Edition, Addison-Wesley Publishing Company.
- Foufoula-Georgiou, E., and Kumar, P., Wavelets in Geophysics, Academic, San Diego, Calif., 1994.
- French, W., 1975, Computer migration of oblique seismic reflection profiles: Geophysics, 40, 961-980.
- Gardner, G. H. F, 1985, Migration of Seismic Data -- Geophysics reprint series No. 4, Society of Exploration Geophysicists.
- Gelchinsky, B. T., and Shtivelman, V., 1983, Automatic picking of first arrivals and parameterization of travelttime curve: Geophys. Prosp., 31, 915-928.
- Gonzalez, R. C. and Woods, R. E., 1993, Digital Image Processing, Addison-Wesley Publishing Company.
- Gu, H., H. Zhou and X. Zhang, 1992, Automatic pick of first arrival time: Geophysical & Geochemical Exploration, 16(2), 120-129.
- Hansen, K. M., Roy-Chowdhury, K. and Phinney, R. A., 1988, The sign filter for seismic event detection: Geophysics, 53, 1024-1033.

- Hanyga, A., 1988, Numerical tracing of rays and wavefronts. In: Seismological Algorithms (ed. D. Doornbos), Academic Press, Inc., 169-233.
- Hatherly, P. J., 1982, A computer method for determining seismic first arrival times: Geophysics, 47, 1431-1436.
- Helstrom, C. W., 1960, Statistical theory of signal detection, Pergamon Press Inc.
- Haykin, S., 1991, Adaptive filter theory (second edition), Prentice-Hall Inc., Englewood Cliffs.
- Herron, D. A., 2000, Horizon autopicking: The Leading edge, Vol. 19, 491-492.
- Kabir, I., 1996, High-Performance – Computer Imaging, Manning Publications Co.
- Kidd, G. D., 1999, Fundamentals of 3-D seismic volume visualization: The Leading edge, Vol. 18, 702-712.
- Knapp, C. H., and Carter, G. C., 1976, The generalized correlation method for estimation of time delay: IEEE Trans. Acoust. Speech Signal Process, 24, 320-305.
- Kowalik, W.S. and Glenn, W.E., 1987, Image processing of aeromagnetic data and integration with Landsat images for improved structural interpretation: Geophysics, 52, 875-884.
- Kumar, P. and Fougoula-Georgiou, E., 1994, Wavelets in Geophysics, American Press.
- Kusuma, T. and Fish, B. C., 1993, Toward more robust neural-network first break and horizon pickers, 63rd meeting of the Soc. Expl. Geophys.
- Le, L. H. T., and Nyland, E., 1990, Pattern analysis of seismic records: Geophysics, 55, 20-28.
- Lee, D., Jackson, G. M. and Mason, I. M., 1993, Partially coherent migration: Geophysics, 58, 1301-1313.
- Levin, F.K., 1971, Apparent velocity from dipping interface reflection: Geophysics, 36, 510-516.
- Levin, F.K. and Shah, P. M., 1977, Peg-leg multiples and dipping reflectors: Geophysics, 42, 957-981.
- Lim, J. S., 1990, Two-dimensional Signal and Image Processing, Prentice-Hall Inc.

- Liu, H. H., and Fu, K. S., 1982, A syntactic pattern recognition approach to seismic discrimination: *Geoexplor.*, 20, 183-196.
- Loewenthal, D and Hu, L.-Z., 1991, Two methods for computing the imaging condition for common-shot prestack migration: *Geophysics*, 56, 378-381.
- Mason, I.M., Hargeaves, J., Zhou, B. and Claassen, D.M., 1995, Radar investigation of karsts beneath H.A.I. nitrocellulose plant, Lavrion, Attica: (Internal report).
- McCormack, M. D., Zaucha, D. E. and Dushek, D. W., 1993, First-break refraction event picking and seismic data trace editing using neural networks: *Geophysics*, 58, 67-78.
- McEvelly, T. V. and Majer, E. L., 1982, ASP: An automated seismic processor for microearthquake networks: *Bull. Seism. Soc. Am.* 72, 303-325.
- McQuillin, R., Bacon, M. and Barclay, W., 1984, *An Introduction to Seismic Interpretation*, Graham & Trotman Limited, London
- Murat, M. E., Rudman, A. J., 1992, Automated First Arrival Picking: A Neural Network Approach: *Geophysical Prospecting*, 40, 587-604.
- Neidell, N. S., and Taner, M. T., 1971, Semblance and other coherency measurements for multichannel data: *Geophysics*, 33, 105-126.
- Nestvold, E. O., 1992, 3-D seismic: Is the promise fulfilled?: *The Leading Edge*, Vol. 11, 12-19.
- Nikias, C. L., and Pan, R., 1987, Bispectrum Estimation: A digital signal processing framework: *Proceedings of the IEEE*, Vol 75, No. 7, 869-891.
- Nikias, C. L., and Pan, R., 1988, Time delay estimation in unknown Gaussian spatially correlated noise: *IEEE Trans. Acoust. Speech Signal Process*, 36, 1706-1714.
- Osman, N., 1998, *Broadband Stereoscopic Imaging of Ore Bodies*, Honour's Thesis, University of Sydney.
- Peradi, R. and Clement, A., 1972, Digital processing of refraction data study of first arrivals: *Geophys. Prosp.*, 20, 529-548.
- Paulson, K. V., and Merdler, S.C., 1968, Automatic seismic reflection picking: *Geophysics*, 33, 431-440.

- Peraldi, R. and A. Clement, 1972, Digital processing of refraction data study of first arrival: *Geophys. Prosp.*, 20, 529-548.
- Press, W. H., Teukolsky, S. A., Vetterling, W. T. and Flannery, B. P., 1992, *Numerical Recipe in C – The Art of Scientific Computing*, Second edition, Cambridge University Press.
- Rijks, E. J. H. and Jauffred, J. C. E. M., 1991, Attribute extraction: An important application in any detailed 3-D interpretation study: *The Leading Edge*, Vol. 10, 11-19.
- Rimmer, S., 1993, *Bit-Mapped Graphics*, 2nd Edition, Windcrest Books.
- Robinson, E. A., 1967, *Statistical communication and detection (with special reference to digital data processing and seismic signals)*, Hafner Publishing Company, New York.
- Robinson, J. E., 1978, Pitfalls in automated lithostratigraphic correlation: *Computers and Geosciences*, 4, 273-275.
- Rockwell, D. W., Migration stack aids interpretation, In: *Migration of seismic data* (ed. Gardener, H. F.), SEG, 75-81.
- Schneider, W. A., 1971, Developments in seismic data processing and analysis(1968-1970): *Geophysics*, 36, 1043-1073.
- Sheriff, R. E., 1991, *Encyclopedic dictionary of exploration geophysics* (third edition), Society of Exploration Geophysicists.
- Skolnik, M. I., 1970, *Radar Handbook*, McGraw-Hill Book Company.
- Spagnolini, U., 1991, Adaptive picking of refracted first arrivals: *Geophys. Prosp.*, 39, 293-312.
- Stolt, R., 1978, Migration by Fourier transform: *Geophysics*, **43**, 23-48.
- Stone, D. G., 1994, *Designing Seismic Surveys in Two and Three Dimensions*, SEG
- Taner, M. T. and Koehler, F., 1969, Velocity spectra—digital computer derivation and applications of velocity functions: *Geophysics*, **39**, 859-881.
- Taner, M. T., Koehler, F., 1969, Velocity spectra-Digital computer deviation and applications of velocity functions: *Geophysics*, 34, 859-881.
- Taner, M. T., Koehler, F., and Sheriff, R. E., 1979, Complex seismic trace analysis: *Geophysics*, 44, 1041-1063.

- Tu, P. H., 1995, Extracting and Analysing Seismic Events Using Computer Vision Techniques, D.Phil. Thesis, Oxford University.
- Wang, X. and D. Waltham, 1995, The stable-beam seismic modeling method: Geophysical Prospecting, **43**, 939-961.
- White, R. E., 1990, Properties of instantaneous seismic attributes: The Leading Edge, Vol. 9, 26-32.
- Wu, X., and Nyland E., 1987, Automated stratigraphic interpretation of well log data: Geophysics, **52**, 1665-1676.
- Yilmaz, O., 1987, Seismic data processing: SEG.
- Yung, S. K. and Ikelle, Luc T., 1997, An example of seismic time picking by third-order bicoherence: Geophysics, **62**, 1947-1951.
- Zhe, J. and S. A. Greenhalgh, 1999, A new kinematic method for mapping seismic reflectors: Geophysics, **64**, 1594-1602.
- Zhou, B., Mason, I.M. and Greenhalgh, S.A., 1995, Accurate and efficient shot-gather dip moveout processing in the log-stretch domain: Geophysical Prospecting, **43**, 963-978.
- Zhou, B. and Hatherly, P., 1999, Interpretation of small scale geological features on seismic reflection data: A final report to ACARP.
- Zhou, B. and Hatherly, P., 2000, Pushing coal seismic to its limits through computer aided interpretation and 3D seismic: Exploration Geophysics, **31**, 343-346.